Participatory Roles of Urban Trees in Regulating Environmental Quality

by

Chenghao Wang

A Dissertation Presented in Partial Fulfillment
of the Requirements for the Degree
Doctor of Philosophy

Approved October 2019 by the
Graduate Supervisory Committee:

Zhihua Wang, Chair
Soe W. Myint
Huei-Ping Huang
Giuseppe Mascaro

ARIZONA STATE UNIVERSITY

December 2019

ABSTRACT

The world has been continuously urbanized and is currently accommodating more than half of the human population. Despite that cities cover only less than 3% of the Earth's land surface area, they emerged as hotspots of anthropogenic activities. The drastic land use changes, complex three-dimensional urban terrain, and anthropogenic heat emissions alter the transport of mass, heat, and momentum, especially within the urban canopy layer. As a result, cities are confronting numerous environmental challenges such as exacerbated heat stress, frequent air pollution episodes, degraded water quality, increased energy consumption and water use, etc. Green infrastructure, in particular, the use of trees, has been proved as an effective means to improve urban environmental quality in existing research. However, quantitative evaluations of the efficacy of urban trees in regulating air quality and thermal environment are impeded by the limited temporal and spatial scales in field measurements and the deficiency in numerical models.

This dissertation aims to advance the simulation of realistic functions of urban trees in both microscale and mesoscale numerical models, and to systematically evaluate the cooling capacity of urban trees under thermal extremes. A coupled large-eddy simulation–Lagrangian stochastic modeling framework is developed for the complex urban environment and is used to evaluate the impact of urban trees on traffic-emitted pollutants. Results show that the model is robust for capturing the dispersion of urban air pollutants and how strategically implemented urban trees can reduce vehicle-emitted pollution. To evaluate the impact of urban trees on the thermal environment, the radiative shading effect of trees are incorporated into the integrated Weather Research and

Forecasting model. The mesoscale model is used to simulate shade trees over the contiguous United States, suggesting how the efficacy of urban trees depends on geographical and climatic conditions. The cooling capacity of urban trees and its response to thermal extremes are then quantified for major metropolitans in the United States based on remotely sensed data. It is found the nonlinear temperature dependence of the cooling capacity remarkably resembles the thermodynamic liquid-water–vapor equilibrium. The findings in this dissertation are informative to evaluating and implementing urban trees, and green infrastructure in large, as an important urban planning strategy to cope with emergent global environmental changes.

ACKNOWLEDGMENTS

First of all, I would like to express my deepest and sincerest appreciation to my advisor and dissertation committee chair, Professor Zhihua Wang, for his effective guidance, strong support, and warm encouragement over the course of my Ph.D. studies. Professor Wang is a truly fantastic mentor, talented teacher, and passionate and intellectual scientist with knowledge and expertise in various research areas. He has given me the freedom to pursue different projects and provided very insightful discussions about my research and career. He has inspired me to become an independent researcher and helped me realize the power of critical reasoning.

I am also extremely grateful to my committee members, Professor Soe W. Myint, Professor Huei-Ping Huang, and Professor Giuseppe Mascaro for their time and patience in supervising my research work, their invaluable and insightful feedback and suggestions on this dissertation, and their indispensable contributions to my development as a young scientist.

I would like to thank Professor Enrique R. Vivoni, Professor Larry W. Mays, Professor Kamil E. Kaloush, Professor Peter Fox, Professor Rebecca L. Muenich, and Professor Margaret Garcia at the School of Sustainable Engineering and the Built Environment, and Professor Anthony J. Brazel, Professor David J. Sailor, Professor Ariane Middel, Professor Wenwen Li, and Professor Sergio J. Rey at the School of Geographical Sciences & Urban Planning, for their kind help, advice, and encouragement during my time at Arizona State University.

Special thanks to my research collaborators Professor Qi Li, Professor Jiachuan Yang, Professor Jiyun Song, Professor Chuyuan Wang, Professor E. Scott Krayenhoff,

and Ruby Upreti. Working with them is always a great pleasure, which has greatly helped me branch out into various new research areas. I also thank Professor C. Sue B. Grimmond, Dr. Jeffrey C. Weil, Professor Elie Bou-Zeid, Professor Xuhui Cai, Professor Andreas Stohl, Professor Antti Hellsten, Dr. Paul E. Bieringer, and Professor Saravanan Arunachalam for their kind assistance and constructive suggestions on my research and career development. I would like to thank my former advisors, Professor Shangbin Xiao and Professor Ji Liu, for their continuous encouragement.

I gratefully acknowledge the financial support from many organizations and departments, including the U.S. National Science Foundation, the U.S. Army Research Laboratory, the National Transportation Center at the University of Maryland, the National Asphalt Pavement Association, and the Graduate College at Arizona State University (through two completion fellowships). I also wish to thank the American Meteorological Society Committee on Boundary Layers and Turbulence, the Graduate and Professional Student Association, and the Graduate College for their financial support for my travels to many conferences.

Finally, I would like to express my special thanks to my family and my fiancée for listening, offering me advice, and being supportive of my academic endeavors. Many thanks to my friends and lab mates for their support, encouragement, and general help throughout this journey.

TABLE OF CONTENTS

Page

CHAPTER Page

LIST OF TABLES

LIST OF FIGURES

Figure Page

Figure Page

CHAPTER 1

INTRODUCTION

1.1. Literature Review

1.1.1. Background

Global urbanization, driven by rapid growth of population and socio-economic development, is primarily in the form of expansion of built terrains toward natural periphery (Bettencourt et al. 2007; Grimm et al. 2008; Kalnay and Cai 2003; Seto, Güneralp, and Hutyra 2012; United Nations 2015). Among all human-induced landscape changes, urbanization emerges as the most drastic and irreversible form (Seto et al. 2011). Urban environment is characterized by heterogeneous morphology of mosaic urban landscapes and extensive anthropogenic activities (Oke et al. 2017). The presence of engineering materials, surface heterogeneity, and anthropogenic stressors reshapes the patterns of atmospheric boundary-layer (ABL) turbulence and water and energy exchange in the urban atmosphere and hydrosphere at different scales (Arnfield 2003; Z.-H. Wang, Bou-Zeid, and Smith 2013; Song, Wang, and Wang 2018). For example, the impervious surfaces used in the construction of roads and parking lots reduce the infiltration toward the ground, meanwhile increasing the surface runoff (Fig. 1.1). The anthropogenic emissions of waste by-products of urban metabolism (e.g., water vapor, particulate air pollutants, aerosols, etc.) have a significant impact on the air quality as well (Oke et al. 2017; Song, Wang, and Wang 2017). As a consequence, a series of environmental issues has arisen, such as the urban warming (C. Wang and Wang 2017), air pollution episodes (Chan and Yao 2008), formation of urban heat island (UHI) (Grimmond 2007), degradation of environmental quality and ecosystem services (Stone Jr 2005), elevated

energy and water usage (Breyer, Chang, and Parandvash 2012), and rise in heat-related morbidity and mortality (Harlan et al. 2006).

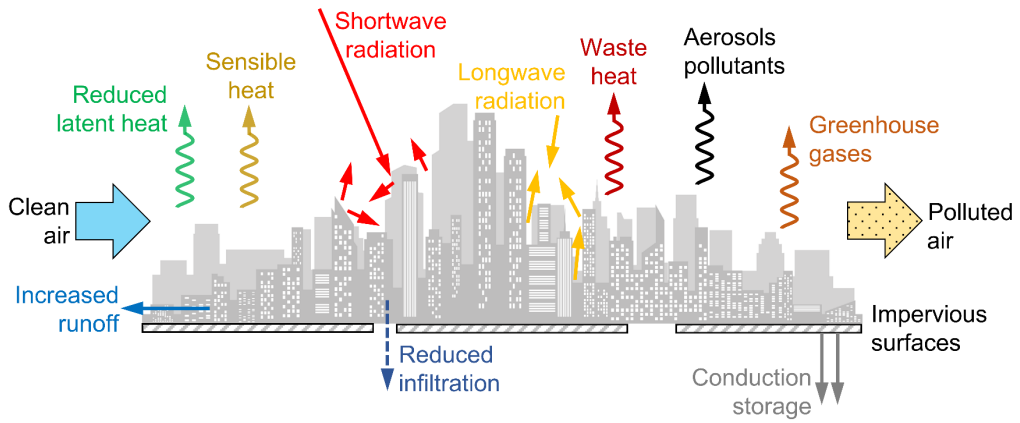

Figure 1.1. Impacts of urban development on the urban atmosphere and hydrosphere.

In particular, the UHI effect is a prominent phenomenon in many cities worldwide, in which the urban cores are found usually warmer than their peripheral rural areas (S. Peng et al. 2012). The UHI effect is primarily attributable to the use of man-made materials, the complex geometry of the urban environment, the reduction of vegetation, and the anthropogenic (waste) heat emissions (Akbari and Kolokotsa 2016). As illustrated in Fig. 1.1, the radiative properties (albedo and emissivity) and conductive properties (thermal admittance and conductivity) of man-made materials are distinct from those of natural landscape, altering the heat absorption, storage, and release processes (Grimmond 2007). Compared to natural surfaces, man-made materials with large heat capacity have a higher nighttime temperature, while dark (low albedo) pavement surface exerts a higher daytime temperature (Phelan et al. 2015). The complex geometric properties of urban structure, such as orientation and sky openness, also play an

important role in radiative exchanges within the urban canopy. In addition, the lack of vegetation in cities reduces the magnitude of latent heat flux, therefore resulting in increased sensible and conductive heat fluxes in the partitioning of net radiation (Arnfield 2003). Anthropogenic heat emissions through human metabolism, industrial activities, building energy use, and transportation (vehicles) are additional sources of heat, furthering contributing to the UHI effect (Sailor 2011). It is noteworthy that anthropogenic heat emissions can serve as a positive feedback in the formation of UHI, as higher temperature contributes to the increase in building energy use for heating, ventilation, and air conditioning, especially during hot seasons.

Over decades, researchers, policy makers, and practitioners have joined synergy in improving the urban environmental quality (Howells et al. 2013), especially the thermal environment, using various mitigation and adaptation strategies like the use of urban green infrastructure and innovative engineering materials (Bowler et al. 2010; Santamouris 2014). In particular, the plantation of trees has emerged as a popular solution for alleviating the excessive thermal stress in cities, with other community benefits such as stormwater management (U.S. EPA 2008). Trees have multiple biophysical functions in the urban ecosystem (Erell, Pearlmutter, and Williamson 2011), among which the radiative shading and evapotranspiration (ET) are predominant in regulating the thermal environment. As illustrated in Fig. 1.2a, the presence of crowns can reduce the penetration of shortwave solar radiation, and lower the surface and air temperatures in shade (Roy, Byrne, and Pickering 2012). But tree crowns block a part of upwelling longwave radiation at night, which may result in higher temperature beneath the trees (radiative trapping effect) as reported in some numerical simulations (Loughner

et al. 2012). In addition, trees can provide cooling through transpiration, especially during nighttime (Konarska, Uddling, et al. 2016). It is noteworthy that the evapotranspirative cooling (hereafter "ET cooling") is highly affected by the seasonal variability in foliage for deciduous trees. It could be relatively insignificant for xeric trees (Song and Wang 2015b; 2016) and coniferous trees. The cooling effect of trees is in general beneficial to the urban environment, leading to energy saving and improved pedestrian thermal comfort during hot seasons (Shahidan et al. 2010).

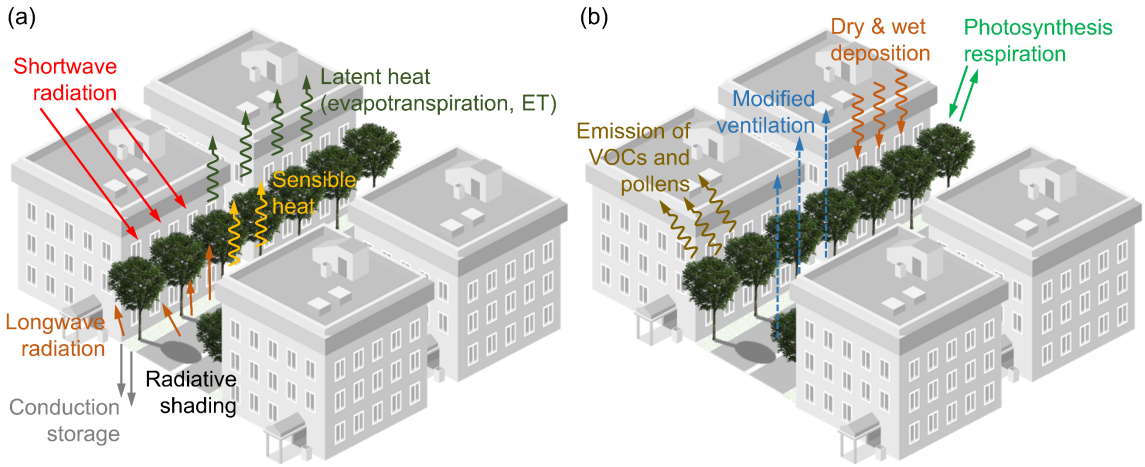

Figure 1.2. Participatory roles of urban trees (street trees as an example) in regulating (a) thermal environment and (b) air quality.

On the other hand, trees play complex participatory roles in gas exchange (e.g., through photosynthesis and respiration) as well as atmospheric pollutant dispersion and deposition (Fig. 1.2b). They are not only important biological sources of volatile organic compounds (VOCs) and pollen (Leung et al. 2011; Vos et al. 2013), but can also absorb gaseous pollutants through stomata, and gather particulate matters via wet and dry

deposition (Salmond et al. 2016). As the sources of emission, trees produce pollen and trigger allergies at their anthesis stage; besides, emitted biogenic VOCs produce secondary air pollutants like ozone (Leung et al. 2011). Aerodynamically, urban trees act as porous media, induce substantial drag on flow field, and result in momentum loss (Gromke and Ruck 2008). In addition, the aforementioned shading and radiative trapping effects of trees (Shashua-Bar and Hoffman 2000; Upreti, Wang, and Yang 2017; Z.-H. Wang, Zhao, et al. 2016) affect the surface temperature of urban facets and heat exchange, leading to the change of thermal field and thermally induced motion (Kim and Baik 2001; Li and Wang 2018).

1.1.2. Modeling the Participatory Roles of Urban Trees in Regulating the Air Quality

Numerous studies have investigated the impact of trees on urban pollution in real cities (Janhäll 2015; Salmond et al. 2016). Remotely sensed air pollution retrieval (e.g., aerosol optical depth) can provide long-term records for spatio-temporal analysis, albeit without revealing physical mechanisms (C. Wang et al. 2017). Early numerical models, such as the airshed simulation model, indirectly assess the impact via meteorological changes induced by urban trees, but with oversimplified aerodynamic effects of trees (Akbari, Pomerantz, and Taha 2001). Advances in numerical modeling techniques, on the other hand, have enabled sophisticated computational fluid dynamics (CFD) modeling for realistic urban morphologies from microscale to neighborhood/local scale, by including tree effects as a momentum sink term or drag force into the governing equation (Amorim et al. 2013; Giometto et al. 2017; Jeanjean, Monks, and Leigh 2016). In particular, CFD

models were coupled with the numerical weather prediction model, which can capture mesoscale land–atmosphere interaction (Tewari et al. 2010).

To simplify the representation of complex built terrains, two- or three-dimensional (2D or 3D) street canyons were widely used in both scale models (e.g., wind tunnel experiments) and land surface models. Extensive wind tunnel measurements have been conducted at Karlsruhe Institute of Technology using an isolated 3D urban street canyon with trees and canyon aspect ratio (i.e., the ratio of building height to street width) of unity (Gromke and Ruck 2012; 2009; 2007). It was found that ventilation is weakened by trees, leading to reduced windward-side pollutant concentration but rising concentration near the leeward wall, while on the leeward-side, pollutant concentration increases with size and porosity of tree crowns (Gromke and Ruck 2009; 2007).

Numerically, Reynolds-averaged Navier–Stokes (RANS) closure models with different turbulence closure schemes (k–ε model, Reynolds stress equation model, etc.) were commonly adopted for solving the flow field affected by trees and buildings within canopy layers (Gromke et al. 2008; Salim, Cheah, and Chan 2011; Xue and Li 2017). Large-eddy simulation (LES) models, more sophisticated and often more accurate than RANS (Tominaga and Stathopoulos 2016), were adopted to resolve the large-scale eddies explicitly with subgrid-scale (SGS) components parameterized. LES techniques have undergone continuous developments over decades, particularly aiming at capturing turbulent flows within the ABL over complex terrains (Wood 2000). Early research using LES focused on simulating flows through homogeneous forest canopies (Su, Shaw, and U 2000), while in recent years complex airflow within and over heterogeneous canopies was extensively studied (Belcher, Harman, and Finnigan 2012). Advances in remote

sensing techniques (e.g., terrestrial laser scanning) expedited finer LES studies on highly resolved forest canopy (Schlegel et al. 2015). On the other hand, LES using scale-dependent Lagrangian dynamic SGS model was conducted over a built terrain; such applications with highly heterogeneous boundary conditions have demonstrated the robustness of LES in urban applications (Tseng, Meneveau, and Parlange 2006). In a comparative study of urban canyons with trees, Salim, Cheah, and Chan (2011) also showed that LES outperformed RANS model in general. Recently, simplistic representation of urban trees was incorporated into the aforementioned group of LES model (Li and Wang 2018).

Simulations directly using CFD models in parallel/online mode, however, are computationally expensive for the short-range dispersion of passive scalars over complex terrain within the ABL. An alternative option is the Lagrangian stochastic models (LSMs), which are a versatile tool in modeling turbulent diffusion (Rodean 1996). LSMs are driven by turbulent flow field and variances that can be analytically resolved or parameterized (Rotach 2001; C. Wang et al. 2018). It was found that, simplified resolution of flow field is in general inadequate for simulating atmospheric dispersion over complex terrains (C. Wang et al. 2018); this inadequacy especially surfaces within the roughness sublayer in the presence of trees. A coupled CFD–LSM framework, in contrast, adopts more accurate CFD-generated flow field, meanwhile possessing flexibility of changing the emission conditions. It therefore represents an economic and robust alternative for simulating the impact of urban trees on pollutant dispersion, which remains hitherto scarce in the literature.

1.1.3. Modeling the Participatory Roles of Urban Trees in Regulating the Thermal Environment

The contribution of trees to a cooler urban environment has been examined and evaluated through *in situ* observations, scale model simulations, numerical model simulations, and remote sensing (Bowler et al. 2010; Richards and Oke 2002; Z.-H. Wang, Zhao, et al. 2016; Myint et al. 2013). Both based on direct measurements, *in situ* observations and scale model simulations are usually conducted over short time periods ranging from hours to days (e.g., Park et al. 2012; Shashua-Bar, Pearlmutter, and Erell 2009). Although there were studies with longer records of field measurements (Hamada and Ohta 2010), the spatial scales are still relatively limited. Meanwhile, different local environments and experimental conditions can lead to significant biases among studies; similar inconsistency has been observed even during the same study due to studied tree species and local geometry (Konarska, Holmer, et al. 2016; Konarska, Uddling, et al. 2016). Numerical models of urban trees with e.g., physical parameterization schemes possess the capability of analyzing real situations or projected scenarios at greater scales (Loughner et al. 2012; C. Wang, Wang, and Yang 2018). In addition, the flexibility of model setups enables us to evaluate the effect of urban tree characteristics, such as tree crown size, on the cooling effect (Z.-H. Wang, Zhao, et al. 2016). It is noteworthy that sub-urban scale numerical models such as ENVI-met have been used to simulate urban trees primarily due to its convenience in software setups (Middel, Chhetri, and Quay 2015). However, these sub-urban scale numerical models largely miss the feedback in the integrated soil–vegetation–atmosphere system. Multiscale numerical frameworks therefore hold the key to more realistic modeling of urban trees and their impact on local

and regional hydroclimates via land–atmosphere interactions. One particular framework of this kind is the mesoscale Weather Research and Forecasting (WRF) model coupled with urban land surface processes parameterized by urban canopy models (UCMs) (Chen et al. 2011).

Recent years have seen the continuous development in the coupled WRF-UCM framework by incorporating urban trees. The effect of ET cooling of urban trees has been investigated (Lee et al. 2016; Lee and Park 2008), whereas the participatory role of trees in radiative heat exchange has not been considered. To model the radiative shading effects of trees, the ray tracing approach based on the Monte Carlo simulations (MCS) was developed to compute the modified view factors between urban facets and trees (Krayenhoff et al. 2014; Z.-H. Wang 2014b). Furthermore, biophysical functions (ET and soil water dynamics) of trees with seasonal variability have been implemented in a UCM (Ryu et al. 2016), but in an offline setting (without coupling to mesoscale atmospheric dynamics). The online WRF-UCM simulations have been conducted lately to evaluate the effect of tree shades on regional hydroclimatic changes (Upreti, Wang, and Yang 2017). Nevertheless, simultaneous modeling of the cooling effect of shade trees at large continental scale for cities in a wide variety of geographical and climatic conditions is hitherto missing.

1.1.4. Unique Characteristics of Urban Trees and the Potential of Using Remote Sensing Technology in Detecting Their Cooling Capacity

The unique characteristics of trees in the urban environment have received considerable attention by researchers during the past decades. The growth of urban trees

is usually affected by management activities and the ambient built environment, resulting in different ecological patterns and processes (e.g., Nowak, Kuroda, and Crane 2004) when compared to the growth of rural and undisturbed natural forests. Quigley (2004) examined 15 hardwood tree species in urban and rural areas in central Ohio based on annual rings, suggesting that hardwood trees grew at slower rates in urban areas presumably limited by rooting zone conditions. The lack of biologic diversity among tree species also increases the vulnerability of urban trees under the threat of insect pests, as documented in 12 cities in the eastern North America (Raupp, Cumming, and Raupp 2006). In contrast, some other studies observed increased biomass and prolonged growing season of urban vegetation in response to urban warming and air pollution. An experiment conducted in New York City using cottonwood clone found that plant biomass in the urban environment was much higher than that in peripheral rural areas, owing to the difference in ozone exposure (Gregg, Jones, and Dawson 2003). Another 32-city investigation in China based on satellite data also confirmed the prevalence of vegetation growth enhancement in urban areas (S. Zhao, Liu, and Zhou 2016).

With the advances in sensor design and the development of data processing algorithm, remote sensing technology has been more widely utilized for assessing the functions of trees in regulating urban climates. Remotely sensed data are flexible in both spatial and temporal resolutions, facilitating the comparisons of the cooling effect provided by urban trees between cities (Spronken-Smith and Oke 1998; Myint et al. 2015). Studies using high spatial resolution data suggested that the spatial configuration of urban trees significantly affect the cooling capacity, while the trend remains uncertain. For instance, W. Zhou, Wang, and Cadenasso (2017) reported a negative correlation

between mean patch size of urban trees and land surface temperature (LST) in Sacramento, California but positive in Baltimore, Maryland. In addition, Earth observing missions such as National Aeronautics and Space Administration (NASA)'s Earth Observing System have been continuously operated for years, providing extensive remotely sensed data for urban climate research. These datasets enable more systematic studies across multiple cities with various background geographical conditions.

Considering the unique characteristics of urban trees, understanding how their cooling effect varies with the ambient environment is very crucial for future urban planning, especially during extreme climate events like heat waves. However, the response of urban trees and their cooling effect to thermal extremes across different climate types still remains obscure, and quantitative assessments on this topic are heretofore absent. Compared to modeling approaches that involve numerical assumptions, the use of remote sensing products can more realistically describe urban surface conditions, and can potentially reveal general patterns in the cooling capacity of urban trees.

1.2. Research Objectives and Dissertation Structure

Based on the reviewed literature and identified research and knowledge gaps of urban trees in Section 1.1, this dissertation aims to evaluate the impacts of urban trees on environmental quality using models and remote sensing products to support more sustainable future urban development under the changing climate. In particular, the two major objectives are: (i) to advance the representation of realistic functions of urban trees

in both microscale and mesoscale numerical models, and (ii) to understand the functions of urban trees under thermal extremes using remote sensing products.

To achieve these objectives, this dissertation is organized as follows. Chapter 2 describes a coupled LES–LSM framework developed for the complex urban environment and its application to predicting the impact of urban trees on the dispersion of traffic-emitted air pollutants, which has been published in C. Wang, Li, and Wang (2018). Chapter 3 investigates the impacts of shade trees on urban hydroclimate, pedestrian thermal comfort, and urban surface energy balance across the contiguous United States (contiguous U.S. or CONUS) by incorporating urban trees into the integrated WRF-urban modeling system, which has been published in C. Wang, Wang, and Yang (2018). Chapter 4 examines how the cooling capacity of urban trees responses to extreme hot and cold weathers (i.e., heat waves and cold spells) in major U.S. metropolitans using remote sensing products and discusses the potential cooling capacity of urban trees under future climate, which has been published in C. Wang et al. (2019). Finally, Chapter 5 summarizes this dissertation with key findings on the participatory roles of urban trees in regulating environmental quality as well as the implications of this work. Chapter 5 also outlines a few recommendations for future research directions.

CHAPTER 2

MICROSCALE IMPACT OF URBAN TREES ON THE DISPERSION OF TRAFFIC POLLUTANT EMISSIONS

As discussed in Chapter 1, a coupled CFD–LSM (modeling) framework adopts more accurate CFD-generated flow field, meanwhile possessing flexibility of changing the emission conditions. In this chapter, we aim to develop an integrative modeling framework by coupling LES and LSM, and to quantify how various geometry of canyons and trees can impact the flow field and pollution distribution. The proposed modeling framework is first applied to simulate passive pollutant dispersion in a square street canyon with canyon aspect ratio equal to one, and results are evaluated against observational data. The coupled LES–LSM is then used to model 24 cases with various geometries of street canyon and tress, in which the results are compared, showing the sensitivity of traffic-emitted pollutant dispersion to the forms of street canyons and urban trees.

2.1. Methodology

2.1.1. The Coupled LES–LSM Modeling Framework

In LES, the spatially-filtered Navier–Stokes equations with Boussinesq approximation in rotation form under neutral stability conditions are (Bou-Zeid et al. 2009; Li and Wang 2018)

$$\frac{\partial \tilde{u}_i}{\partial x_i} = 0, \tag{2.1}$$

$$\frac{\partial \tilde{u}_i}{\partial t} + \tilde{u}_j \left(\frac{\partial \tilde{u}_i}{\partial x_j} - \frac{\partial \tilde{u}_j}{\partial x_i} \right) = -\frac{1}{\rho_0} \frac{\partial \tilde{p}^*}{\partial x_i} - \frac{\partial \tau_{ij}}{\partial x_j} + \tilde{F}_i + \tilde{f}_i^B + \tilde{f}_i^T , \tag{2.2}$$

where $\tilde{u}_i$ is the filtered wind velocity vector in the Cartesian coordinate system x_i, with i and j = 1, 2, or 3 the free indices, t is time, $\tilde{p}^*$ is the modified pressure term calculated as $\tilde{p}^* = \tilde{p} + \rho_0 \left(\frac{1}{3}\sigma_{kk} + \frac{1}{2}\tilde{u}_j \tilde{u}_j \right)$, ρ_0 is the air density, τ_{ij} is the anisotropic part of the SGS stress tensor σ_{ij}, $\tilde{F}_i$ is the mean streamwise pressure forcing that drives the flow, $\tilde{f}_i^B$ is the immersed boundary force exerted by the obstacles (buildings herein), and $\tilde{f}_i^T$ is the kinematic drag from trees. Note that the tilde (˜) denotes the filtering at grid scale Δ. The molecular viscous term is negligible at very high Reynolds number. The anisotropic part τ_{ij} is evaluated using the scale-dependent Lagrangian dynamic SGS model (Bou-Zeid, Meneveau, and Parlange 2005). The advection–diffusion equation for temperature is given by (Li and Wang 2018)

$$\frac{\partial \tilde{\theta}}{\partial t} + \tilde{u}_i \frac{\partial \tilde{\theta}}{\partial x_i} = -\frac{\partial \pi_i}{\partial x_i} , \tag{2.3}$$

in which $\tilde{\theta}$ is the resolved temperature, and π_i is the SGS heat flux.

We assume that the flow over leaves and branches is in the fully rough regime and thus form drag dominates, which is a commonly adopted approach in flows over vegetation (Giometto et al. 2017; Patton et al. 2016; Shaw and Schumann 1992). The drag force from trees uses the parameterization scheme (Giometto et al. 2017; Pan, Chamecki, and Isard 2014)

$$\tilde{f}_i^T = -C_d L(z) P_i \cdot \left| U_{\mathrm{LES}} \right| \cdot u_i , \tag{2.4}$$

in which the sectional drag coefficient C_d = 0.40 is used based on wind tunnel experiments for different plant species (Gillies, Nickling, and King 2002). Note that the uncertainty in C_d affects the accuracy of modeled turbulent statistics, regardless of the selected scheme of turbulence closure (Pinard and Wilson 2001). Further refinements are possible by adopting variable C_d such as velocity-dependent drag coefficients (Pan, Chamecki, and Isard 2014). P_i is the projection coefficient tensor to acquire effective leaf area densities facing 3D directions, while in this study $P_x = P_y = 0.28$ (symmetric in horizontal directions) and $P_z = 0.44$ are adopted (Li and Wang 2018; Pan, Chamecki, and Isard 2014). The projection coefficient tensor can be altered based on other measurements to account for more complex 3D canopy anisotropy. U_{LES} is the magnitude of the wind speed vector (Amorim et al. 2013), and L is the vertical distribution of the leaf area density (LAD), empirically expressed as (Lalic and Mihailovic 2004)

$$L(z) = L_{\max}\left(\frac{h_T - z_{\max}}{h_T - z}\right)^n \exp\left[n\left(1 - \frac{h_T - z_{\max}}{h_T - z}\right)\right], \tag{2.5}$$

where h_T is the tree height, and $L_{\max}$ is the maximum LAD at the corresponding height $z_{\max}$. The values of parameter n are 6 and 0.5 for ranges $0 \le z < z_{\max}$ and $z_{\max} \le z \le h_T$, respectively (Lalic and Mihailovic 2004). Although the distribution of LAD may vary with specific tree/vegetation species, this empirical expression is sufficient to represent various tree morphologies in the present study.

The shading effect of trees is included via the modification of temperature boundary conditions, and the temperature boundary conditions are constrained by the net radiation on the urban surface. The surface temperature is solved using a one-dimensional subsurface heat conduction model and the information provided by the wall-modeling in

LES (Li et al. 2016). The procedure is documented in Li and Wang (2018). The urban facets are assumed to have a uniform thickness (0.5 m) with a constant surface interior temperature (25 °C) (Li and Wang 2018). As the first step, the shading effect of trees is restrained to noon (local time), at which the zenith and azimuth angles are 0° and 180°, respectively.

The LES model (Albertson 1996; Albertson and Parlange 1999) has been validated for neutral and convective boundary layers in previous studies (Bou-Zeid, Meneveau, and Parlange 2005; Kumar et al. 2006). The LES code solves the 3D filtered momentum and temperature equations written in rotational form. Second-order centered finite differences in the vertical and pseudospectral differentiation in the horizontal directions are implemented for computing spatial derivatives, and a fully staggered uniform grid configuration is used. The convective terms are fully dealiased using the 3/2-rule (Orszag 1971). A scale-dependent Lagrangian dynamic model (Bou-Zeid, Meneveau, and Parlange 2005) is used as the SGS model. The Poisson equation for pressure is solved numerically using the spectral transform in the horizontal and finite differences in the vertical directions with a tridiagonal solver. Time integration is carried out using the second-order Adams–Bashforth method. The discretization approaches and boundary conditions adopted in the LES model are summarized in Table 2.1.

Table 2.1. Discretization approaches and boundary conditions in the LES model

LES model setups	Details
Discretization approaches	
Horizontal direction	Fourier-based pseudospectral
Vertical direction	Second-order centered finite differences
Grid configuration	Fully staggered uniform grid
Time integration	Second-order Adams–Bashforth method
Boundary conditions	
Domain	Horizontally periodic (infinitely long canyons in spanwise direction)
Domain bottom	No-slip, wall-modeling approach
Domain top	Stress-free for velocity, zero heat flux for temperature

The LSM is used to numerically represent particle movements over time (viz., particle trajectories). The molecular diffusion of particles is neglected at high Reynolds number, yielding the assumption that tracer particles approximatively travel at local velocities (Thomson 1987). The Markovian evolution of the velocity $u_{i,p}$ and position $x_{i,p}$ of a particle is described with stochastic differential equations (Thomson 1987; Wilson and Sawford 1996)

$$du_{i,p} = a_i\left(x_{i,p}, u_{i,p}, t\right)dt + b_{ij}\left(x_{i,p}, u_{i,p}, t\right)d\lambda_j, \tag{2.6}$$

$$dx_{i,p} = u_{i,p}dt, \tag{2.7}$$

where a_i and b_{ij} are drift and random acceleration coefficients, respectively, $d\lambda_j$ is the Gaussian white noise component, and the subscript p denotes velocity or position of the particle. The first term on the right-hand-side of Eq. (2.6) is the deterministic part expressed as

$$a_i = -\frac{1}{2} b_{ik} b_{jk} \frac{u_{k,p} - U_k}{V_{jk}} + \phi_i / g_a , \tag{2.8}$$

in which U_k is the mean velocity field, and the notation $V_{jk} = \left\langle \left(u_{j,p} - U_j\right)\left(u_{k,p} - U_k\right) \right\rangle$, with angled brackets denoting ensemble average. The random acceleration coefficient has the form

$$b_{ij} = \delta_{ij} \sqrt{C_0 \varepsilon} , \tag{2.9}$$

to ensure accuracy on timescale greater than the Kolmogorov timescale, with time lag falling within the inertial subrange (Thomson 1987). In Eq. (2.9), δ_{ij} denotes the Kronecker delta, ε is the turbulent kinetic energy dissipation rate, and C_0 (≈ 3.0) is the inertial subrange Kolmogorov constant in the Lagrangian structure function (Hsieh and Katul 2009; Thomson 1987). To satisfy the well-mixed criterion, the Thomson's "simplest" solution (Thomson 1987), though there is no unique solution for 3D space (Rodean 1996), is adopted in Eq. (2.8)

$$\frac{\phi_i}{g_a} = \frac{1}{2}\frac{\partial V^{il}}{\partial x_{l,p}} + \frac{\partial U_i}{\partial t} + U_l \frac{\partial U_i}{\partial x_{l,p}} + \left[\frac{1}{2} V_{lj}^{-1} \left(\frac{\partial V^{il}}{\partial t} + U_m \frac{\partial V^{il}}{\partial x_{m,p}} \right) + \frac{\partial U_i}{\partial x_{j,p}} \right] \left(u_{j,p} - U_j\right)$$

$$+ \frac{1}{2} V_{lj}^{-1} \frac{\partial V^{il}}{\partial x_{k,p}} \left(u_{j,p} - U_j\right)\left(u_{k,p} - U_k\right). \tag{2.10}$$

The LES and LSM are coupled in offline mode, meaning particles trajectories are simulated by the Langevin equation in LSM, meanwhile the non-Gaussian forcing, i.e.,

the Eulerian flow statistics and fields required in LSM, is pre-generated using LES in different cases.

2.1.2. Model Setup

The model domains and configurations of urban geometry are shown in Fig. 2.1a and b. For LES, a cuboid-shaped 3D domain is adopted, with the size of 307.2 m (streamwise) × 153.6 m (lateral/spanwise) × 50 m (vertical) and the spatial resolution of 192 × 96 × 80 grid points. The domain settings used in this study have been evaluated in previous studies (Li et al. 2016; Tseng, Meneveau, and Parlange 2006). The building height is fixed to the lower 16 points. As described in Section 2.1.1, trees are parameterized as volumes using Eq. (2.5), whilst buildings are resolved using the simplified 3D canyon geometry. Periodic boundary condition is applied in the horizontal direction, thus the number of canyons differs for different canyon aspect ratios given the same domain length in streamwise direction. A free-lid boundary condition is used at the domain top. Immersed boundary method is implemented to represent the effects of obstacles on the flow via the discrete forcing method, which imposes zero velocity inside and on the boundary of the obstacles (Chester, Meneveau, and Parlange 2007; Li, Bou-Zeid, and Anderson 2016). The thermal boundary condition implements a surface energy balance scheme, where the heat conduction into the surface and surface temperature are explicitly computed in the simulation. The net radiation R_n reaching heterogeneous urban surface partitions into ground heat flux G, sensible heat flux H_s, and latent heat flux LE (not included in this study), as shown in Fig. 2.1a. A constant R_n of 200 W m^{-2}, an R_n reduction of 25% due to tree shading, and a surface interior temperature of 25 °C are

postulated to achieve initial temperature of each facet, and initialized radiative fluxes. All cases were run for 20 eddy turnover times. Note that the eddy turnover time is the ratio of vertical domain height to friction velocity u_*. The first 10 eddy turnover times served as a spin-up period, while the last 10 were averaged to yield turbulent statistics and flow information. The convergence test was conducted with a 10-eddy-turnover-time moving window to achieve a quasi-steady state (Li and Wang 2018). Furthermore, data from LES model were first averaged in the spanwise direction and over the periodic units of street canyons. Then the averaged data were scaled to be dimensionless by the friction velocity and urban geometry, and were uniformly scaled to drive LSM.

Different from the LES domain, the LSM domain is 2D consisting of only unit of street canyon, i.e., $(W_c + R) \times H_{\text{domain}}$, with W_c the street or road width, R the roof width, H_{domain} the domain height, and infinite in the spanwise dimension (Fig. 2.1b). We select four representative sets of canyon geometry with the aspect ratio H/W_c = 1.0, 0.2, 0.5, and 5.0, respectively (hereafter referred to as “square”, “wide”, “broad”, and “narrow” for simplicity) for numerical simulations. Note that H is the building height. Each set contains six cases of different tree geometries, with NoTree case serving as the control, and others including trees with various heights, crown sizes, and distributions of LAD, following Li and Wang (2018) with prescribed thermal boundary conditions. Tree0 and TreeWide cases have the same LAD profile, but different tree crown sizes. In addition, the friction velocity u_* = 0.4 m s^{-1} is used to scale turbulent flow and statistics, following C. Wang et al. (2018). The parameter space of all simulations is detailed in Table 2.2.

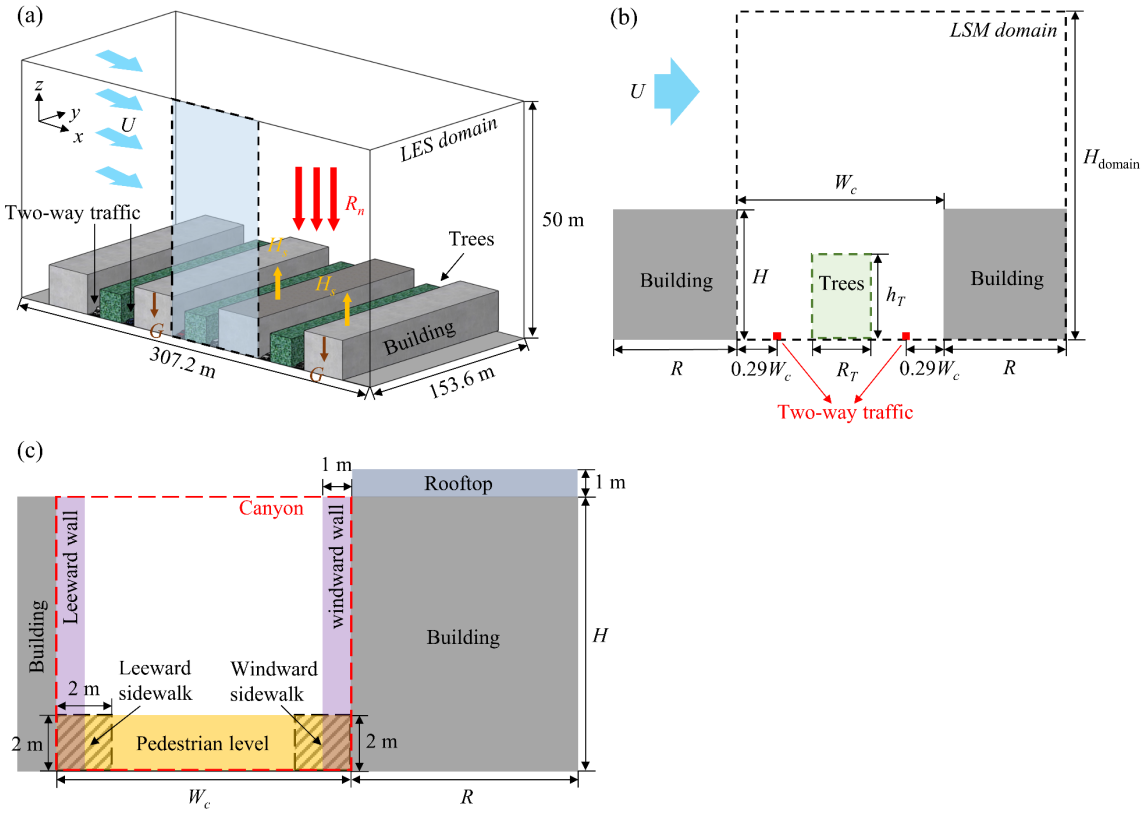

Figure 2.1. Domains and model setups for (a) LES (schematic diagram) and (b) LSM, and (c) zones for concentration evaluation. For the LES model the domain is horizontally periodic, and canyons are infinitely long in spanwise direction. The LES domain bottom is no-slip; the top is stress-free for velocity, and zero heat flux for temperature.

Table 2.2. Summary of cases and model parameters

Cases	Building height, H (m)	Canyon width, W_c (m)	Roof width, R (m)	Tree crown size, R_T/H	Tree height, h_T/H	Height of the LAD_{max}, z_{max}/ h_T	Maximum value of LAD, L_{max} (m^2m^{-3})	Domain height, H_{domain} (m)
Canyon aspect ratio H/W_c = 1.0								
NoTree	10	10	10	–	–	–	–	50
Tree0	10	10	10	0.25	0.75	0.8	2.8	50
Tree0*	10	10	10	0.25	0.75	0.5	2.8	50
TreeTall	10	10	10	0.25	1.25	0.8	2.8	50
TreeWide	10	10	10	0.50	0.75	0.8	2.8	50
TreeSparse	10	10	10	0.25	0.75	0.8	0.5	50
Canyon aspect ratio H/W_c = 0.2								
NoTree	10	50	10	–	–	–	–	50
Tree0	10	50	10	0.25	0.75	0.8	2.8	50
Tree0*	10	50	10	0.25	0.75	0.5	2.8	50
TreeTall	10	50	10	0.25	1.25	0.8	2.8	50
TreeWide	10	50	10	0.50	0.75	0.8	2.8	50
TreeSparse	10	50	10	0.25	0.75	0.8	0.5	50
Canyon aspect ratio H/W_c = 0.5								
NoTree	10	20	10	–	–	–	–	50
Tree0	10	20	10	0.25	0.75	0.8	2.8	50
Tree0*	10	20	10	0.25	0.75	0.5	2.8	50
TreeTall	10	20	10	0.25	1.25	0.8	2.8	50
TreeWide	10	20	10	0.50	0.75	0.8	2.8	50
TreeSparse	10	20	10	0.25	0.75	0.8	0.5	50
Canyon aspect ratio H/W_c = 5.0								
NoTree	50	10	10	–	–	–	–	100
Tree0	50	10	10	0.15	0.20	0.8	2.8	100
Tree0*	50	10	10	0.15	0.20	0.5	2.8	100
TreeTall	50	10	10	0.15	0.30	0.8	2.8	100
TreeWide	50	10	10	0.20	0.20	0.8	2.8	100
TreeSparse	50	10	10	0.15	0.20	0.8	0.5	100

Two sources of emission are included in the canyon located at the road level (with 0.5 m in height) as suggested by Gromke and Ruck (2009), to represent the two-way traffic emission. The initial 2D velocity components of released particles were prescribed as zeros, as the exhaust emission is primarily along lateral (spanwise) direction. The pollutant/particle concentration c was normalized using

$$\overline{c} = n_i / \sum_{i=1}^{n_t} \left(2N_i\right), \tag{2.11}$$

where n_i is the number of particles in a 1 m × 1 m grid cell, $2N_i$ is the number of particles released at each time step (N_i per source), and n_t is the number of time steps in each simulation (200 in this study). Note that here each 2D 1 m × 1 m grid cell is the cross-sectional area of each 3D unit volume (1 m × 1 m × an infinite length). Counting particle numbers over each 2D grid cell is equivalent to aggregating all particles within each 3D unit volume.

2.2. Model Evaluations

We first evaluate the developed LES–LSM modeling framework against a water channel experiment done by Caton, Britter, and Dalziel (2003), in which a 7 cm × 7 cm cavity was used to represent a square canyon (H/W_c = 1.0), with a 3-m long Perspex plate installed at the roof level in the upstream of the cavity. Relatively uniform external flow field was generated at high Reynolds number, providing an ideal case for comparison. To mimic their water tunnel setups, a single emission source is placed in the street canyon in our LES–LSM modeling framework. The center of the emission source is at the road

surface level, and the released particles represent fluorescein. The canyon setups are identical to the NoTree case with $H/W_c = 1$.

The comparison of the vertical wind velocity (positive upward) at the canyon top is shown in Fig. 2.2a and b. The streamwise distance from the origin (leeward side) was normalized by canyon width W_c, and the profiles of vertical speed were normalized by the maxima W_{max}. The profile predicted by the LES model matches well with water tunnel measurement ($R^2 = 0.690$). The discrepancy can be attributed to different setups in our simulations, for example, the radiation exchange. Furthermore, the pattern is also consistent with measurements in a real street canyon (Louka, Belcher, and Harrison 1998). We then compare the simulated pollutant concentrations with measurements in a transient experiment (Caton, Britter, and Dalziel 2003). In the experiment, the spatially averaged concentration was measured right after stopping the source emission. Similarly, particles were released simultaneously from the source in our model, and the spatially averaged concentrations were calculated for the canyon zone (see Fig. 2.1c) and the whole domain. The mean concentrations in our model dilute exponentially with time, showing a similar evolution to observation by Caton, Britter, and Dalziel (2003). This comparison also provides useful information in determining a simulation time, in that nearly all particles initially released are depleted in the domain at the end of a continuously releasing simulation.

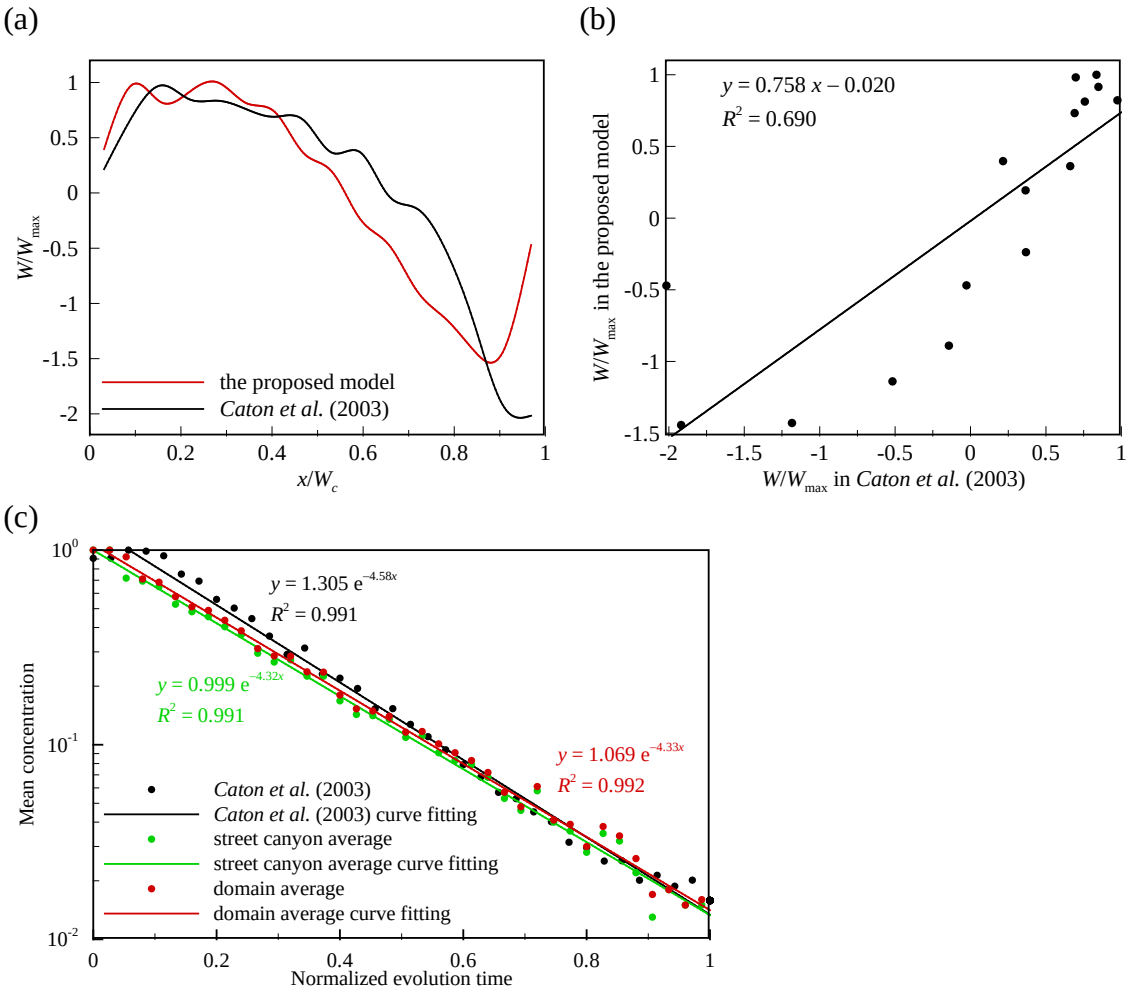

Figure 2.2. Comparisons of simulated results against water channel experiment by Caton, Britter, and Dalziel (2003): (a) profiles of the vertical wind velocity at the canyon top, (b) correlation between two profiles, and (c) a transient experiment. The canyon aspect ratio is $H/W_c = 1.0$, and particles were released from the center of the road. In the water channel experiment, the building height was 7 cm, and the canyon length was 30 cm. In the coupled LES–LSM simulations, the building height is 10 m, the canyon length is infinite, and friction velocity $u_* = 0.4$ m s^{-1}. All spatially averaged concentrations are normalized by their respective maxima in (c).

Additional comparisons are made between the model predictions and a wind tunnel experiment done by Tominaga and Stathopoulos (2011). Tominaga and Stathopoulos (2011) used a square canyon (H/W_c = 1.0) consisting of two blocks with finite spanwise length (2H), where particles (Ethylene) were continuously released from the center of the road. The time-averaged concentration was also simulated using RANS and LES models in their study. Here we use a single street canyon similar to that in their experiment and simulate the 3D dispersion of pollutants. Note that different from the setups described in Section 2.1.2, the LSM domain is 3D in this comparison. Figure 2.3 shows the concentration comparisons at the center line of the street canyon along the streamwise direction. The general patterns of model predictions are in line with measurements at three different canyon levels (R^2 > 0.825). Nevertheless, small discrepancies are still observed between their observational data and our simulations, especially at the bottom level. For example, our model shows a relatively higher concentration at the windward side, while the windward-side pollutant concentration is close to zero in the study conducted by Tominaga and Stathopoulos (2011). This is probably due to some minor differences of flow field between the wind tunnel experiment and our model simulations, as numerically reproducing the identical flow boundary conditions could be extremely difficult. Furthermore, it is noteworthy that there are also noticeable disparities between wind tunnel measurements and numerical simulations using RANS and LES in their study, while our model successfully captures the concentration peak near the windward wall (x/W_c = ~1.0, see Fig. 2.3a and c).

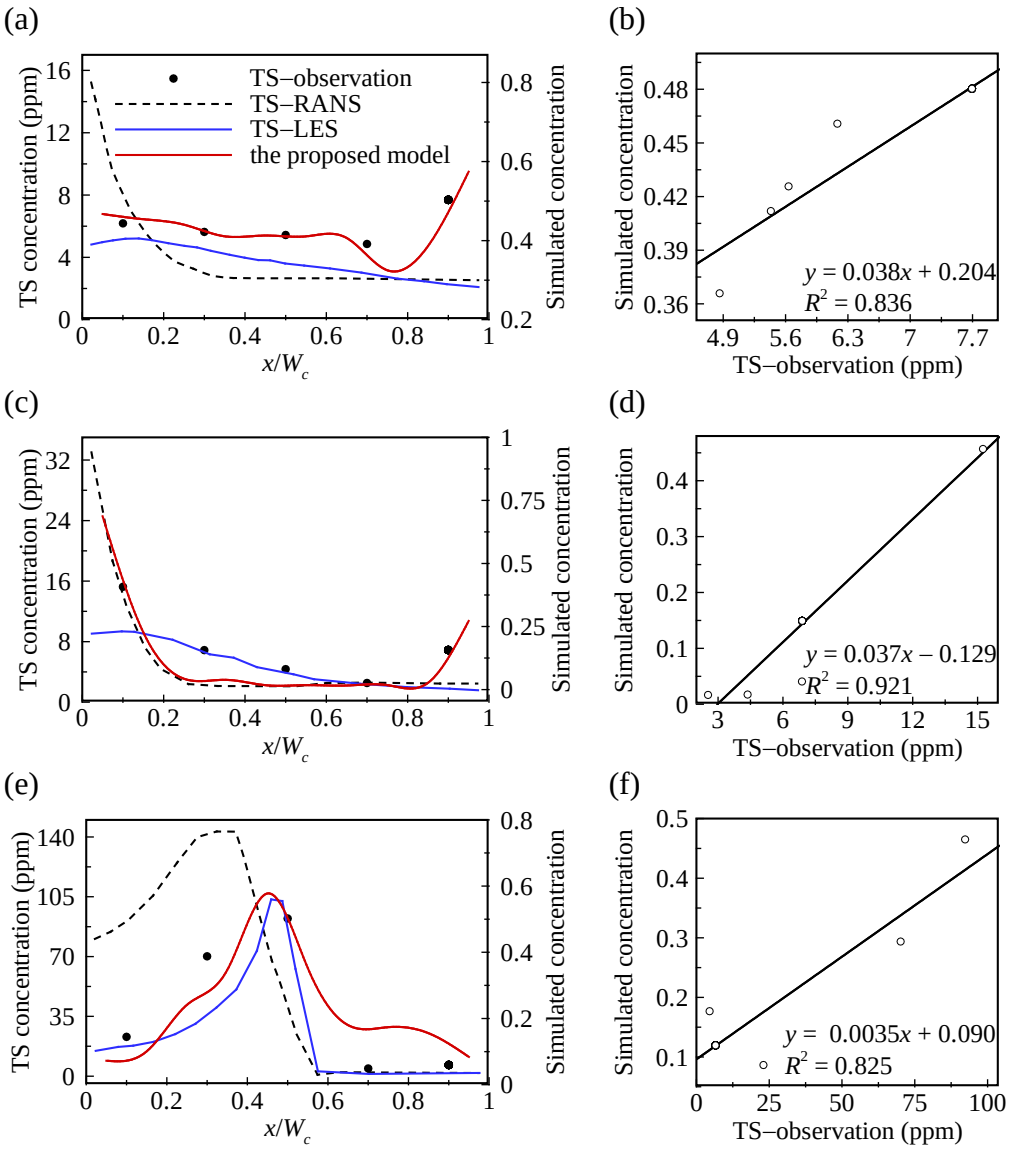

Figure 2.3. Comparisons of simulated pollutant concentrations inside the street canyon against results from Tominaga and Stathopoulos (2011) (denoted as TS in this figure) at (a) and (b) top level (1.0*H*), (c) and (d) middle level (0.5*H*), and (e) and (f) bottom level (0.1*H*). The canyon aspect ratio H/W_c = 1.0, and particles were released from the center of the road. In the wind tunnel experiment, the canyon length was twice the building height, and the concentration of emission gas was 1000 ppm. In the coupled LES–LSM simulations, the building height is 10 m, the canyon length is 20 m, and friction velocity

u_* = 0.4 m s^{-1}. Results of the proposed model have been normalized by the maximum concentration.

2.3. Results and Discussion

For better clarity, we divide the street canyon into seven zones (Fig. 2.1c) and evaluate the normalized zonal concentrations $\overline{c}_{zone}$ for all cases, which is defined as

$$\overline{c}_{zone} = \frac{\sum_{i=1}^{nz} \overline{c}_i}{x_z z_z / \left(x_0 z_0 \right)}, \tag{2.12}$$

where x_z and z_z are dimensions of each zone, and $\overline{c}_i$ is the normalized concentration within each $x_0 \times z_0$ grid cell (x_0 and z_0 being unity). The number of such grid cells in each zone is *nz*, which can be calculated as $x_z z_z / (x_0 z_0)$. The pedestrian level zone (a $W_c \times 2$ m zone above the ground) and two sidewalk zones (2 m × 2 m square-shaped zones at canyon corners) are extremely important for assessment of pedestrian exposure to pollutants. Two wall zones show the pollution level near walls, suggesting possible exposure through windows. Canyon zone is to evaluate the overall pollution level. The rooftop zone indicates the impact outside street canyons.

The spatial distributions of the normalized pollutant concentrations (see Eq. (2.11)) and zonal concentrations (see Eq. (2.12)) are showed in Figs. 2.4–2.7, for canyon aspect ratio H/W_c = 1.0, 0.2, 0.5, and 5.0, respectively. Figs. 2.8–2.11 show the normalized streamwise wind velocity and mean circulations in all cases, and Figs. 2.12–2.15 show the profiles of normalized streamwise and vertical wind velocity components at different parts inside street canyons. The percent changes of normalized zonal

concentration in each case (as compared to the control, i.e., NoTree case) are summarized in Table 2.3. We mainly focus on H/W_c = 1.0 cases in Section 2.3.1, and other cases in Section 2.3.2. Further implications of the results are discussed in Section 2.3.3.

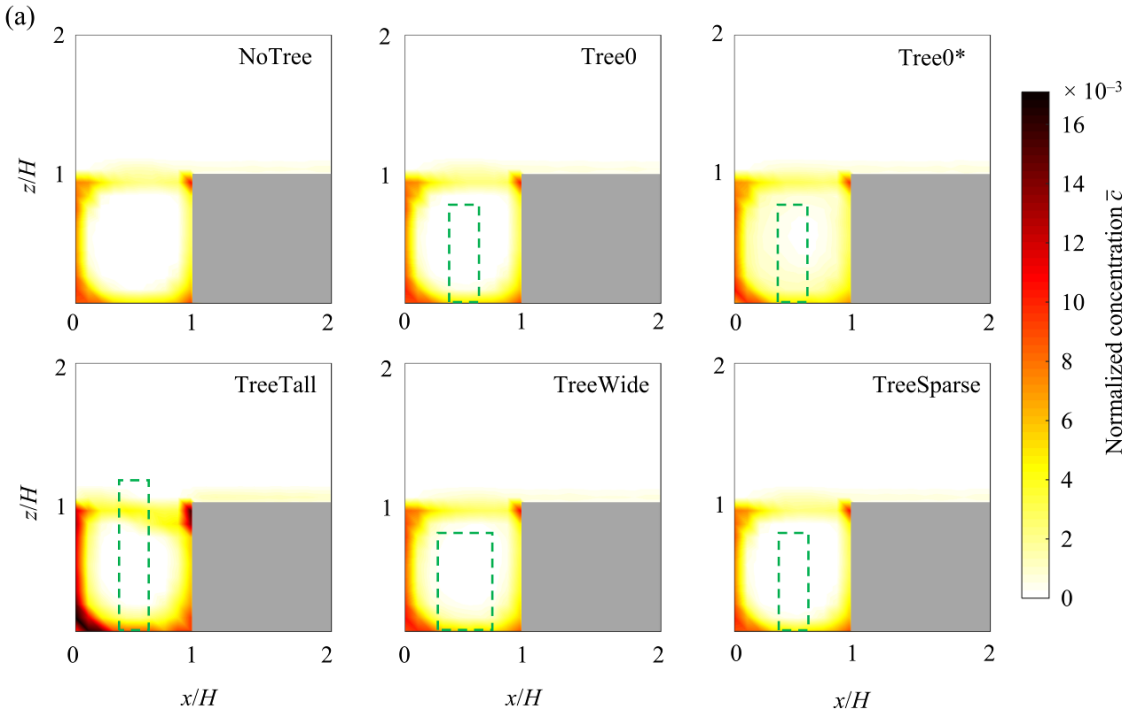

(b)

	Leeward wall	Windward wall	Pedestrian level	Leeward sidewalk	Windward sidewalk	Street canyon	Rooftop
NoTree	7.719	4.930	4.764	8.182	6.109	2.307	0.634
Tree0	8.067	5.036	5.034	8.557	6.141	2.449	0.637
Tree0*	8.066	4.421	4.869	8.286	5.130	2.769	0.676
TreeTall	12.663	8.259	8.085	13.584	8.289	4.151	1.249
TreeWide	8.696	5.190	5.369	9.207	6.018	2.814	0.631
TreeSparse	7.986	4.988	4.869	8.403	6.154	2.386	0.668

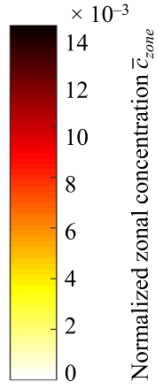

Figure 2.4. Results of normalized concentrations for cases with H/W_c = 1.0: (a) normalized concentration and (b) normalized zonal concentration. The green boxes mark the positions of modeled tree canopies.

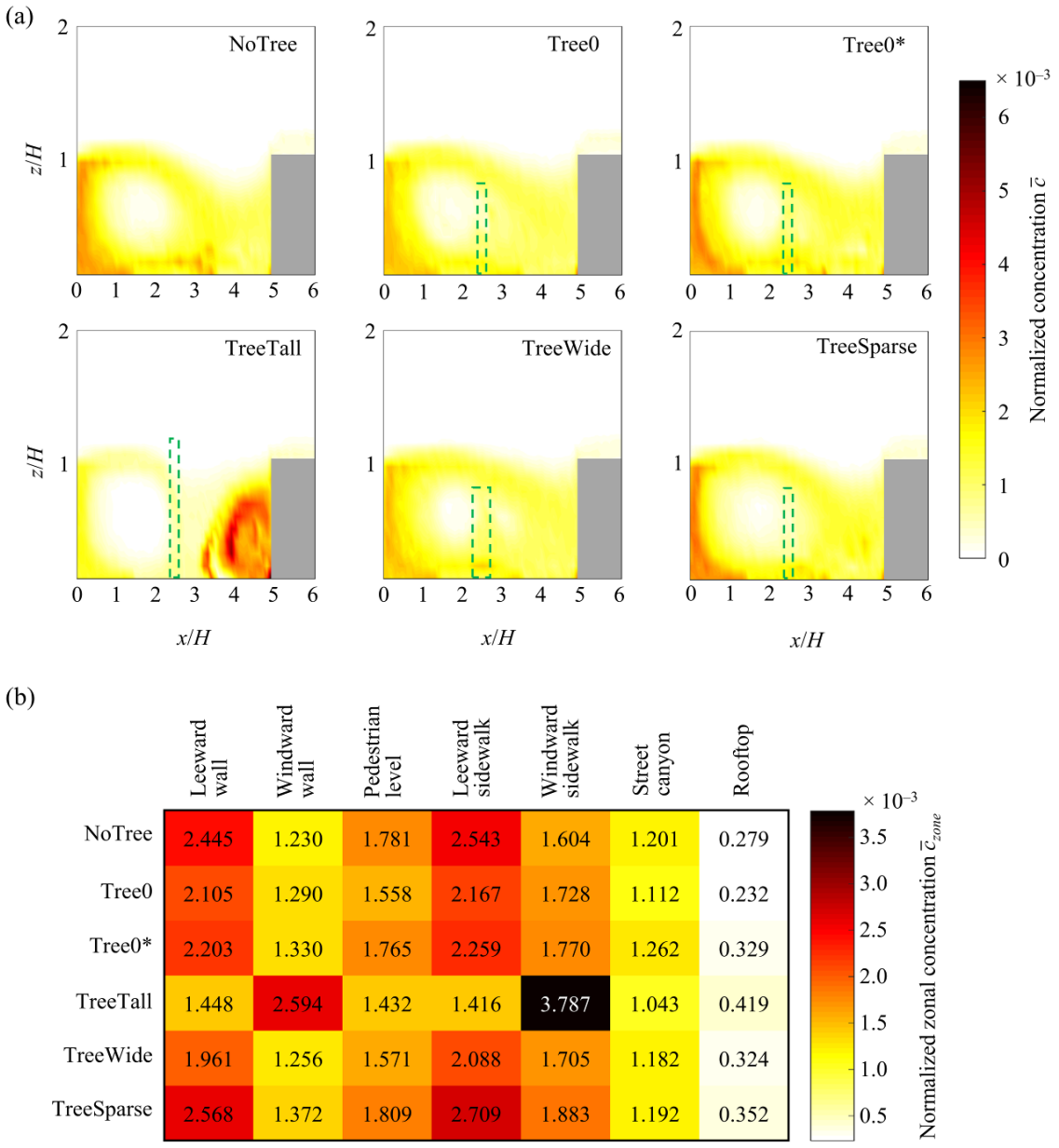

Figure 2.5. Results of normalized concentrations for cases with H/W_c = 0.2: (a) normalized concentration and (b) normalized zonal concentration. The green boxes mark the positions of modeled tree canopies.

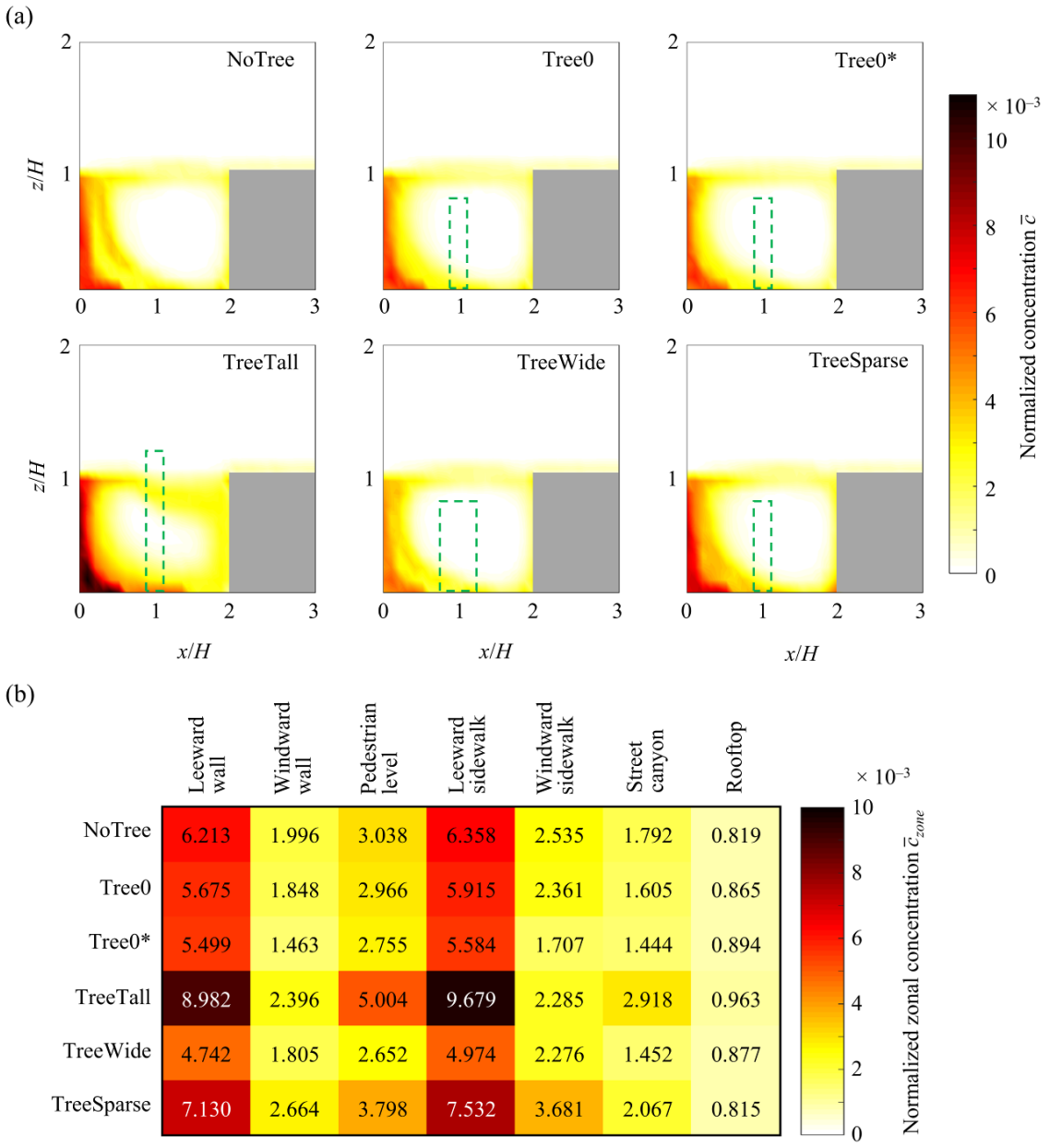

Figure 2.6. Results of normalized concentrations for cases with H/W_c = 0.5: (a) normalized concentration and (b) normalized zonal concentration. The green boxes mark the positions of modeled tree canopies.

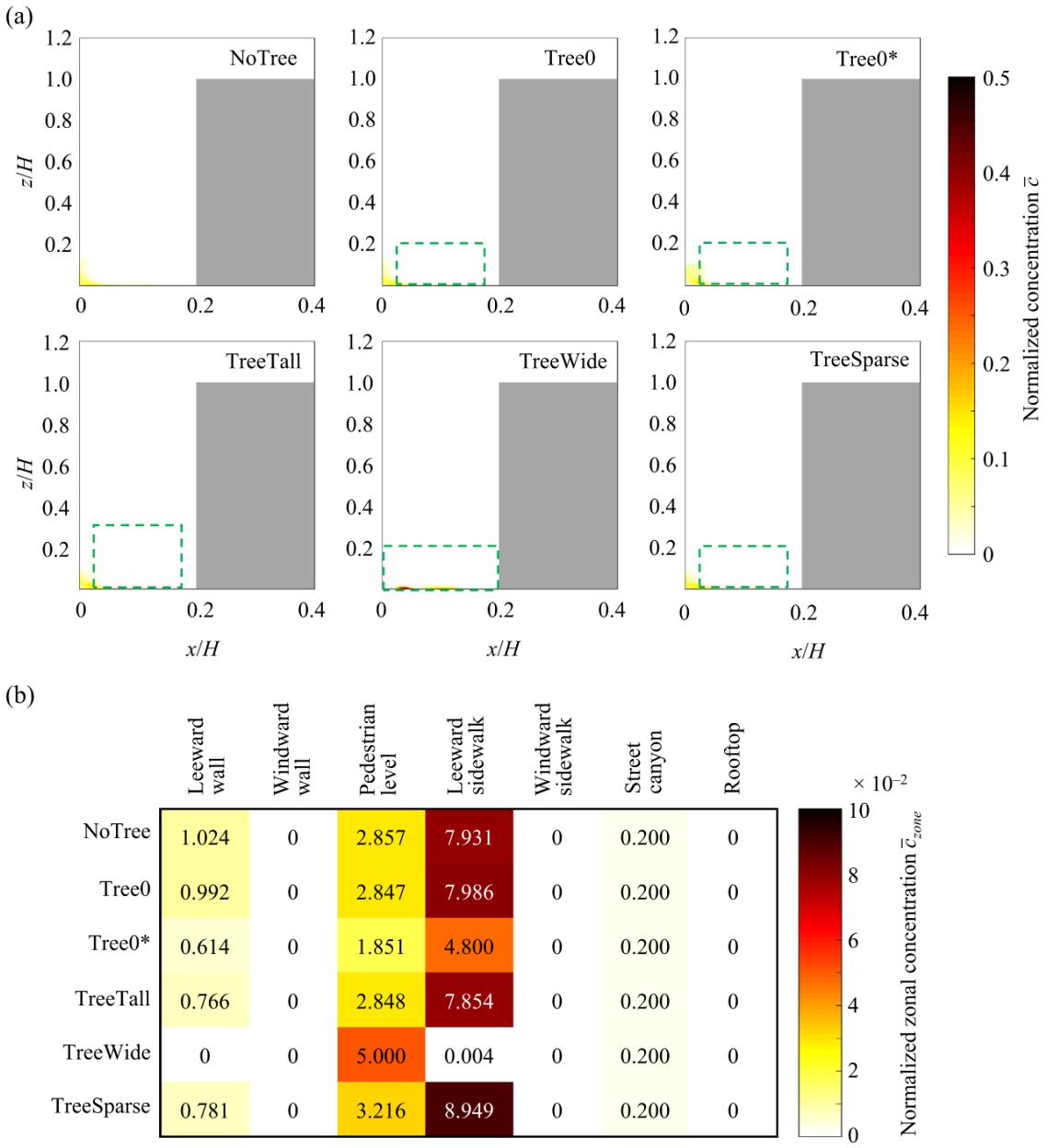

Figure 2.7. Results of normalized concentrations for cases with H/W_c = 5.0: (a) normalized concentration and (b) normalized zonal concentration. The green boxes mark the positions of modeled tree canopies.

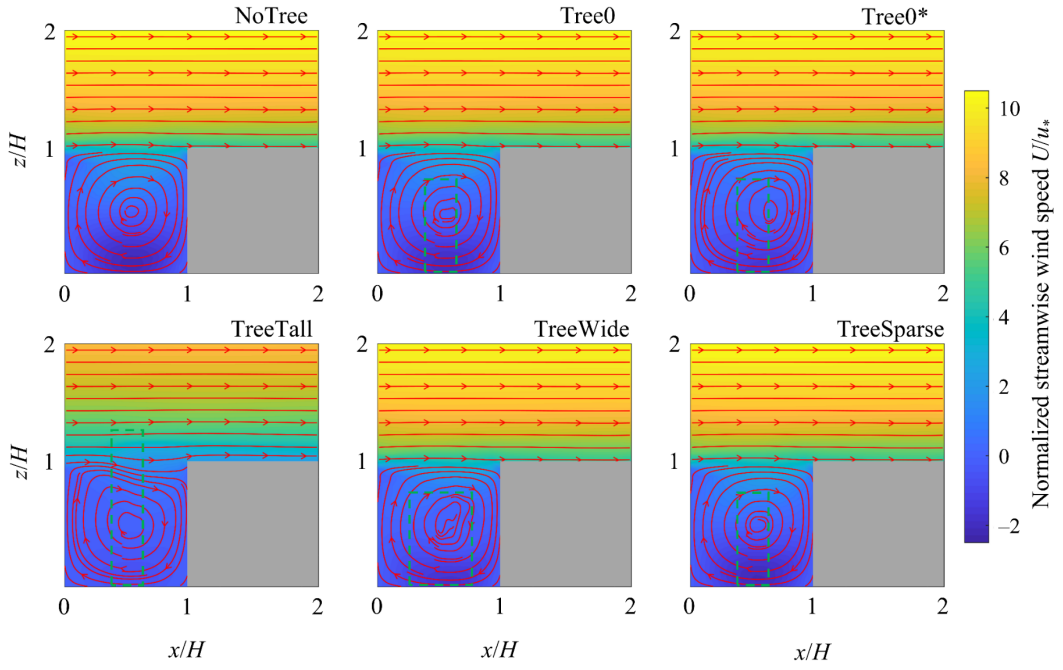

Figure 2.8. Normalized streamwise wind velocity and mean circulations for cases with H/W_c = 1.0. The green boxes mark the positions of modeled tree canopies.

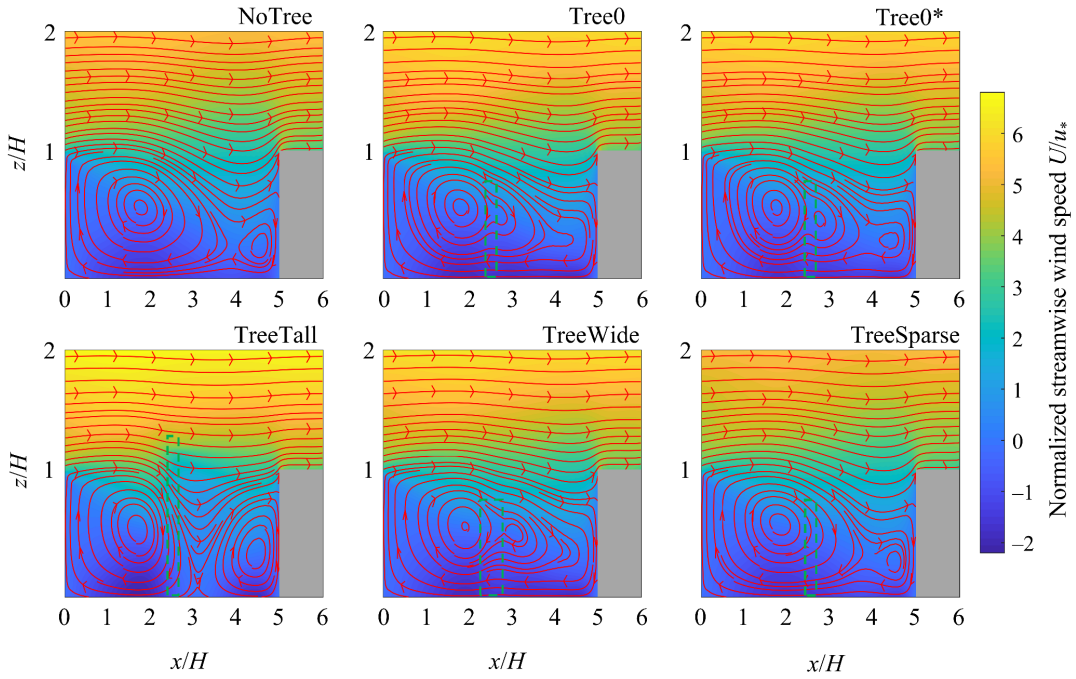

Figure 2.9. Normalized streamwise wind velocity and mean circulations for cases with H/W_c = 0.2. The green boxes mark the positions of modeled tree canopies.

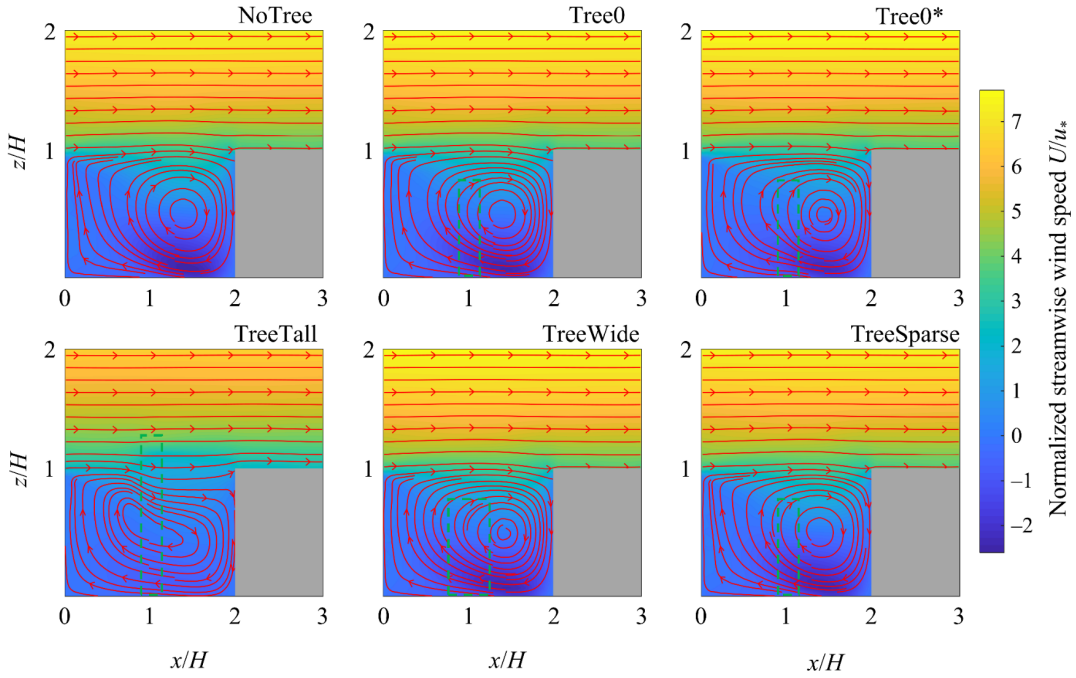

Figure 2.10. Normalized streamwise wind velocity and mean circulations for cases with H/W_c = 0.5. The green boxes mark the positions of modeled tree canopies.

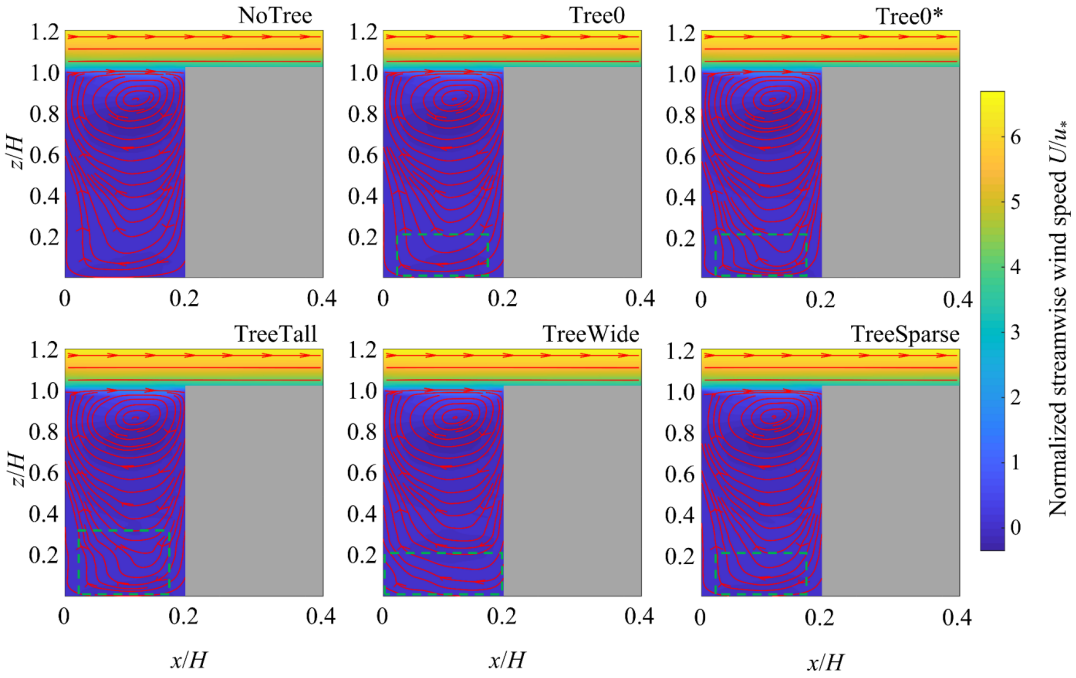

Figure 2.11. Normalized streamwise wind velocity and mean circulations for cases with H/W_c = 5.0. The green boxes mark the positions of modeled tree canopies.

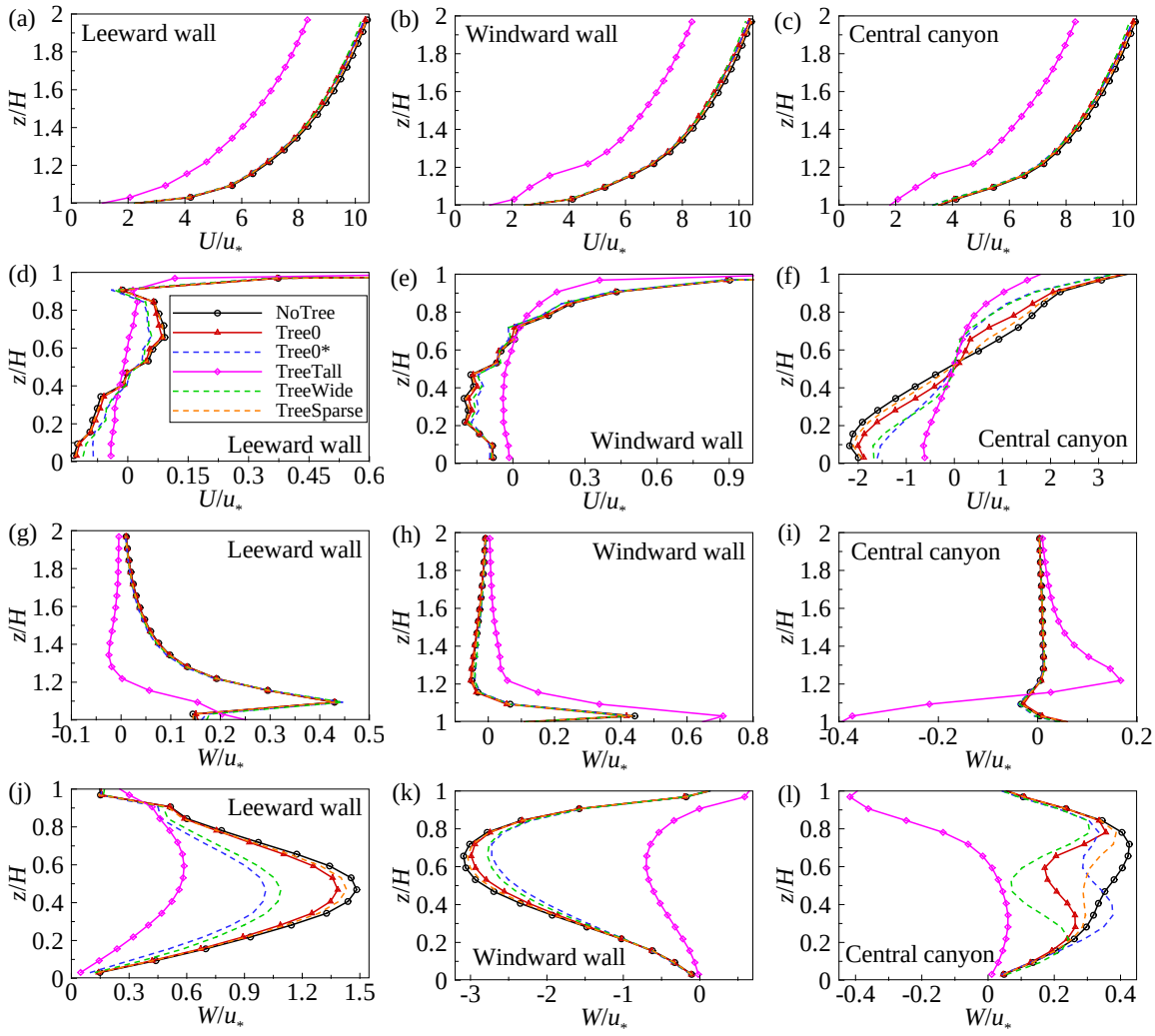

Figure 2.12. Vertical profiles of normalized streamwise and vertical wind velocities in different cases with H/W_c = 1.0: normalized streamwise wind velocity (a) and (d) near the leeward wall, (b) and (e) near the windward wall, (c) and (f) at the canyon center, and normalized vertical wind velocity (g) and (j) near the leeward wall, (h) and (k) near the windward wall, (i) and (l) at the canyon center.

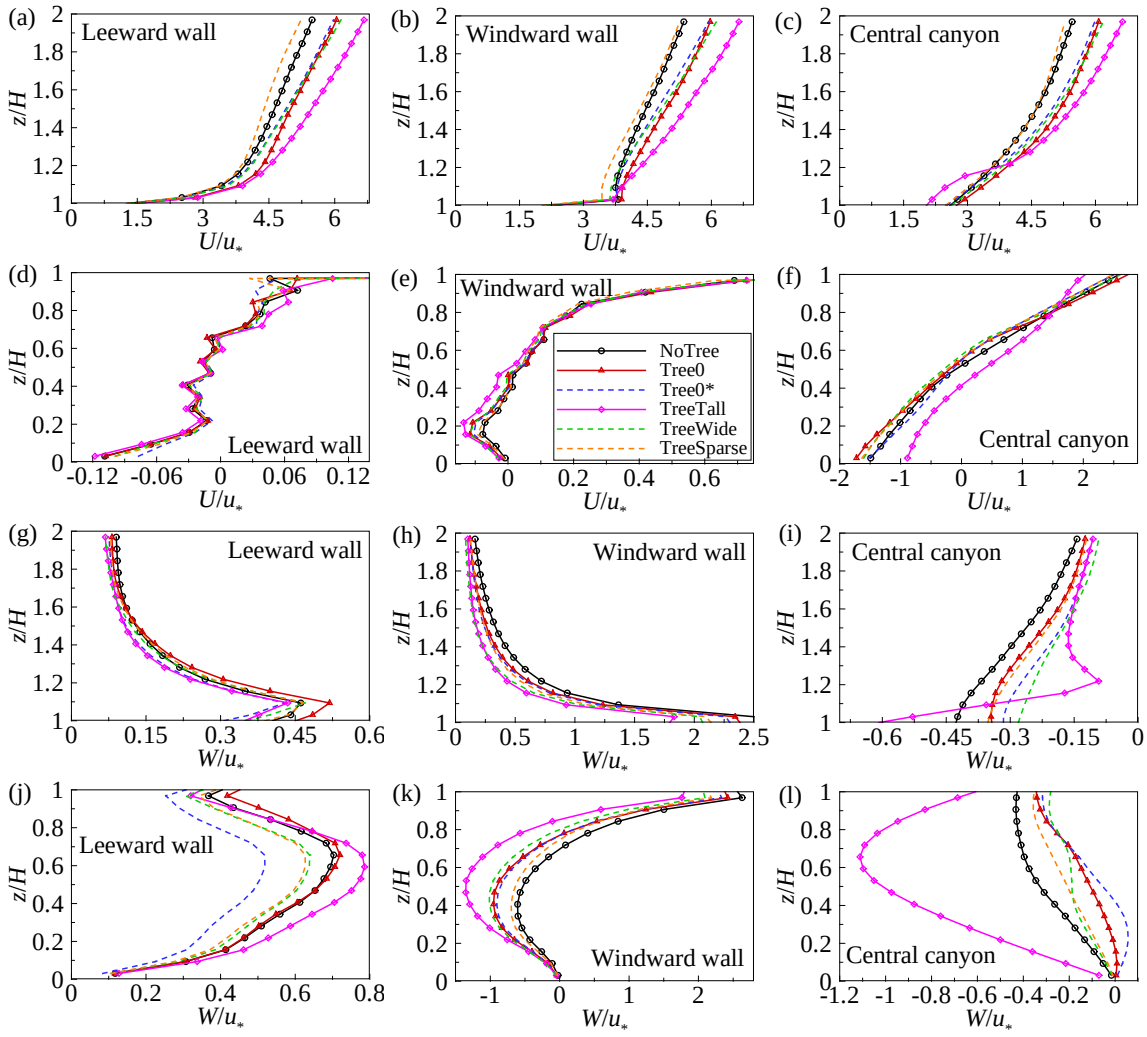

Figure 2.13. Vertical profiles of normalized streamwise and vertical wind velocities in different cases with H/W_c = 0.2: normalized streamwise wind velocity (a) and (d) near the leeward wall, (b) and (e) near the windward wall, (c) and (f) at the canyon center, and normalized vertical wind velocity (g) and (j) near the leeward wall, (h) and (k) near the windward wall, (i) and (l) at the canyon center.

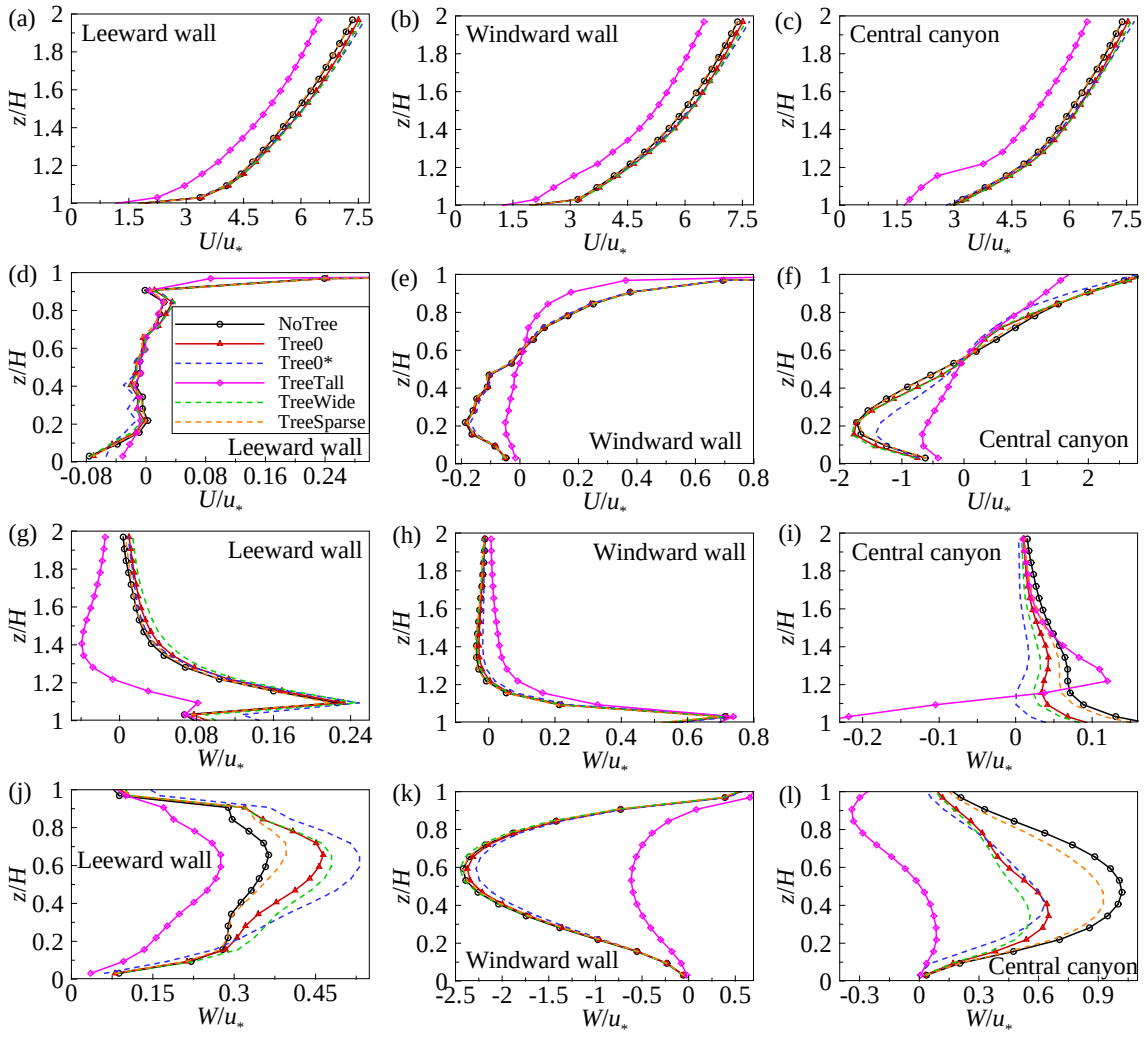

Figure 2.14. Vertical profiles of normalized streamwise and vertical wind velocities in different cases with H/W_c = 0.5: normalized streamwise wind velocity (a) and (d) near the leeward wall, (b) and (e) near the windward wall, (c) and (f) at the canyon center, and normalized vertical wind velocity (g) and (j) near the leeward wall, (h) and (k) near the windward wall, (i) and (l) at the canyon center.

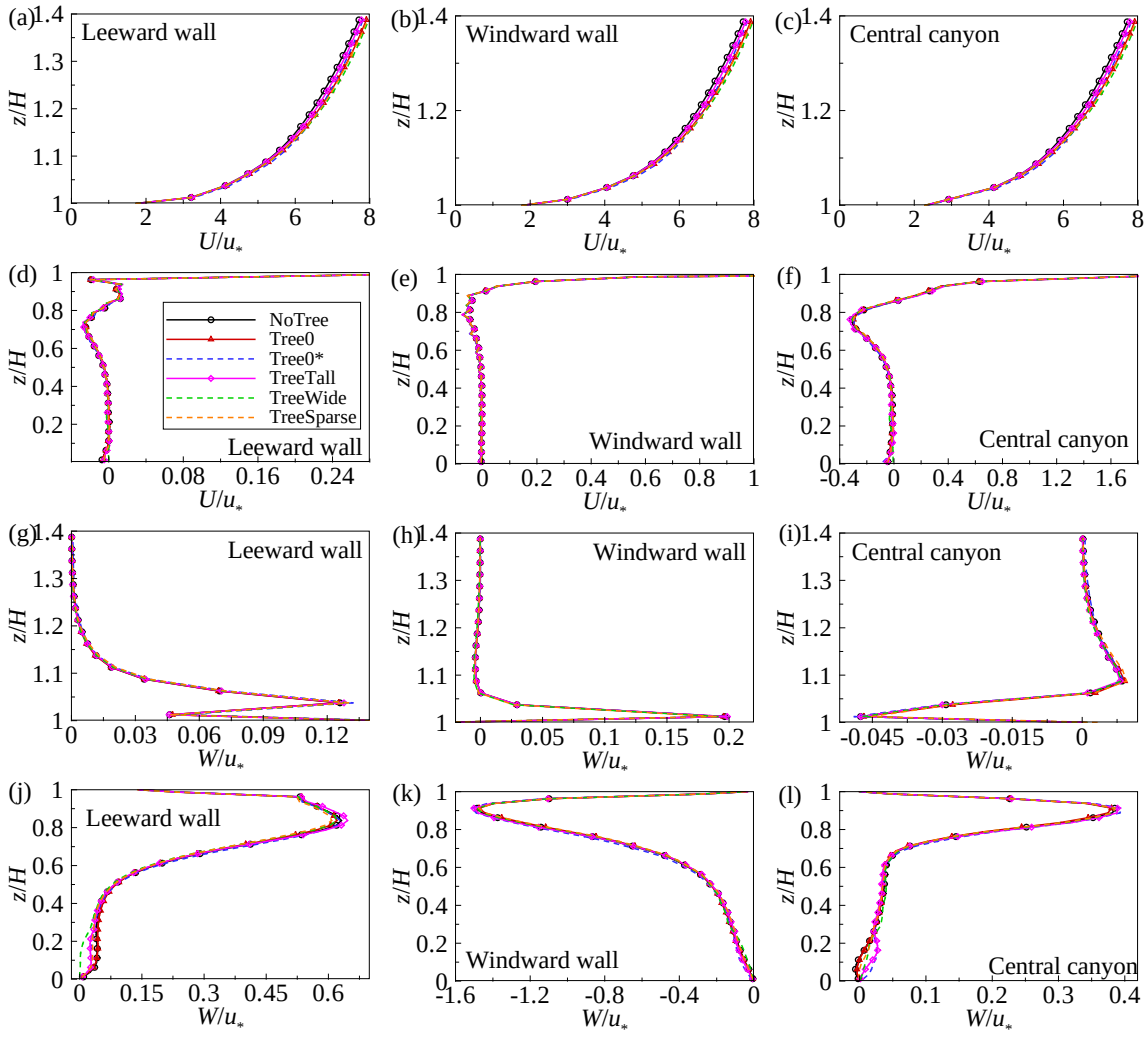

Figure 2.15. Vertical profiles of normalized streamwise and vertical wind velocities in different cases with H/W_c = 5.0: normalized streamwise wind velocity (a) and (d) near the leeward wall, (b) and (e) near the windward wall, (c) and (f) at the canyon center, and normalized vertical wind velocity (g) and (j) near the leeward wall, (h) and (k) near the windward wall, (i) and (l) at the canyon center.

Table 2.3. Changes (%) of normalized zonal concentration when compared with NoTree case

Cases	Leeward wall	Windward wall	Pedestrian level	Leeward sidewalk	Windward sidewalk	Street canyon	Rooftop
Canyon aspect ratio H/W_c = 1.0							
NoTree	0	0	0	0	0	0	0
Tree0	4.51	2.14	5.67	4.58	0.52	6.18	0.53
Tree0*	4.49	–10.33	2.21	1.27	–16.03	20.05	6.57
TreeTall	64.04	67.53	69.72	66.03	35.68	79.95	96.95
TreeWide	12.65	5.28	12.72	12.53	–1.50	21.98	–0.42
TreeSparse	3.45	1.17	2.22	2.71	0.74	3.43	5.31
Canyon aspect ratio H/W_c = 0.2							
NoTree	0	0	0	0	0	0	0
Tree0	–13.88	4.91	–12.53	–14.78	7.69	–7.36	–16.97
Tree0*	–9.87	8.13	–0.88	–11.14	10.34	5.15	18.04
TreeTall	–40.78	110.92	–19.60	–44.31	136.05	–13.09	50.06
TreeWide	–19.80	2.09	–11.77	–17.90	6.29	–1.57	16.01
TreeSparse	5.03	11.54	1.57	6.56	17.35	–0.69	26.05
Canyon aspect ratio H/W_c = 0.5							
NoTree	0	0	0	0	0	0	0
Tree0	–8.65	–7.40	–2.35	–6.97	–6.87	–10.43	5.70
Tree0*	–11.50	–26.72	–9.30	–12.18	–32.68	–19.46	9.24
TreeTall	44.56	20.06	64.74	52.23	–9.86	62.83	17.59
TreeWide	–23.68	–9.59	–12.69	–21.77	–10.22	–18.99	7.13
TreeSparse	14.76	33.45	25.04	18.45	45.20	15.33	–0.45
Canyon aspect ratio H/W_c = 5.0							
NoTree	0	0	0	0	0	0	0
Tree0	–3.16	0	–0.36	0.69	0	0	0
Tree0*	–40.02	0	–35.20	–39.48	0	0	0
TreeTall	–25.25	0	–0.30	–0.98	0	0	0
TreeWide	–100	0	75.03	–99.95	0	0	0
TreeSparse	–23.80	0	12.59	12.84	0	0	0

2.3.1. Effect of Tree Geometry on Street Canyon Pollutant Dispersion

The NoTree case with H/W_c = 1.0 (square canyon without trees) generates a skimming flow regime (Oke 1988b). The streamwise flow partially enters the canyon due to the pressure gradient, and flow separation occurs. When the outer airflow strikes the windward wall, part of it descends all the way to the road (the so-called "downwash"), turns toward the leeward side, deflects upwards when encountering the leeward wall, and recirculates, forming a nearly de-coupled vortex circulation in the canyon. Square canyons with trees show a similar recirculation forming, albeit with attenuated canyon circulation and slight shifts of rotation center. The only exception is the TreeTall case, in which the protruding tree crown above the roof level significantly perturbs the shear layer roughly at the canyon top level ($z/H \sim 1$), generating a reinforced downward turbulent transport of high momentum fluid into the canyon space downwind the tree (Li and Wang 2018) (see Figs. 2.8 and 2.12i and l). Profiles of streamwise and vertical winds in Fig. 2.12 also reveal that changes of flow field in the TreeTall case are the most significant (Krayenhoff et al. 2015).

The canyon wind field is vital to the atmospheric dispersion and dilution of pollutants in the canopy layer. The reversed streamwise wind velocity carries tracers toward the leeward wall, while the vertical wind velocity is conducive to uplifting and ventilation. The analysis of zonal concentrations in the square NoTree case suggests that pollutants tend to be trapped within low-wind-velocity areas, i.e., the peripheries of the canyon facets. A relatively higher concentration at the leeward wall and sidewalk is observed when compared to their windward counterparts (Fig. 2.4). The leeward sidewalk is most susceptible to pollution, where the concentration is 33.9% higher than in

the windward sidewalk. Similar results have been reported in both wind tunnel experiments and numerical simulations (Cai, Barlow, and Belcher 2008; Gromke and Ruck 2009; 2007). In contrast to earlier studies, however, stagnant concentration around the upper corner of the windward wall (hereafter “upper windward corner”) was detected. In the present study, the primary vortex is relatively isolated, and the corner spiral vortices at the end of canyon are neglected (cf. Fig. 4 in Gromke and Ruck (2007)). As a result, pollutant cannot be effectively diluted by lateral wind velocity. This inadequacy in resolution of longitudinal vortices renders the upper windward corner a nearly stagnation point, which, when coupled to the LSM, in turn leads to a (probably) “incorrectly too high” (Lanzani and Tamponi 1995) concentration. It should be noted that when the spanwise canyon length is not infinite, corner eddies play an important role in adding additional ventilation and diluting pollutants. In addition, rooftop area has a much lower concentration if compared to the street canyon, as the escaped pollutant is quickly transported and diluted as a result of the strong shear layer immediately above the canyons (Li and Wang 2018).

The presence of trees can aggravate the canyon air pollution for all square-canyon cases (see Fig. 2.4 and Table 2.3) mainly due to the reduced wind velocity, as suggested by field measurements in different cities (Jeanjean et al. 2017; S. Jin et al. 2014). The TreeTall case in the square canyon presents the most significant modifications to zonal concentrations, and the mean canyon concentration increases by 80.0% than that in the NoTree case (Table 2.3). The attenuated upward wind velocity on the leeward side above the canyon also contributes to trapping pollutants. The protruding tree crown generates stronger updrafts near the windward wall at the canyon top which pumps pollutants

upwards, leading to a nearly doubled concentration on the rooftop. The trapping effect also manifests in other tree cases in square canyons, resulting in increased pollution near the leeward wall and at the pedestrian level. Different tree morphologies, as represented by LAD profiles, can alter the pollutant distribution at the canyon bottom. Due to the higher LAD near the road (Li and Wang 2018), Tree0* case substantially attenuates the horizontal and vertical airflows (Fig. 2.12d, e, j, and k) and therefore the pollutant transport toward the windward side, resulting in much lower windward concentrations (Fig. 2.4b). The mean concentration at windward sidewalk decreases by 16.0% in Tree0* case (Table 2.3). Similar patterns also exist in the TreeWide case. Likewise, TreeTall case attenuates pedestrian level wind velocities (Fig. 2.12d–f and j–l), which increases mean leeward sidewalk concentration by 66.0% than that in the NoTree case, but only rises mean windward sidewalk concentration by 35.7%. Furthermore, consistently higher concentration at the upper windward corner can be found in all square cases, showing the relatively stable isolation of the canyon vortex.

Different effects of trees on pollutant dispersion are manifest in wider street canyons. Trees in wide and broad canyons (H/W_c = 0.2 and 0.5) tend to alleviate pollution level inside canyons, while increase pollutant concentrations in the rooftop zone (Figs. 2.5, 2.6, and Table 2.3). When compared to the NoTree cases, the TreeTall cases consistently exhibit the most distinct changes of pollutant concentration. For example, we observe 13.1% reduction of mean canyon concentration in wide canyons (H/W_c = 0.2) but 62.8% increase in broad canyons (H/W_c = 0.5). For narrow canyons, however, the effect of wide trees is markedly distinctive by trapping most pollutants near the ground but leaving the leeward wall comparatively clear (Fig. 2.7). These diverse patterns are

attributed to altered flow fields with different urban geometry, as detailed in the following section.

2.3.2. Effect of Canyon Geometry on Street Canyon Pollutant Dispersion

The canyon geometry plays an important role in shaping the canyon flow pattern. As canyon becomes wider (H/W_c = 0.2 and 0.5), high concentration at the upper windward corner shown in square-canyon cases disappears, owing to the more intensive mass and momentum exchanges at the canyon top (see Figs. 2.1, 2.9, 2.10, 2.13, and 2.14) (Li and Wang 2018). The wide NoTree case (H/W_c = 0.2) features a strong pattern of isolated roughness flow (Oke 1988b), where a secondary vortex is formed in front of the windward wall, interacting with the primary vortex. Strong downdrafts are observed within the wake zone of the upstream building even at the height of z/H = 2.0, as shown in Figs. 2.9 and 2.13i and l. Pollutants are entrained mainly by the primary vortex, leading to higher concentrations at the leeward side, as shown in Fig. 2.5. Trees with high LAD (2.8 m^2 m^{-3}) act like bluff bodies embedded inside wide canyons, and accelerate the outer streamwise flow (Fig. 2.13a–c). The enhanced outer airflow sweeps the pollutant emitted from the canyon at a faster rate, partially contributing to the decreased level of pollution at the leeward side and pedestrian level (Fig. 2.5). The most distinct dispersion patterns are found in the TreeTall case with the maximum LAD at the roof level. As the outer streamwise airflow approaches tall tree crowns, the flow deviates vertically over the crown and enters into the canyon, forming a narrower vortex between trees and the leeward wall (Fig. 2.9). The flow passing the canopy is drawn into the canyon by lower pressure and then recirculates, generating a stronger secondary vortex as compared to

other wide-canyon cases. The lack of horizontal mass transport toward the leeward side near the canyon bottom, together with the highly isolated secondary vortex, is responsible for the heavy pollutant level on the windward side, especially at the windward sidewalk junction (Fig. 2.5). Similarly, the presence of dense tree canopies (LAD = 2.8 $m^2 m^{-3}$) enhances the secondary vortex and thus the downdraft along the lower windward wall (Fig. 2.13k), resulting in consistently high concentration on the windward side. In contrast, sparse trees with the lowest LAD and highest porosity, alter the flow mainly via form drag (Fig. 2.13a and b), leading to increased pollutant concentrations in the wide TreeSparse case.

In all broad canyons (H/W_c = 0.5), only the primary vortex is observed (Fig. 2.10). Similar to wide-canyon cases, dense tree canopies below the roof level accelerate the streamwise wind velocity above the canyon (Fig. 2.14a–c), reducing canyon pollutant concentrations by 10.4–19.5% (Table 2.3). Enhanced updrafts near the leeward wall further contribute to the decrease of pollutant concentration in Tree0, Tree0* and TreeWide cases (Figs. 2.6 and 2.14j). The presence of tall or sparse trees in the canyon, however, reduces the mean outer streamwise airflow and therefore impedes the ventilation. Tall trees, especially, substantially reduce both the streamwise and vertical transports in the (lower) canyon (Fig. 2.14d–f and j–l), inducing the most aggravated pedestrian level pollutant concentration among all broad-canyon cases.

The results of simulations for narrow canyons (H/W_c = 5.0) suggest that trees much lower than buildings slightly enhance the outer streamwise airflow (Fig. 2.15a–c), as adding porous media at the canyon bottom is equivalent to decreasing the canyon aspect ratio. Likewise, the modifications to streamwise wind velocity inside canyons are

marginal (Figs. 2.11 and 2.15). Extremely low wind velocity presents at the bottom, retarding the atmospheric dispersion of pollutants. Although notable variability in dispersion can be found among some cases with different tree morphology (Fig. 2.7b and Table 2.3), pollutants are essentially trapped within the bottom area of narrow cases, while the windward side remains relatively unpolluted (Fig. 2.7).

2.3.3. Implications for Urban Planning of Environmental Quality

The results of simulations, in line with findings in previous studies, suggest that whether trees aggravate or alleviate pollutant concentrations depends on the geometry of street canyons and trees (Abhijith et al. 2017). While the impact of trees in square canyons is often adverse on ventilation and pollutant dispersion, dense trees below the roof level can in general improve the canyon air quality in broad canyons ($H/W_c = 0.5$). The two-fold effect is informative to urban stakeholders such as planners, resource managers, policy makers, residents, etc. For a symmetric square canyon, albeit beneficial in providing shade and improved outdoor thermal comfort, urban trees nevertheless can potentially degrade environmental quality with elevated concentrations of traffic-emitted pollutants at the pedestrian level (Gromke and Blocken 2015). In addition, higher pollutant concentrations near walls due to the presence of trees can induce indoor air pollution through natural/forced building ventilation systems. In contrast, for wide canyons ($H/W_c = 0.2$), dense and high trees are beneficial to mitigating exposure risks. Ventilation through windows should be reduced for walls facing the prevailing wind direction and alternatively, indoor ventilation systems can be used. For broad canyons ($H/W_c = 0.5$), tall trees and low-porosity trees impose potential risks of pollution. Toward

alleviating the pollution exposure risk at the pedestrian-level, urban trees should be avoided in square canyons, although minimal increases of concentration (< 2.3%) are observed in Tree0* and TreeSparse cases. Dense trees taller than building height (in TreeTall case) substantially reduce the concentration by 19.6%, being the optimal selection among wide-canyon cases. In broad canyons, the use of dense trees with a larger crown size (in TreeWide case) is the most suitable one, which brings down the concentration by 12.7%.

Narrow canyons exemplify a typical urban morphology that is susceptible to extremely high pollutant concentration near the ground surface. It should be noted that all cases tested in this study are limited to approach-wind perpendicular to the canyon. Previous research, however, has shown that approach-wind parallel to the street canyon is able to effectively dilute canyon pollution (Gromke, Jamarkattel, and Ruck 2016). Considering the natural ventilation through parallel airflow is thus necessary in urban design for areas with high-rise buildings. Furthermore, the comparison between Tree0 and TreeSparse cases indicates that trees with seasonality in foliage might manifest distinct influences on canyon air pollution, signaling the importance of a more integrated understanding when choosing urban tree species.

2.4. Concluding Remarks

A coupled LES–LSM modeling framework was developed in this chapter to assess the effects of trees on pollutant dispersion within street canyons. We analyzed a set of 24 cases with various tree and canyon geometries, with continuously released sources mimicking traffic-emitted pollutants. Trees taller than the building height show the most

significant modifications to both flow field and distribution of pollutant concentration in relatively wide canyons. Consistently higher pollutant concentration is observed on the leeward side in bare street canyons. Due to the presence of isolated vortex, trees attenuate the airflow and aggravate the pollution level in square canyons. Dense trees in wide canyons are able to reduce pollutants by enhancing canyon vortices and outer airflow. Tall or sparse trees in broad canyons exhibit strong trapping effects, while other tree geometries can strengthen the ventilation. Strongest pollutant trapping effects are observed in narrow canyons, as trees only marginally alter the canyon flow field.

It is noteworthy that only the neutral condition was considered in this study. It will be crucial for future research effort to include other (stable/unstable) atmospheric stratification, as well as interactions of thermal-flow fields such as the inclusion of buoyancy-induced convection. We only considered approach-wind perpendicular to the canyon, while other wind directions/canyon orientations may yield different dispersion patterns. In addition, geometric representation of urban trees is still primitive, neglecting e.g., complex interactions between airborne pollutants and leaves. Further development of the coupled LES–LSM modeling framework necessarily calls more realistic representation of biophysical and phonological functions of urban trees and their roles in regulating air quality in cities, such as direct emission of VOCs by trees, and wet/dry depositions on leaves with mixed convection. Nevertheless, the proposed modeling framework and its applications in the current study shed some new light on the impact of urban and tree morphologies, though simplistically represented, on the atmospheric dispersion of traffic-emitted pollutants. The modeling-based findings here are informative to stakeholders such as urban planners, policy makers, landscape managers, and the

general residents in cities in promoting their awareness of the participatory roles of trees in environmental quality.

CHAPTER 3

LARGE-SCALE EFFECT OF SHADE TREES ON URBAN HYDROCLIMATE AND PEDESTRIAN THERMAL COMFORT

Exacerbated heat stress has resulted in a series of environmental issues in urban areas. Mounting empirical evidence shows that urban trees are effective in mitigating the thermal stress in the built environment, whereas large-scale numerical simulations remain scarce. In this chapter, the effects of shade trees on the built environment are evaluated in all urban areas across the CONUS. The projected scenario is simulated using a coupled WRF-urban modeling system incorporating the radiative shading of urban trees. In particular, we evaluate the radiative shading of urban trees on urban temperature and relative humidity, as well as pedestrian thermal comfort during summers and winters. We also quantify the response of urban surface energy balance to the presence of shade trees.

3.1. Methodology

3.1.1. Integrated WRF-Urban Modeling System

The WRF model is a fully non-hydrostatic, compressible mesoscale model for numerical weather prediction and climate simulation (Skamarock et al. 2008). The WRF version 3.6.1 was used in this study, in conjunction with a single-layer UCM (Chen et al. 2011; Yang et al. 2016). The building arrays are represented in the UCM as a two-dimensional and longitudinally infinite street canyon (Yang et al. 2015). The shading effects of trees on radiative transfers in urban canopies were parameterized through modified view factors estimated by a stochastic ray-tracing method (Z.-H. Wang 2014b). The problem domain covers the entire CONUS (Fig. 3.1), which enables simultaneous

comparisons of multiple metropolitans. Moreover, CONUS was divided into six focus areas of concentrated megapolitans (subregions), i.e., Cascadia (subregion a), Great Lakes (subregion b), Northeast (subregion c), California-Arizona Sun Corridor (CA-AZ) (subregion d), Texas Triangle (subregion e), and Florida (subregion f), as shown in Fig. 3.1.

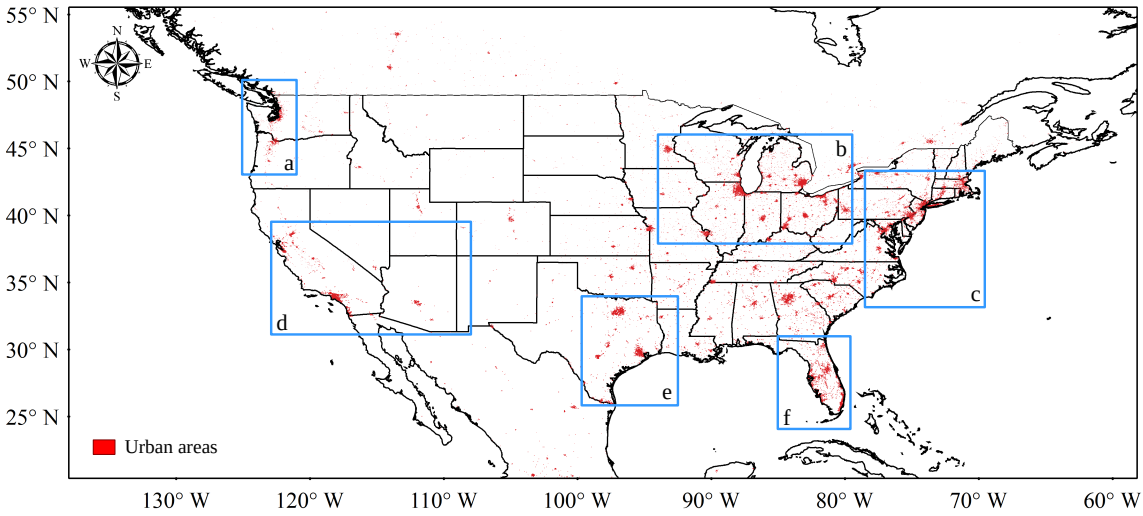

Figure 3.1. Model domain and urban areas in WRF simulations. Boxed are six focus areas: (a) Cascadia, (b) Great Lakes, (c) Northeast, (d) California-Arizona Sun Corridor (CA-AZ), (e) Texas Triangle, and (f) Florida.

The 1-km modified IGBP Moderate Resolution Imaging Spectroradiometer (MODIS) 20-category vegetation (land cover) data were used in the Noah LSM to represent the current land use/land cover conditions (see MODIS urban areas in Fig. 3.1). Daily FNL (Final) Operational Global Tropospheric Analysis data were retrieved from the National Centers for Environmental Prediction (2000) for the simulation period

(2012–2014), as the meteorological input to drive WRF simulations. These 6-hourly FNL data are from the Global Data Assimilation System (GDAS) with a 1° × 1° spatial resolution. All WRF simulations were carried out with a spatial resolution of 20 km and a time step of 60 s for integration. Large-scale forcings, including zonal wind, meridional wind, geopotential height, and potential temperature were nudged only above the planetary boundary layer using the spectral nudging technique (von Storch, Langenberg, and Feser 2000). The spectral nudging technique is to correct the systematic distortion of the large-scale flow for regional simulations (M. Wang et al. 2017). The top wave numbers to nudge are 4 and 3 in *x* and *y* directions, respectively. The physical schemes used in this study are summarized in Table 3.1.

Table 3.1. Parameterization schemes of surface and atmospheric physics used in WRF

Physics	Schemes
Microphysics	WRF double-moment 6-class scheme
Longwave radiation physics	Rapid radiative transfer model scheme
Shortwave radiation physics	Dudhia scheme
Surface layer	MM5 similarity scheme
Planetary boundary layer physics	Yonsei University scheme
Cumulus parameterization	Grell 3D scheme

A set of six simulations was conducted using WRF-UCM under two scenarios, viz., the control case (without trees) and the shaded case (with shade trees), implemented uniformly in all CONUS urban areas. The radiative shading effects of trees were

evaluated using the difference between the control and shaded scenarios by averaging the output hydrometeorological variables of one-year simulations. Each one-year simulation was carried out for 13 months, beginning from the last month (December) of the previous year, with the first month used as the spin-up period. Note that a comprehensive model validation can hardly be performed over the entire CONUS due to (i) the vast variability of the built environment at the continental scale, (ii) the paucity of observational data in many subregions, and (iii) the moderately coarse spatial resolution (20-km herein). Instead, the confidence of model performance and predictability skills of the numerical WRF-UCM platform are based on the numerous evaluations reported in previous studies. In particular, the application of the same set of parameterization schemes in this study (see Table 3.1) has been separately validated by M. Wang et al. (2017). Our recent study (C. Wang, Wang, and Yang 2019) using identical parameterization schemes but with a much finer resolution (5-km) over the CONUS has also suggested that the simulated 2-m air temperature and land surface temperature in summer 2012 matched reasonably well with measurements from 135 stations (both rural and urban) and remotely sensed data. For example, in the 2-m air temperature comparison, the overall Pearson's *r* and root mean square error (RMSE) were 0.926 and 2.16 °C, respectively, in this 5-km study (C. Wang, Wang, and Yang 2019). In addition, the use of online coupled WRF-UCM and offline UCM has been evaluated in multiple cities and at the regional scale, with the average RMSEs of simulated ambient temperatures around or less than 2 °C (Upreti, Wang, and Yang 2017; Z.-H. Wang 2014b; Ryu et al. 2016).

3.1.2. Numerical Representation of Urban Shade Trees

The thermal environment in cities is determined by the dynamics of energetics (Arnfield 2003; Oke 1988a). The fundamental understanding of the effects of shade trees on the urban surface energy balance is critical to the management of the thermal environment of cities. For a generic urban facet, the surface energy balance equation can be written as (Oke 1988a):

$$R_n + A_F = H + LE + G\,, \tag{3.1}$$

where $R_n = S^{\downarrow} - S^{\uparrow} + L^{\downarrow} - L^{\uparrow}$ is the net radiation, with S and L denoting the shortwave and longwave radiations, respectively, and upwelling and downwelling arrows for vertical directions; A_F is the anthropogenic heat; and H, LE, and G are the sensible, latent, and ground (conductive) heat fluxes, respectively.

The presence of urban trees alters all the energy budgets in Eq. (3.1), albeit via different pathways. As shown in Fig. 3.2 (and Fig. 1.2a), the presence of the 3D geometry of trees inside an urban canyon can effectively intercept and reflect both the shortwave (solar) and longwave (terrestrial) radiations, leading to the radiative *shading* and *trapping* effects, respectively. In fact, the participation of tree geometry in redistributing the net radiation R_n constitutes the primary cooling effect of trees (Upreti, Wang, and Yang 2017). As a response to the radiative shading, sensible and latent heat fluxes (H and LE) change due to the modified land surface temperature. Over a short time period (e.g., diurnal cycles), ground heat flux responds to the redistribution of net radiation with a reduced amount of heat transported downward (into building envelops and soils) during daytime, but enhanced upwelling transfer during nighttime (Upreti, Wang, and Yang

2017). Over the long run (e.g., annual means), the heat storage term remains relatively constant and insensitive to the presence of trees.

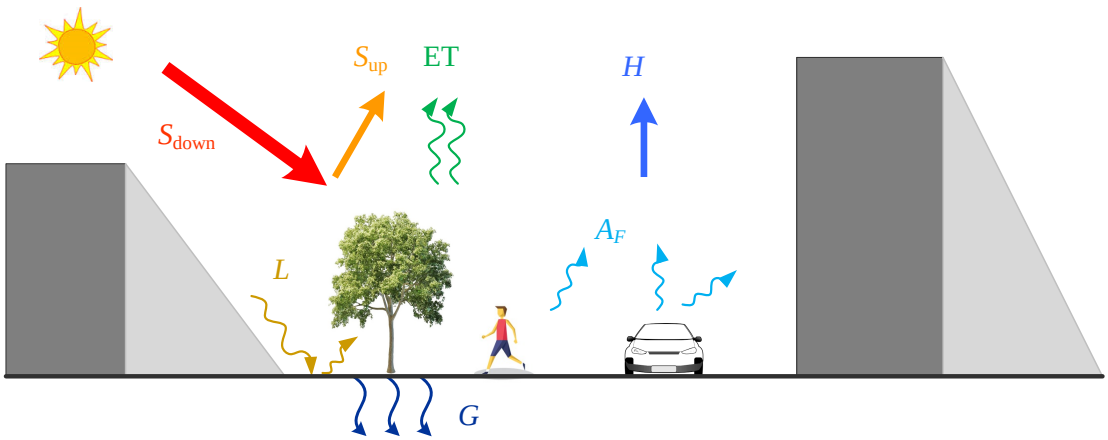

Figure 3.2. Schematic of the participatory role of urban trees in the urban land surface energy balance. S_{down} is the downward shortwave radiation; S_{up} is the upward shortwave radiation; L is the longwave radiation; ET is the evapotranspiration; H is the sensible heat flux; G is the ground heat flux; and A_F is the anthropogenic heat.

Physical representations of the complex thermal interactions between trees and street canyons are hitherto absent in the WRF-urban modeling system. For simplicity, the participation of trees in radiative heat exchange inside the street canyon was represented using two symmetric rows of trees with circular crowns in this study. The parameterization schemes in the single-layer UCM require inputs of uniform street canyon dimensions over CONUS, and the specified values are summarized in Table 3.2. A uniform geometric configuration of trees is applied in all urban areas. In this study, tree crowns above the roof level were not considered. Using MCS, the sky view factor (SVF,

the fraction of the sky visible from the ground) was calculated for both the control and shaded scenarios. The SVFs are 0.604 and 0.488 for the control and the shaded scenarios, respectively. The change of SVFs signals the reduction of net radiative heat exchange between the sky and the canyon ground. Note that the radiative view factors between any two canyon facets, in the absence of trees, can be determined analytically (Z.-H. Wang, Bou-Zeid, and Smith 2013), but need to be calculated case-by-case in the presence of trees using ray-tracing MCS (Ryu et al. 2016; Z.-H. Wang 2014b). The view factors with and without trees are summarized in Table 3.3.

Table 3.2. Geometric dimensions of street canyon and trees in the single-layer UCM

Variables	Values (m)	Calculation method and references
Road width, w	12.0	Combination of the suggested sidewalk width and the standard lane width in U.S. (AASHTO 2011; NACTO 2017)
Building height, h	6.3	Weighted mean building height in 12 North American cities (Schläpfer, Lee, and Bettencourt 2015)
Roof width, r	9.0	Informed by the default value in WRF model
Tree crown radius, r_t	1.0	Ensure the sufficient space between crowns and the adjacent wall facades (Erell, Pearlmutter, and Williamson 2011)

Table 3.3. Radiative view factors F_{ij} from facet *i* to *j*, with subscripts W, G, and S denoting wall, ground, and sky, respectively

View factors F_{ij} from facet *i* to *j*	Analytical without trees	MCS with trees
$SVF = F_{GS} = F_{SG}$	0.604	0.488
F_{WW}	0.249	0.141
$F_{SW} = F_{GW}$	0.197	0.116
$F_{WS} = F_{WG}$	0.375	0.200

3.1.3. Outdoor Thermal Comfort

Two thermal indices were adopted in this study to evaluate the effects of shade trees on modifying the outdoor thermal comfort, viz., the heat index (*HI*) and wind chill index (*WCI*). Both indices were derived based on the method given by National Oceanic and Atmospheric Administration's National Weather Service (NOAA 2007).

The *HI* was developed based upon extensive biometeorological studies, combining multiple parameters including vapor pressure, dimensions of a human, clothing cover, core temperature, sweating rate, etc. The *HI* is computed as (Rothfusz 1990):

$$\begin{aligned} HI = & -42.379 + 2.04901523T + 10.14333127R - 0.22475541TR \\ & -6.83783\times10^{-3}T^2 - 5.481717\times10^{-2}R^2 + 1.22874\times10^{-3}T^2R, \\ & +8.5282\times10^{-4}TR^2 - 1.99\times10^{-6}T^2R^2 \end{aligned} \tag{3.2}$$

where *T* is the ambient dry bulb temperature in °F, and *R* is the relative humidity (%). Adjustment is made to Eq. (3.2) when the relative humidity is extremely low (below 13%) or high (above 85%) (NOAA 2007). In this study, we used WRF model's

diagnostic 2-m air temperature and 2-m relative humidity (above the zero-plane displacement) to represent *T* and *R*, respectively.

The *HI* describes the subjective human feeling by coupling the actual air temperature and relative humidity. The *HI* is higher than the corresponding air temperature under high relative humidity. The National Weather Service relates *HI* to heat safety by classifying it into four degrees: extreme danger with likely heat stroke (over 54.4 °C, or 130 °F); danger with possible heatstroke and likely sunstroke, muscle cramps, and/or heat exhaustion (40.6–54.4 °C, or 105–130 °F); extreme caution for possible sunstroke, muscle cramps, and/or heat exhaustion (32.2–40.6 °C, or 90–105 °F); and caution for possible fatigue (26.7–32.2 °C, or 80–90 °F). Note that HI is only applicable when the air temperature is above 26.7 °C.

In contrast, the *WCI* was developed to evaluate the dangers of winter winds and temperatures with a human face model (NOAA 2007), given by:

$$WCI = 35.74 + 0.6215T - 35.75V^{0.16} + 0.4275TV^{0.16}, \tag{3.3}$$

where *T* is the air temperature in °F and *V* is the wind speed at the height of 1.52 m (5 ft, the average height of an adult human face) in miles per hour (mph). The wind speed can be derived from the 10-m wind speed measured by standard U.S. anemometers. In this study, the canyon wind speed predicted by WRF-UCM was directly adopted. Four degrees of *WCI* have been classified based upon the time of frostbite for people from 30 min to less than 5 min. The *WCI* is only applicable when the air temperature is below 4.4 °C. It is always lower than the actual air temperature, as wind intensifies the heat loss from human body to its surroundings. For example, when wind speed is 2.24 m s^{-1} at –9.4 °C, the *WCI* is –13.9 °C.

Note that three primary meteorological variables, viz., air temperature, relative humidity, and wind speed are used in the thermal comfort indices (*HI* and *WCI*) in this study. Nevertheless, the direct shading effect alone plays an important role in regulating outdoor thermal comfort. Here the direct shading effect refers to the blockage of solar radiation incident on human bodies, rather than through the reduction of ambient temperature. This effect is incorporated in many other thermal comfort indices, such as the mean radiation temperature (Epstein and Moran 2006), or physiological equivalent temperature (Höppe 1999), and needs to be further explored.

3.2. Evaluation of Model Uncertainty

We carried out two sets of sensitivity tests to characterize the model uncertainty of the proposed numerical framework. First, the sensitivity of radiative view factors was tested as a function of urban and tree morphologies using the ray tracing algorithm (Z.-H. Wang 2014b). Four geometric parameters were used to quantify the sensitivity of view factors between canyon facets and trees, viz., the canyon aspect ratio (h/w), the proximity of trees to buildings (x_t/w), the tree crown size (r_t/w), and the tree height (r_t/w). The latter three are all normalized by the road width w. The results are shown in Figs. 3.3 and 3.4. In general, all view factors are more sensitive to canyon aspect ratio and tree crown sizes than to the locations of trees. When the tree morphology is fixed, view factors between sky and ground (F_{GS}) and those between wall and sky/ground (F_{WS} or F_{WG}) decrease with the canyon aspect ratio; the opposite trend holds for the other two view factors (F_{SW} and F_{WW}). In addition, for the same canyon aspect ratio, all view factors decrease with tree sizes, as larger trees tend to impede radiative exchange between any pair of canyon

facets. It is also noteworthy that the sensitivity of view factors to all the geometric parameters exhibit certain degree of nonlinearity. Thus the application of linear approximation used for parameterizing view factors with presence of trees (e.g., Ryu et al. 2016) has limited applicability within a narrow range of urban/tree morphologies.

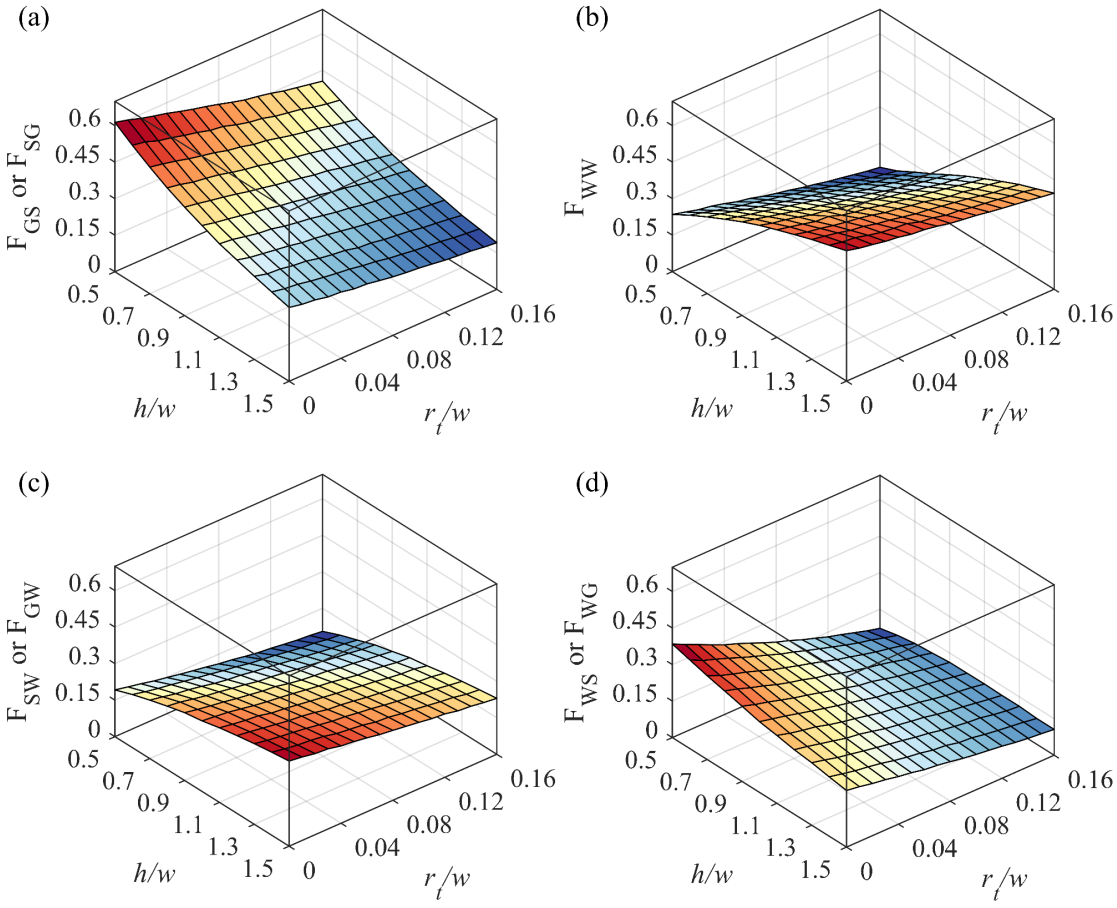

Figure 3.3. Sensitivity of view factors (a) F_{GS} or F_{SG}, (b) F_{WW}, (c) F_{SW} or F_{GW}, and (d) F_{WS} or F_{WG} to canyon aspect ratio (h/w) and normalized tree crown radius (r_t/w). The canyon width w and the height of tree crown center h_t are 12 m and 4 m, respectively. View factors F_{ij} is from facet i to j, with subscripts W, G, and S denoting wall, ground, and sky, respectively.

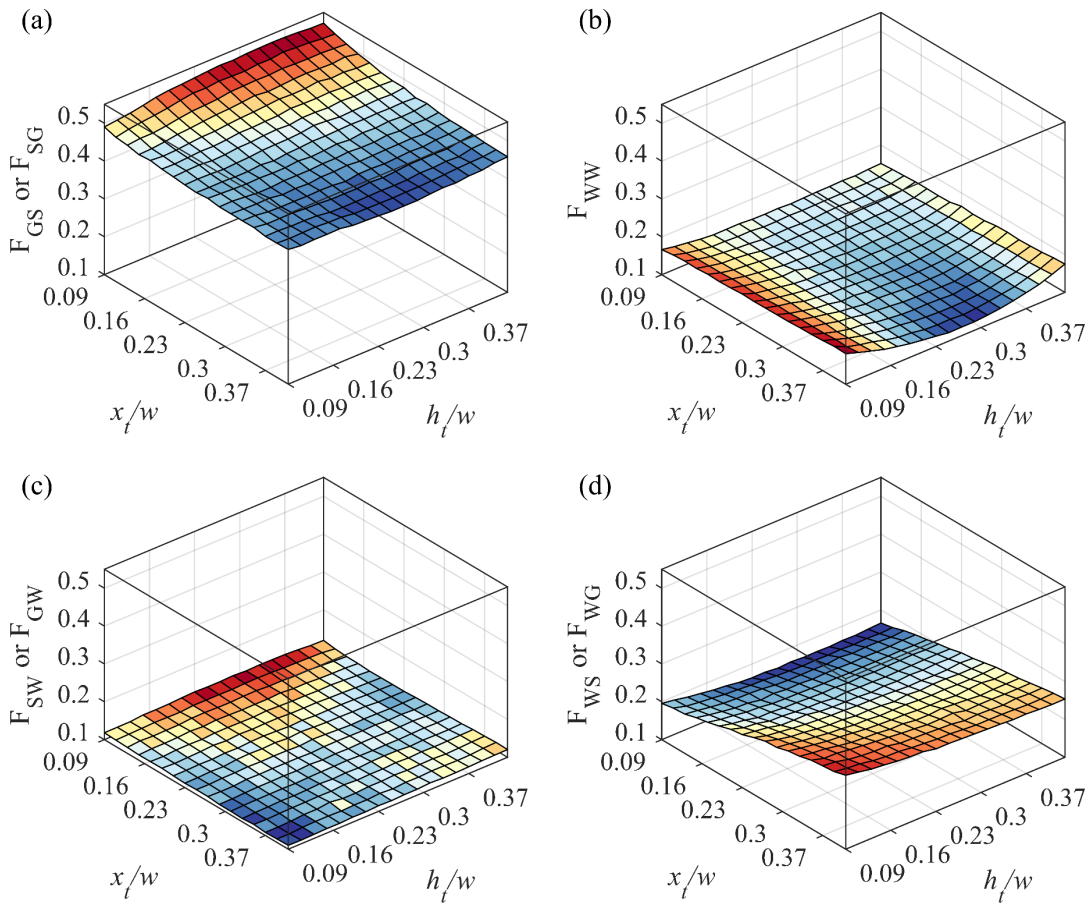

Figure 3.4. Sensitivity of view factors (a) F_{GS} or F_{SG}, (b) F_{WW}, (c) F_{SW} or F_{GW}, and (d) F_{WS} or F_{WG} to normalized tree crown height (h_t/w) and normalized proximity of trees to buildings (x_t/w). The canyon width w and the building height h are 12 m and 6.3 m, respectively. View factors F_{ij} is from facet i to j, with subscripts W, G, and S denoting wall, ground, and sky, respectively.

Second, the uncertainties in the output of online WRF-UCM was quantified with respect to the changing SVFs. We tested a set of nine WRF simulations (detailed in Table

3.4) over the CONUS for summer 2012 (June–August), with the last week of May being the spin-up period. The SVF varies from 0.15 to 0.85 by changing urban or tree morphologies. WRF diagnostics of 2-m air temperature (T_2), net radiation (R_n), ground heat (G) and sensible heat (H) were used to quantify the model uncertainties. The results are shown in Fig. 3.5. All the diagnostics were averaged temporarily over 18:00–21:00 UTC (11:00–14:00 PST or 14:00–17:00 EST) for daytime, and 06:00–09:00 UTC (23:00–02:00 PST or 02:00–05:00 EST) for nighttime, respectively, accounting for the variety of time zones of all CONUS cities. UTC was used to eliminate the potential confusion of daylight saving schemes in local times. The same temporal averaging method applies for all WRF simulations in this study.

Table 3.4. Numerical setups of cases for model uncertainty evaluation

Cases	1	2	3	4	5	6	7	8	9
SVF=F_{GS}=F_{SG}	0.150	0.250	0.364	0.450	0.550	0.604	0.651	0.750	0.850
w (m)	12.00	12.00	12.00	12.00	12.00	12.00	12.00	12.00	21.50
h (m)	21.80	11.50	6.30	6.30	6.30	6.30	5.35	3.50	3.50
r (m)	9.00	9.00	9.00	9.00	9.00	9.00	9.00	9.00	9.00
r_t (m)	2.30	2.30	2.30	1.35	0.45	0	0	0	0

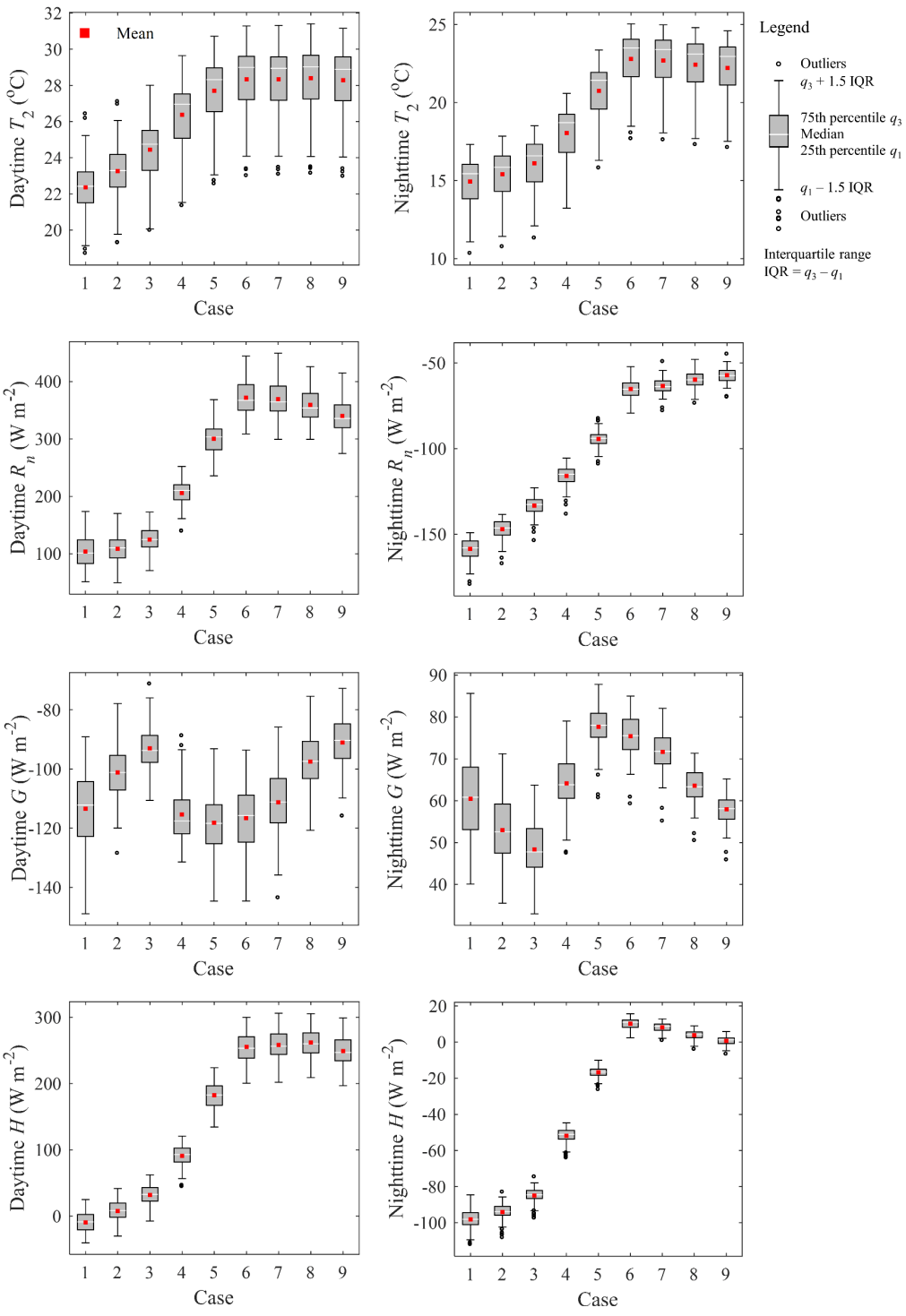

Figure 3.5. Sensitivity of urban hydroclimate and surface energy balance to different cases in Table 3.4: (left) daytime (averaged over 18:00–21:00 UTC) and (right) nighttime

(averaged over 06:00–09:00 UTC). T_2 is the near-surface (2-m) air temperature; R_n is the net radiation, positive downward; H is the sensible heat flux, positive upward; and G is the ground heat flux, positive upward.

From Fig. 3.5, it can be seen that the statistical mean diagnostics of T_2, R_n, and H increase with the SVF increasing from 0.15 to 0.60 (decrease in tree coverage or building density), but plateaued with further increase in SVF. The variation of G with SVF is rather nonlinear, with local extrema (downward maximum for daytime but upward maximum for nighttime) of mean G occurring at SVF of 0.5–0.6. This nonreality is attributable to the combined effect of radiative shading and trapping on the surface thermal state due to changes in urban and tree morphologies (Song and Wang 2015a).

3.3. Results and Discussion

3.3.1. Impact of Urban Trees on Regional Hydroclimate

The cooling effect of urban trees via shading is captured by the reductions of annual mean near-surface air temperature (WRF's 2-m diagnostic temperature, or T_2). The results are shown in Figs. 3.6 and 3.7 over the entire CONUS as well as in the selected six subregions for daytime and nighttime, respectively. The histograms of mean near-surface air temperature reductions and the associated (normalized) frequency (f) distribution functions are presented as well to show the variations of simulated results. The reductions of mean near-surface air temperature in urban areas are summarized in Table 3.5.

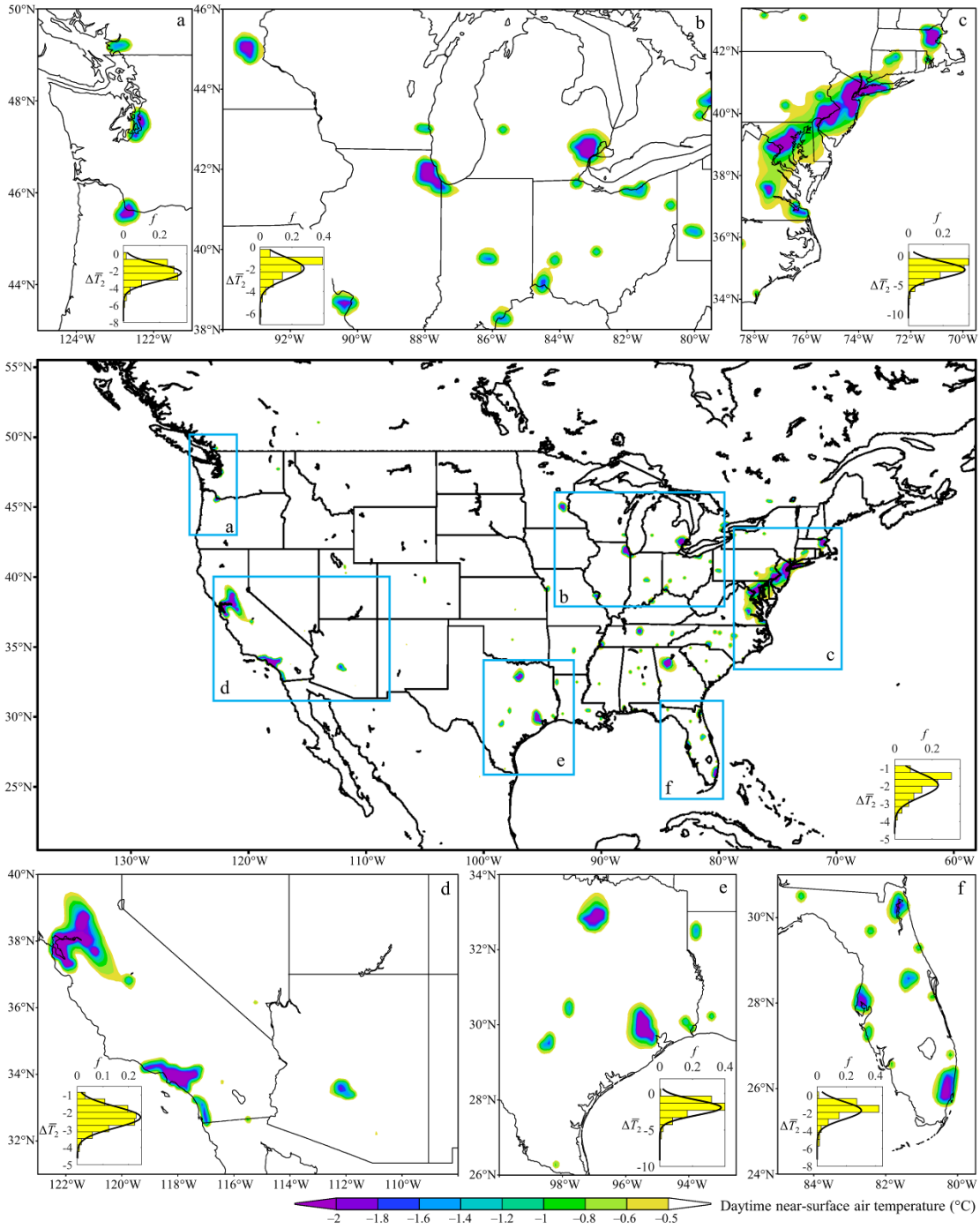

Figure 3.6. Impact of urban shade trees on mean daytime (averaged over 18:00–21:00 UTC) near-surface air temperature. Histograms denote (normalized) frequency (*f*) distribution of mean near-surface air temperature reduction ($\Delta\overline{T_2}$).

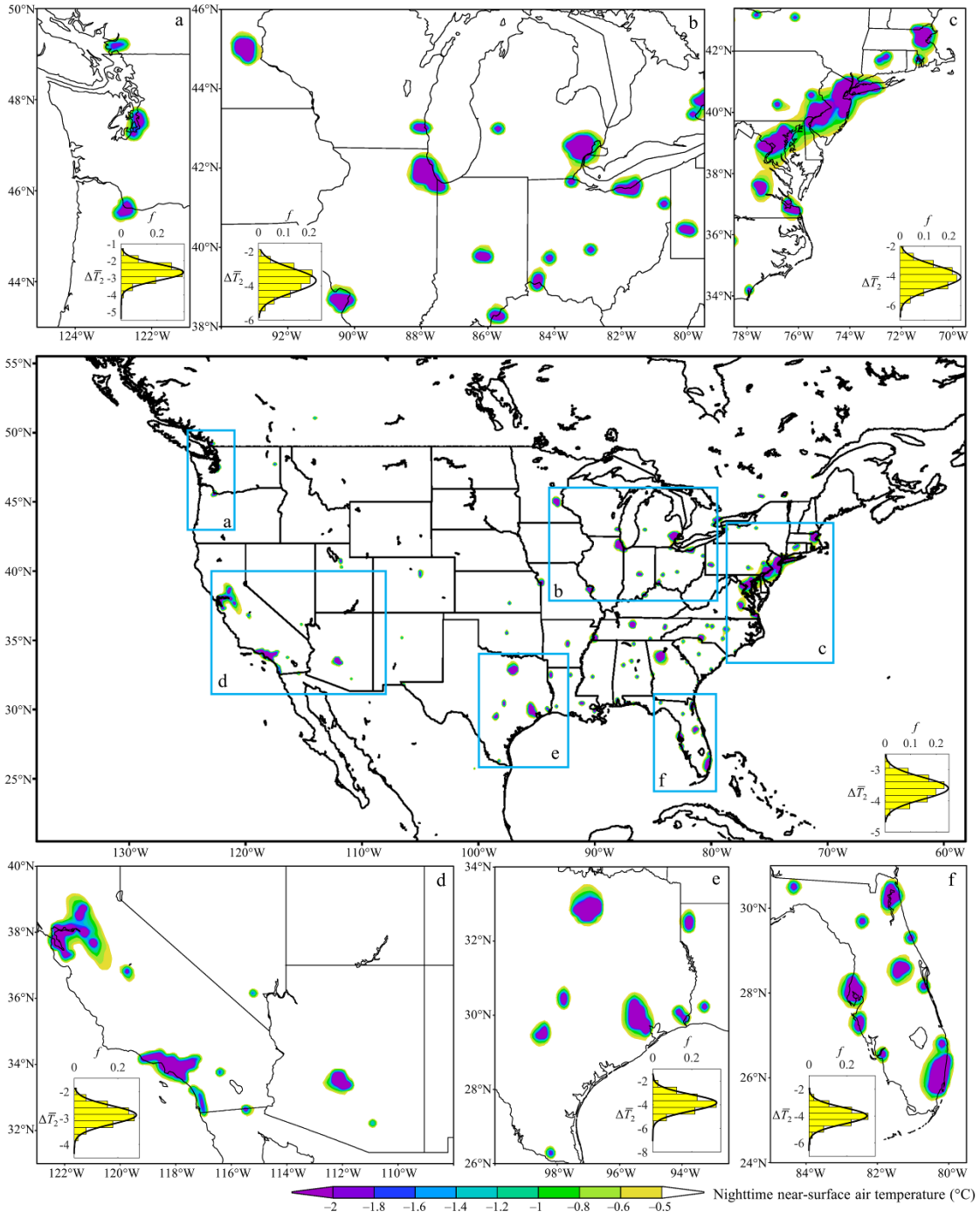

Figure 3.7. Impact of urban shade trees on mean nighttime (averaged over 06:00–09:00 UTC) near-surface air temperature. Histograms denote (normalized) frequency (*f*) distribution of mean near-surface air temperature reduction ($\Delta\overline{T_2}$).

Table 3.5. Mean near-surface air temperature (°C) averaged over the simulation period and its reductions due to the radiative shading by urban trees

Regions	Daily mean		Mean reduction	Daytime reduction	Nighttime reduction
	Control	Shaded			
CONUS	15.76	12.71	3.06	1.95	3.60
Cascadia	11.65	9.20	2.45	2.20	2.68
Great Lakes	9.45	6.35	3.10	1.93	3.69
Northeast	11.64	8.08	3.56	2.39	4.09
CA-AZ	18.76	16.11	2.66	2.27	2.88
Texas Triangle	20.47	17.29	3.18	1.95	3.84
Florida	23.04	19.73	3.31	1.70	3.99

The radiative shading effect of urban trees is significant on cooling the near-surface atmosphere, leading to a daily average reduction of 3.06 °C in near-surface air temperature in CONUS. The primary mechanism is that the presence of shade trees reduces the available energy impinged on canyon facets, modulating the near-surface air temperature through reduced sensible heat. The nighttime reduction of temperature is slightly stronger than that of daytime, owing to the enhanced radiative cooling over the entire built environment (detailed in Section 3.3.3); this is consistent with the finding of Upreti, Wang, and Yang (2017) at the regional scale.

Spatially, the reduction of mean near-surface air temperature, averaged over the entire simulation period of three years, varies in different subregions, attributable to different climatic and geographical conditions. Trees in more clustered (in terms of the

geographical distribution of urban pixels) and less fragmented built environment admit higher cooling degrees (Fan, Myint, and Zheng 2015). The cooling degrees in all six urban subregions are summarized in Table 3.5 as well. As shown in Fig. 3.6 and Table 3.5, denser urban clusters in the eastern portion of CONUS exhibit stronger cooling effects in the presence of trees when compared to the west continent. The cooling effect of urban trees is also regulated by the atmospheric stability via heat transport in urban canopy and boundary layers. The unstable atmosphere is conducive to vertical (turbulent mixing) and horizontal (breeze) advection (Hamada and Ohta 2010), leading to stronger cooling effects (e.g., subregion c in Fig. 3.6). In addition, the cooling intensity can be influenced by the available downwelling solar radiation as well. For example, the cooling effect is stronger in winter (December–February, 3.15 °C) than in summer (June–August, 2.95 °C), owing to the relatively more available solar radiation in winter during daytime (the prevalent clear sky weather). Interestingly, the reduction of mean near-surface air temperature over CONUS reaches its maximum in fall (September–November) on the order of ~3.36 °C, and minimum in spring (March–May) at ~2.78 °C. This temporal lag in extremities of the cooling effect is likely due to the flux–temperature hysteresis presented in the annual cycle, where temperature extremities are delayed as compared to those of heat fluxes (Z.-H. Wang 2014a).

The changes of mean daytime and nocturnal near-surface (2-m diagnostic) relative humidity are plotted in Fig. 3.8. Over the entire simulation period, the mean near-surface relative humidity increases by 13.62% with the presence of shade trees in CONUS.

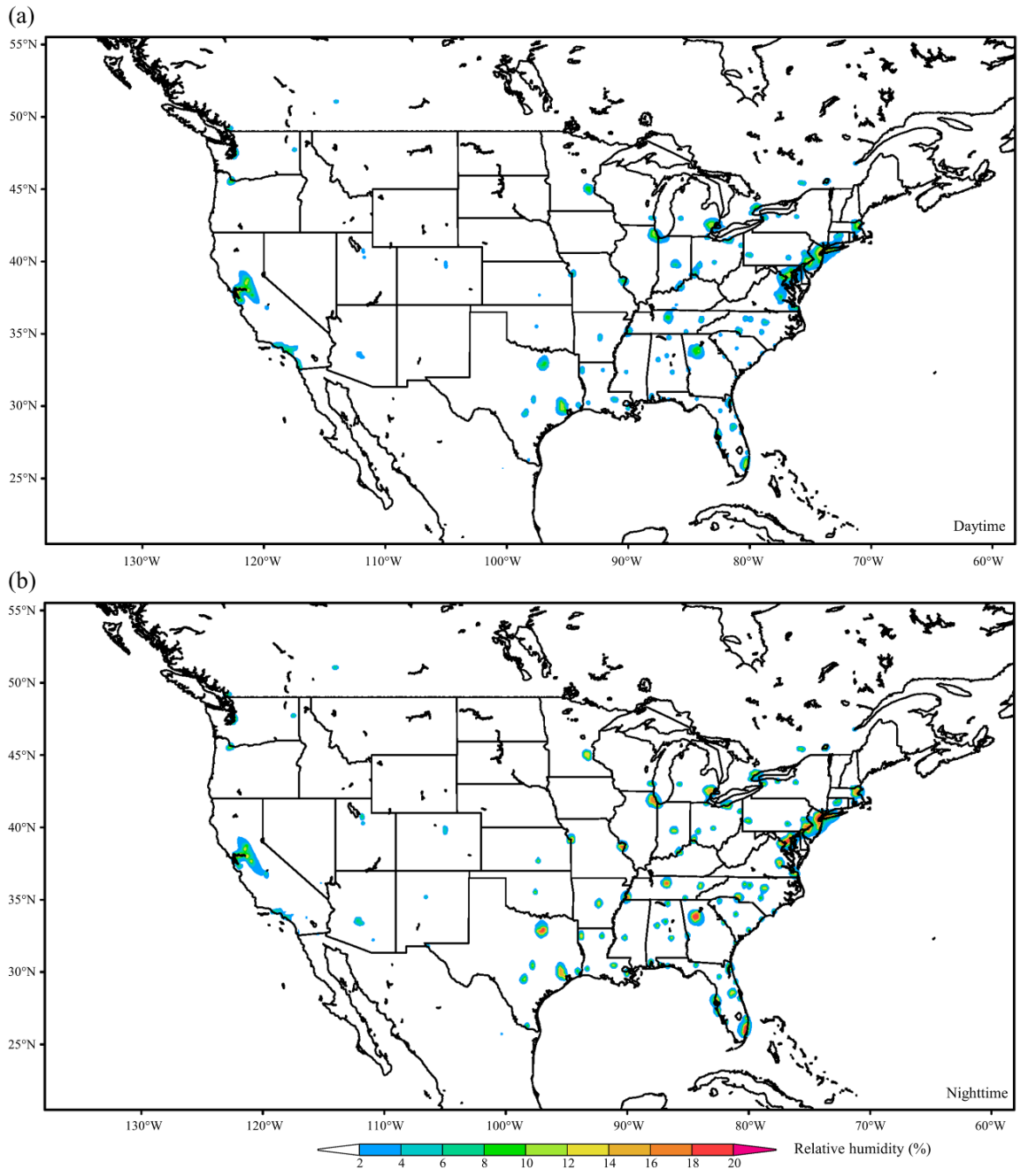

Figure 3.8. Impact of urban shade trees on mean near-surface relative humidity for (a) daytime (averaged over 18:00–21:00 UTC) and (b) nighttime (averaged over 06:00–09:00 UTC).

The increase in near-surface relative humidity is exclusively due to the decreased near-surface air temperature (Upreti, Wang, and Yang 2017), as ET from trees is inhibited in the current setting. Note that the relative humidity is the ratio of the vapor pressure to saturation vapor pressure. Temperature drops reduce saturation vapor pressure, resulting in relative humidity rises. Therefore, the spatial pattern of mean near-surface relative humidity changes is similar to that of mean near-surface air temperature changes (Figs. 3.6 and 3.7). Similarly, the increase of mean daytime near-surface relative humidity (10.84%) is relatively less than that at night (14.11%). The density of urban clusters plays an important role in affecting the intensity of mean near-surface relative humidity decreases as well, as suggested by the stronger reduction in the eastern portion of CONUS. However, climate patterns and contemporary humidity conditions might not significantly influence the mean reduction of near-surface relative humidity. For example, both maximum and minimum reductions are observed in humid subregions (with maximum of 14.95% in Florida, and minimum of 10.97% in Cascadia).

3.3.2. Impact of Urban Trees on Outdoor Thermal Comfort

The changes of mean *HI* and *WCI* were evaluated in summers and winters, respectively. The results are shown in Fig. 3.9. Note that the results here are conditioned upon the presence of trees with particular geometry (i.e., with circular crown of 1 m in radius) in a uniform street canyon with dimensions shown in Table 3.2. Statistics of changes (i.e., arithmetic averages $\overline{\Delta HI}$ and $\overline{\Delta WCI}$, and standard deviations $\sigma(\Delta HI)$ and $\sigma(\Delta WCI)$), are shown in Fig. 3.9 as well. Regions that are not suitable for evaluations with *HI* (mean air temperature < 26.7 °C) or *WCI* (mean air temperature > 4.4 °C) were

masked out. Among the selected six subregions, only four subregions are suitable for evaluating mean *HI* or *WCI* reductions.

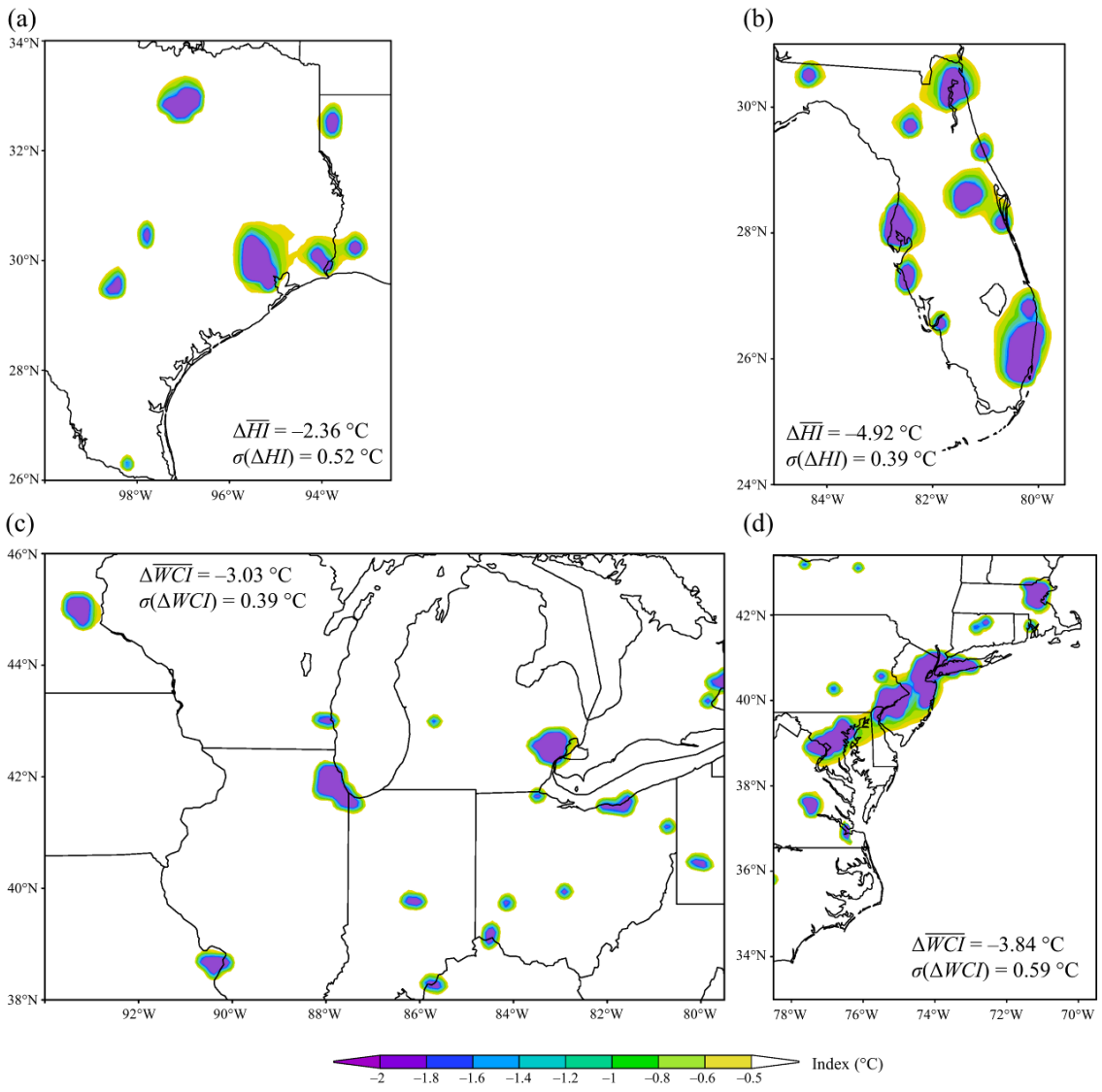

Figure 3.9. Impact of urban shade trees on summer heat index *HI* in (a) Texas Triangle and (b) Florida, and winter wind chill index *WCI* in (c) Great Lakes and (d) Northeast.

$\overline{\Delta HI}$ and $\overline{\Delta WCI}$ are mean *HI* and *WCI* reductions, while $\sigma(\Delta HI)$ and $\sigma(\Delta WCI)$ are standard deviations of *HI* and *WCI* reductions, respectively.

The reduction of *HI* in summers mainly results from the decreased air temperature. *HI* reductions are observed over several hot cities distributed in the Southwestern (Phoenix, Arizona) and Southern U.S. (major cities in West South Central and Florida, e.g., Houston, Texas, and Miami, Florida). The effect of local climatology and geography is noticeable. The improvement of thermal comfort level in relatively humid regions is amplified by the higher humidity (e.g., Florida; see Fig. 3.9b). A plausible reason is that mean *HI* is greater than that of mean near-surface air temperature. In contrast, the cooling effect of trees on the outdoor thermal comfort is impaired in relatively drier climatic zones. For example, mean summer *HI* in Texas Triangle only decreases by 2.36 °C, though the mean air temperature drops by 3.04 °C. It is noteworthy that here the *HI* values were averaged over summers. During extreme urban climate events such as mega heat waves, the effect of tree shading on the reduction in *HI* and the enhancement of pedestrian thermal comfort can be more significant. Based upon the methodology adopted in previous studies on mortality risk during heat waves in U.S. cities (Anderson and Bell 2011; Curriero et al. 2002), the heat-related mortality in Texas Triangle and Florida during a severe heat wave is estimated to be at least reduced by ~16.3% with shade trees deployment.

Winter *WCI* reduction is found mainly in the Northeastern and Midwestern U.S. (e.g., Chicago, Illinois, and New York City, New York; Fig. 3.9c and d). There are a number of cities with only ~1 °C mean *WCI* reduction scattering in the Western U.S.

(e.g., Salt Lake City, Utah, and Denver, Colorado). The *WCI* change is induced by decreased near-surface air temperature by shading and wind speed retarded by tree canopies. In addition, the magnitude of *WCI* is dominated by the values of ambient temperature. For instance, a minimum *WCI* of –9.24 °C is observed in the Great Lakes region, which is the coldest subregion during the winter.

The reduction of winter *WCI* can be detrimental, as the temperature-related mortality peaks in the winter due to relatively common epidemic respiratory infections (Curriero et al. 2002). It was suggested that the mortalities in Northeast and Chicago, Illinois increase by ~3.6% and ~2.3%, respectively, per 1 °F lower than the minimum winter mortality temperature (Curriero et al. 2002). Therefore, an increase of mortality due to the reduced *WCI* in Northeast is estimated to be ~24.0%. If further assuming the winter mortality in Chicago representative for the entire subregion b, the mortality rise is ~12.1% in Great Lakes. As far as the shading effect alone is considered, planting too many shade trees could induce more health problems during the winter, and thus is not recommended for cold regions like Northeast U.S.

3.3.3. Impact of Urban Trees on Surface Energy Balance

Trees regulate the land surface energy balance via a number of pathways, as discussed in Section 3.1.2. Considering a generic urban pixel represented using WRF-UCM, the anthropogenic and latent heat in Eq. (3.1) are not accounted here. The results of surface energy balance are shown in Fig. 3.10.

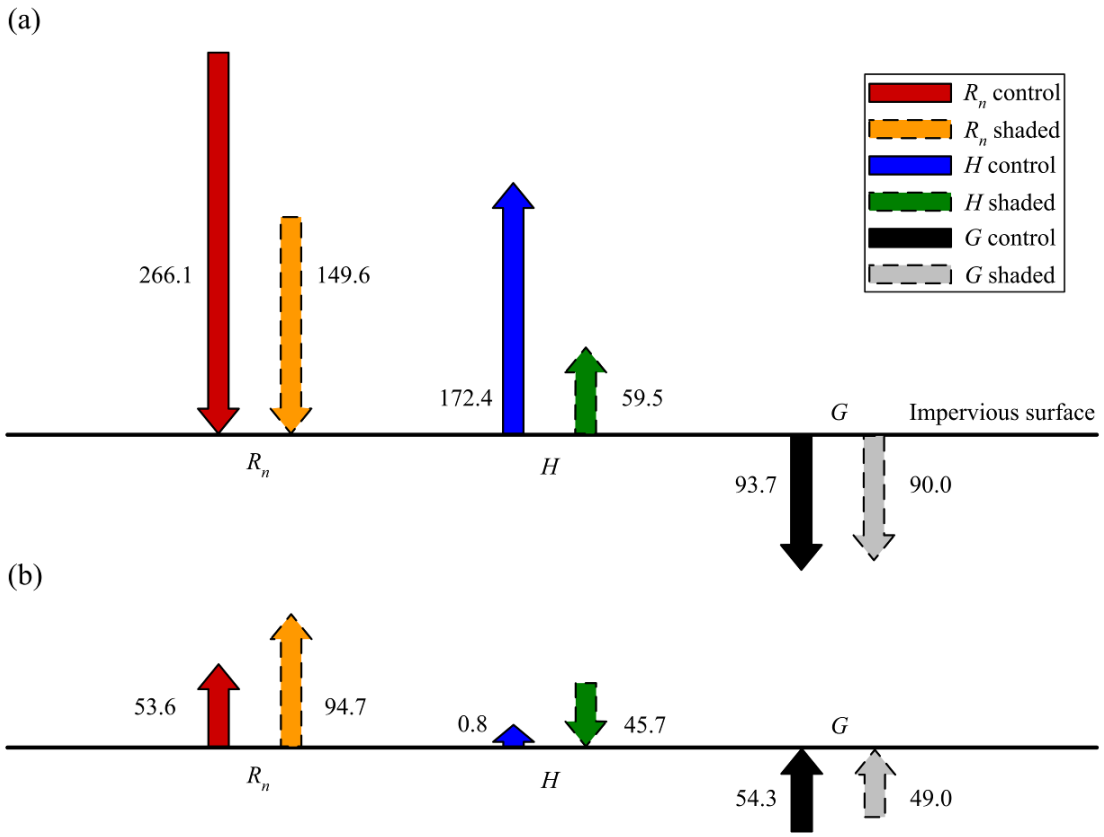

Figure 3.10. Impact of urban shade trees on the energy balance of impervious surfaces of CONUS, averaged over (a) daytime and (b) nighttime. R_n is the net radiation, positive downward; H is the sensible heat flux, positive upward; and G is the ground heat flux, positive upward. All values are shown as absolute values in W m^{-2}.

During daytime, the interception of solar (shortwave) radiation by tree foliage substantially decreases the amount of energy impinged on urban facets, leading to an average reduction of net radiation of 116.5 W m^{-2} (43.8%) over the CONUS. It is noteworthy that despite the drastic difference in incoming solar radiation among different subregions, this reduction of daytime radiation distributes quite uniformly over the CONUS (results of subregional analysis not shown here). Similarly, the presence of trees

significantly enhances the radiative cooling during nighttime, with an average increase in upwelling terrestrial radiation of 41.1 W m^{-2} (76.7%). In the urban canopy layer, the nocturnal cooling of the built environment is predominated by the radiative cooling in the vertical direction (Z.-H. Wang and Li 2017). When normalized by the amplitude of daytime and nighttime radiation respectively, the radiative cooling effect by urban trees is comparatively stronger during nighttime, leading to a higher degree of nocturnal cooling. This is consistent with the results reported in an extensive field measurement conducted recently, suggesting that more significant nighttime cooling can be induced by transpiration of urban trees (Konarska, Uddling, et al. 2016). The phenomenon here is also in line with the review by Bowler et al. (2010) on the cooling effect of urban vegetation in general.

In response to the presence of trees, the change in sensible heat is much more significant than that in ground heat. This is because the thermal inertia of the atmosphere (in transporting sensible heat) is much less as compared to that of engineering pavements (in conducting ground heat). The difference in thermal inertia amounts to roughly three orders of magnitude, rendering the atmosphere much more susceptible to change in energy balance via the adjustment of the near-surface temperature gradient. The patterns of change in sensible and ground heat fluxes are consistent during daytime and nighttime. It is apparent that the presence of urban shade trees, over the long run, tends to regulate the near-surface atmospheric temperature significantly, but leaves the subsurface thermal field and thermal storage nearly intact.

The effect of shade trees on regulating radiative and sensible heat fluxes has strong implications to energy efficiency, especially the cooling load during summers.

Indoor cooling inside built structures has strong correlations to the ambient temperature as well as to the net radiation, both sensitive to the presence of trees. On the other hand, the strong cooling potential of the outdoor environment by shade trees, together with the improved human thermal comfort, leads to prolonged period of outdoor activities and saving of cooling energy (e.g., personal, vehicular, and infrastructural) (Z.-H. Wang, Zhao, et al. 2016).

3.3.4 Relative Contribution to Cooling by Radiative Shading and ET

The net radiation absorbed by tree crowns mainly partitions into the advection of sensible heat, the latent heat of vaporizing liquid water via ET, and heat storage within the canopy (Oke et al. 1989; Shashua-Bar and Hoffman 2002). On the other hand, the ambient air is less heated by the cooler surface owing to the shading. Previous experiments measured temperature or radiation differences between the shaded areas and the adjacent sunlit areas, blending the effect of radiative shading and ET cooling (e.g., Hamada and Ohta 2010). In contrast, scale models and numerical studies largely focus on only one of them due to the extreme difficulty of mimicking real plants. For example, Spronken-Smith and Oke (1999) neglected the ET of trees, as scaling this process is too complex using foam rubber. Song and Wang (2015b) considered only the shading effect in their UCM simulations owing to the negligible ET from trees over xeric landscapes. A recent computational fluid dynamics analysis studied ET cooling solely but omitted shading from trees (Gromke et al. 2015).

Nevertheless, there is growing interest in splitting the two effects and quantifying them separately, even for *in situ* measurements. A measurement in Israel quantified the

shading of urban trees which contributes to ~80% of the cooling effect at 15:00 local time during summer via multilinear regression (Shashua-Bar and Hoffman 2000). In contrast, Georgi and Dimitriou (2010) concluded that trees improve microclimatic conditions mainly through ET by observing five different species. It is noteworthy that the contributions of shading and ET to the actual cooling effect of trees significantly vary under different conditions. Tree species have been recognized as one of the key factors (Georgi and Dimitriou 2010; Shahidan et al. 2010). Research suggested that the ET cooling effect differs also in different latitudes. For instance, two long-term observations showed that the ET cooling in Manchester, UK was several times stronger than that in Gothenburg, Sweden (Konarska, Uddling, et al. 2016; Rahman et al. 2011). Shashua-Bar and Hoffman (2002) suggested that the cooling effect of tree crowns on air temperature can be estimated either by subtracting the sensible heat from the absorbed net radiation, or by summing up the energy consumptions via ET and heat storage. They concluded that estimating the cooling of air temperature solely based on a single factor can lead to inaccurate results. Nevertheless, besides shading and ET, resolving the interactive thermodynamic and biophysical processes in the continuum of trees, ambient air, buildings, pavements, and soils remains an outstanding challenge to quantify the actual thermal impact of urban trees using numerical models.

3.4. Concluding Remarks

In this study, we incorporated urban trees into the WRF-urban modeling system by parameterizing their participation in radiative heat exchange via modified view factors. This multiscale modeling framework was then applied to simulate the effect of

shade trees on all urban areas over CONUS. A uniform geometry of trees was adopted in this study. The model uncertainties associated with the mismatch between this simplification and those of existing landscape patterns are imbedded in the variability of view factors and climatic responses that are quantified in Section 3.2. Model diagnostics were calculated to evaluate the impact of trees shading on urban hydroclimate, outdoor human thermal comfort, and land surface energy balance.

In general, urban trees are found to be effective in alleviating urban thermal stress via radiative shading, and the cooling effect is more prominent during nighttime. This cooling effect is beneficial to outdoor thermal comfort by reducing the summer heat index for cities located in tropical and subtropical climates. Over a long run, the presence of urban trees has opposite effect on the land surface energy balance: It reduces the shortwave radiation during daytime but enhances the terrestrial radiation during nighttime. As a response, this change of surface energy balance leads to significant reduction of long-term mean sensible heat toward the sky, while leaving the long-term ground heat storage comparatively intact.

We reiterate that the proposed WRF-urban modeling framework only incorporates the radiative heat exchange between trees and urban facets, leaving out other biophysical functions of trees such as ET in the current study. Much work is left to be done for more comprehensive and realistic representation of urban trees and their interactions with the built environment. Nevertheless, the findings of this study on the cooling effect of shade trees can be informative to researchers and policy makers. For instance, most of the current urban mitigation strategies focus, almost exclusively, on reducing the daily maximum temperature, but largely ignore the nighttime thermodynamics of cities. A

famous example is the widely advocated use of highly reflective (white) materials on roofs (aka cool roofs). White roofs cool the urban temperature above the canopy layer during daytime, but become unserviceable during nighttime in the absence of solar radiation. In planning for sustainable development of future cities, this one-sidedness needs to be avoided. Toward this end, the use of urban green infrastructure in general (trees included) emerges as an attractive option.

CHAPTER 4

ENVIRONMENTAL COOLING OF URBAN TREES UNDER THERMAL EXTREMES

In this chapter, we aim to quantify the cooling capacity of urban trees in major U.S. metropolitans in response to thermal extremes (heat waves and cold spells) based on remotely sensed data. In total 24 heat and cold waves are identified as the extreme climatic stressors for 11 metropolitan areas. We define two temperature regimes, i.e., the transpirative cooling regime and the pseudo cooling regime, to account for the dominant mechanisms of the explicit cooling effect during heat waves and cold spells, respectively. The term “pseudo cooling” is introduced to describe the synthetic cooling of urban environment during cold waves where physiological functions of urban trees are largely suppressed. Specifically, we adopt the hypothesis of maximum transpiration (J. Wang et al. 2007) to characterize the transpirative cooling using water vapor pressure inside the stomatal cavity (instead of the commonly used vapor pressure deficit between leaf surface and atmosphere) that is assumed to be saturated according to the Clausius–Clapeyron equation.

4.1. Methodology

4.1.1. Selection of Metropolitan Areas

Eleven metropolitan areas in the CONUS were selected in this study (Fig. 4.1). The six metropolitan areas selected for heat wave analysis are Atlanta, Dallas-Fort Worth-Arlington, Los Angeles-Riverside, Miami, New York Metropolitan, and Phoenix Metropolitan. The six metropolitan areas selected for cold wave analysis are Boston-

Providence, Chicago, Detroit Metropolitan, Minneapolis-St. Paul, New York Metropolitan, and Washington-Baltimore. The New York Metropolitan was studied for both heat and cold waves, as it is the largest U.S. metropolitan in terms of area extent and population count. The selected metropolitan areas are among the most populous U.S. metropolitan areas based on U.S. census data. The boundaries of the selected metropolitans are based on the Topologically Integrated Geographic Encoding and Referencing (TIGER) product from the U.S. Census Bureau (https://www.census.gov/geo/maps-data/data/tiger.html). The urban areas were delineated using the 2010 U.S. census data in this product. We grouped the two connected metropolitans, e.g., Washington-Arlington-Alexandria and Baltimore-Columbia-Towson, into an integrated metropolitan area to yield a greater metropolitan. The detailed information of each metropolitan, including area, population, etc., is summarized in Table 4.1. Note that the urban population data in Table 4.1 are the annual estimates of the resident population as of July 01, 2016, which were retrieved from the U.S. Census Bureau.

We conducted a thorough review for documentation of urban trees in the selected metropolitan areas (see Appendix A). The city-scale species-based inventory is unavailable for most metropolitans, but there are inventories available for at least several districts in all metropolitans. The documented percentages of deciduous and evergreen trees, and the most common species within each metropolitan, based on available inventories, are summarized in Table 4.2. The information in Table 4.2 can be viewed as a snapshot to represent the ground truth of urban trees in the selected metropolitans. It is noteworthy that the vast majority of urban trees are deciduous in the six metropolitans

selected for cold wave study. In addition, the climate of each metropolitan area in Table 4.2 follows Köppen-Geiger climate classification based on observations during 1951–2000 with a spatial resolution of 0.5° (Kottek et al. 2006).

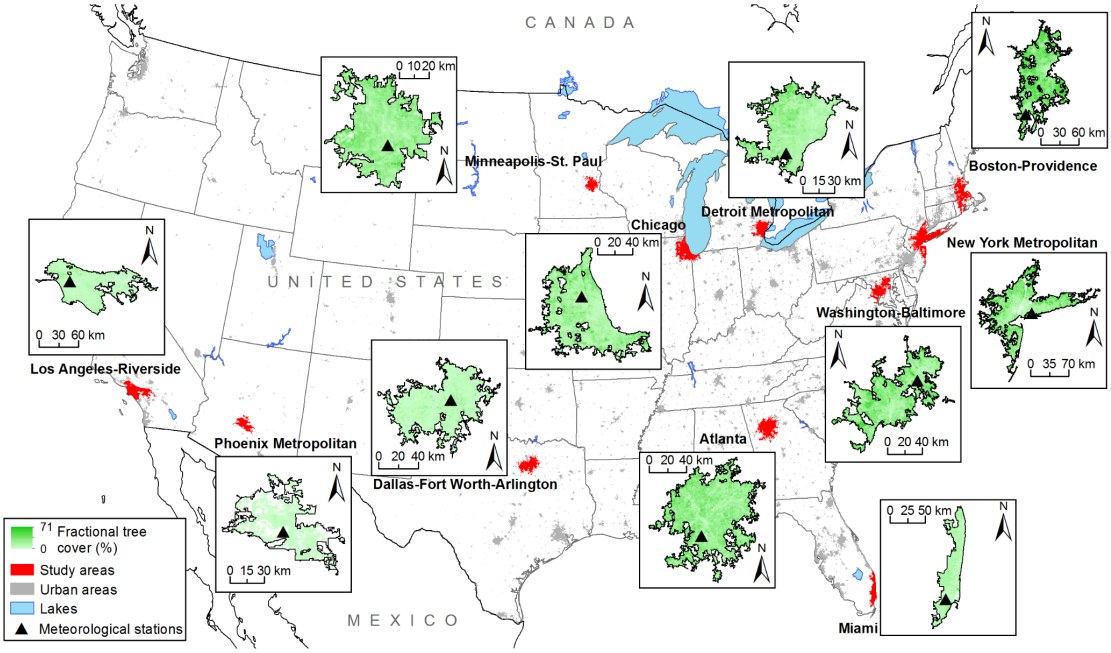

Figure 4.1. Locations of the selected metropolitan areas and meteorological stations in the CONUS, and variations of fractional tree cover in 2016.

Table 4.1. Information and statistics of the selected metropolitan areas

Metropolitan Area	State(s)	Area (km^2)	Metropolitan Statistical Area (MSA)	MSA Population in 2016 (million)	Meteorological Station ID	Number of pixels
Atlanta	GA	6944.94	Atlanta-Sandy Springs-Roswell	5.79	USW00013874	6932
Boston-Providence	NH, MA, RI	6551.10	Boston-Cambridge-Newton, Providence-Warwick	6.41	USW00014765	6572
Chicago	IL, IN	6432.34	Chicago-Naperville-Elgin	9.51	USW00094846	6441
Dallas-Fort Worth-Arlington	TX	4702.03	Dallas-Fort Worth-Arlington	7.23	USW00013960	4693
Detroit Metropolitan	MI	3981.94	Detroit-Warren-Dearborn, Ann Arbor	4.66	USW00094847	3986
Los Angeles-Riverside	CA	5977.43	Los Angeles-Long Beach-Anaheim, Riverside-San Bernardino-Ontario	17.84	USW00093134	5989
Miami	FL	3399.96	Miami-Fort Lauderdale-West Palm Beach	6.07	USW00012839	3402
Minneapolis-St. Paul	MN, WI	2878.58	Minneapolis-St. Paul-Bloomington	3.55	USW00014922	2861
New York Metropolitan	NY, NJ, CT	9469.16	New York-Newark-Jersey City	20.15	USW00094789	9493
Phoenix Metropolitan	AZ	3209.34	Phoenix-Mesa-Scottsdale	4.66	USW00023183	3194
Washington-Baltimore	DC, VA, MD	5416.04	Washington-Arlington-Alexandria, Baltimore-Columbia-Towson	8.93	USW00093721	5425

Table 4.2. Statistics of urban trees in the selected metropolitan areas

Metropolitan Area	Mean FTC in 2016 (%)	Climate	Deciduous (%)	Evergreen (%)	Other species (%)	Most common species and percent population
Atlanta	24.16	*Cfa*	94.7	5.3	–	Common crapemyrtle (*Lagerstroemia indica*), 17%
Boston-Providence	35.91	*Cfa*, *Dfa*, *Dfb*	49.4	3.0	47.6	Norway maple (*Acer platanoides*), 18%
Chicago	16.84	*Dfa*	~93.6	~6.4	–	European buckthorn (*Rhamnus cathartica*), 28%
Dallas-Fort Worth-Arlington	5.40	*Cfa*	75.5	24.5	–	Southern live oak (*Quercus virginiana*), 20%
Detroit Metropolitan	18.36	*Dfa*, *Dfb*	57.0	0	43.0	Norway maple (*Acer platanoides*), 18%
Los Angeles-Riverside	5.15	*Csa*, *Csb*	–	–	–	Mediterranean cypress (*Cupressus sempervirens*), 8%
Miami	10.19	*Af*, *Am*	0	69.0	31.0	Black olive (*Bucida buceras*), 31%
Minneapolis-St. Paul	21.21	*Dfa*, *Dfb*	99.7	0.3	–	Green ash (*Fraxinus pennsylvanica*), 14%
New York Metropolitan	27.01	*Cfa*, *Dfa*	99.1	0.9	–	London planetree (*Platanus acerifolia*), 15%
Phoenix Metropolitan	0.97	*BWh*, *BSh*	–	–	–	Velvet mesquite (*Prosopis velutina*), 8%
Washington-Baltimore	25.93	*Cfa*	~100	~0	–	Red maple (*Acer rubrum*), 19%

Note: FTC is the fractional tree cover based on satellite data (see Section 4.1.4 for details). Other species include unspecified species except the most common species in the inventory.

4.1.2. Land-Based Meteorological Observations and Selection of Heat and Cold Waves

To identify historical extreme temperature events, the daily average temperature (if available), maximum temperature, minimum temperature, precipitation, snowfall, and snow depth data from 2010 to 2017 were retrieved from the Global Historical Climatology Network (https://www.ncdc.noaa.gov/cdo-web/). One meteorological station was selected for each metropolitan area (see Table 4.1), and for most metropolitans we selected stations at the largest international airports mainly for two reasons. First, international airports in the U.S. usually have stable and the longest historical climate records. Second, measurements with a large open space are relatively undisturbed. The meteorological data at the selected airport stations were compared with other stations located in smaller airport within the same metropolitan area, showing only marginal discrepancies. The 30-year (1981–2010) long-term averages of daily temperatures were retrieved from Station Normals dataset provided by National Centers for Environmental Information, National Oceanic and Atmospheric Administration (https://www.ncdc.noaa.gov/cdo-web/search?datasetid=NORMAL_DLY).

Heat and cold waves are extreme temperature events that exceed a specified temperature threshold, and last for a minimum number of days (Peterson et al. 2013). We identified heat waves and cold waves as the periods of several days in June–Early September and Late November–February that have at least three consecutive days with daily minimum air temperatures greater and lower than the 30-year monthly averages of daily minimum temperatures, respectively. In addition, a complete heat/cold wave should include recognizable temperature rises/drops and temperature drops/rises in the pre-event and post-event periods, respectively. Cold waves with snow cover on some days (snow

depth > 0 mm) were filtered in this study, as the snow cover changes the albedo and thermal properties of the land surface (Jackson et al. 2008; M. Jin, Dickinson, and Zhang 2005; L. Zhou et al. 2003), and inconsistently alters the surface cooling mechanism. Furthermore, we selected extreme temperature events with only minimal, or no precipitation (rainfall, snow fall, etc.), to minimize the impacts of cloud cover and precipitation. For the selected heat waves, the durations were 9–21 days, and the ranges of rises in daily minimum and maximum temperatures were 2.2–9.5 °C and 6.2–16.7 °C, respectively. For the selected cold waves, the durations were 7–13 days, and the ranges of drops in daily minimum and maximum temperatures were 9.9–19.3 °C and 11.1–23.3 °C, respectively.

4.1.3. Surface Cooling Rate and Saturation Vapor Pressure under Environmental Temperatures

To quantify the cooling capacity of urban trees, we define a generic cooling rate (CR) as the change of temperature (T) per fractional tree cover (FTC), as

$$\mathrm{CR} = -\,dT / d\mathrm{FTC}, \tag{4.1}$$

where the negative sign denotes the opposite trend of changes in the two variables, i.e., temperature decreases as fractional tree coverage increases. For remotely sensed land surface temperature (LST), we can define the surface cooling rate (SCR) as

$$\mathrm{SCR} = -\,d\mathrm{LST} / d\mathrm{FTC}, \tag{4.2}$$

which can be readily derived from the slope of the simple linear regression between FTC and LST, for all pixels at each satellite overpass. The FTC in this study is based on a static yearly product without seasonal variability (see Section 4.1.4). Note that all simple

linear regression models and second order polynomial regression models, as a special case of multiple linear regression, are based on least squares methods in this study. The Pearson product-moment correlation coefficient *r* (Pearson's *r*) is used to describe the simple linear relationship between the variables, and *p*-value is from the two-tailed test of significance for regression coefficients (slope for simple linear regression).

To relate the surface cooling rate to saturation vapor pressure changes with temperature (see Section 4.2.1), we need to depict the nonlinearity of saturation vapor pressure–temperature relationship. The Clausius–Clapeyron equation for the phase change between water vapor and liquid water can be approximated as

$$\frac{de_s}{dT} = \frac{L_v e_s}{R_v T^2}, \tag{4.3}$$

where e_s is the saturation vapor pressure of water, L_v is the latent heat of vaporization for water, and R_v is the gas constant of water vapor. The nonlinear e_s–T relationship is described using an improved Magnus-form approximation (Alduchov and Eskridge 1996), given as

$$e_s = 6.1094 \exp\left(\frac{17.625T}{243.04+T}\right), \tag{4.4}$$

with e_s in hPa, T in °C, and the applicable temperature range is from –40 to 50 °C. Although the highest average LST (~63 °C) is out of this range, the relative error induced by using Eq. (4.4) is still minimal (~0.5%).

4.1.4. Satellite-Based Land Surface Characteristics

The LST data were retrieved from the Collection-6 (C6) MODIS instruments on

board the Terra and Aqua satellites (Wan, Hook, and Hulley 2015a; 2015b). Both satellites have sun-synchronous, near-polar circular orbits. Terra passes over the equator at around 10:30 and 22:30 local time, while Aqua passes over the equator at around 13:30 and 1:30 local time. The twin satellites jointly provide four LST retrievals in each 24-hour period for the same area (products MOD11A1 and MYD11A1), which adequately capture the daily extreme temperatures. The spatial resolution of LST images is 1 km at nadir. The LST products used herein have a mean LST error generally below 2 K with quality control, better than Collection-4.1 and Collection-5 products (Wan 2014). In addition, the MODIS LST product has been validated against *in situ* measurement, and the discrepancy was within ±1 K in the range of 263–322 K with different values of atmospheric column water (Wan et al. 2002). During each selected extreme temperature event, LST images that have > 80% pixels with low quality or no data (due to cloud coverage or other reasons) were discarded from the analysis.

The FTC data were retrieved from the yearly C6 MODIS Vegetation Continuous Fields (VCF) product (MOD44B) (DiMiceli et al. 2015). This product was derived using a regression tree algorithm (Hansen et al. 2002), and trained with Landsat data. The FTC data have a spatial resolution of 250 m and were degraded to 1 km resolution to match the LST product. This static yearly FTC product from the 65th day of the current year to the 64th day of the next year was used, showing the tree coverage all year round (DiMiceli et al. 2015). The FTC patterns in all selected metropolitans based on MOD44B 2016 data suggest the variations between different cities (Fig. 4.1 and Table 4.2). Examples of FTC and LST in the daytime and at night in 11 metropolitans during heat waves and cold spells are shown in Figs. 4.2 and 4.3. The information of the selected

examples (satellite images) is summarized in Table 4.3. Note that for each extreme temperature event, the corresponding yearly FTC product was used to derive the values of surface cooling rate.

Table 4.3. Information of the example satellite images shown in Figs. 4.2 and 4.3

Metropolitan area	Image collection data/range		
	Fractional tree cover	Daytime LST	Nighttime LST
Heat waves			
Atlanta	Mar. 2010–Mar. 2011	Sep. 06, 2010 (Aqua)	Sep. 07, 2010 (Terra)
Dallas-Fort Worth-Arlington	Mar. 2014–Mar. 2015	Aug. 12, 2014 (Terra)	Aug. 08, 2014 (Aqua)
Los Angeles-Riverside	Mar. 2016–Mar. 2017	Jun. 19, 2016 (Aqua)	Jun. 20, 2016 (Aqua)
Miami	Mar. 2013–Mar. 2014	Jul. 22, 2013 (Aqua)	Jul. 23, 2013 (Aqua)
New York Metropolitan	Mar. 2010–Mar. 2011	Jul. 05, 2010 (Aqua)	Jul. 04, 2010 (Terra)
Phoenix Metropolitan	Mar. 2013–Mar. 2014	Aug. 09, 2013 (Aqua)	Aug. 09, 2013 (Aqua)
Cold waves			
Boston-Providence	Mar. 2014–Mar. 2015	Dec. 26, 2014 (Terra)	Dec. 29, 2014 (Terra)
Chicago	Mar. 2016–Mar. 2017	Jan. 04, 2017 (Terra)	Jan. 04, 2017 (Aqua)
Detroit Metropolitan	Mar. 2009–Mar. 2010	Jan. 27, 2010 (Terra)	Jan. 28, 2010 (Aqua)
Minneapolis-St. Paul	Mar. 2015–Mar. 2016	Nov. 24, 2015 (Aqua)	Nov. 20, 2015 (Terra)
New York Metropolitan	Mar. 2011–Mar. 2012	Jan. 01, 2012 (Terra)	Jan. 07, 2012 (Aqua)
Washington-Baltimore	Mar. 2015–Mar. 2016	Jan. 02, 2016 (Aqua)	Jan. 03, 2016 (Terra)

Note: The satellite sources are shown in parentheses.

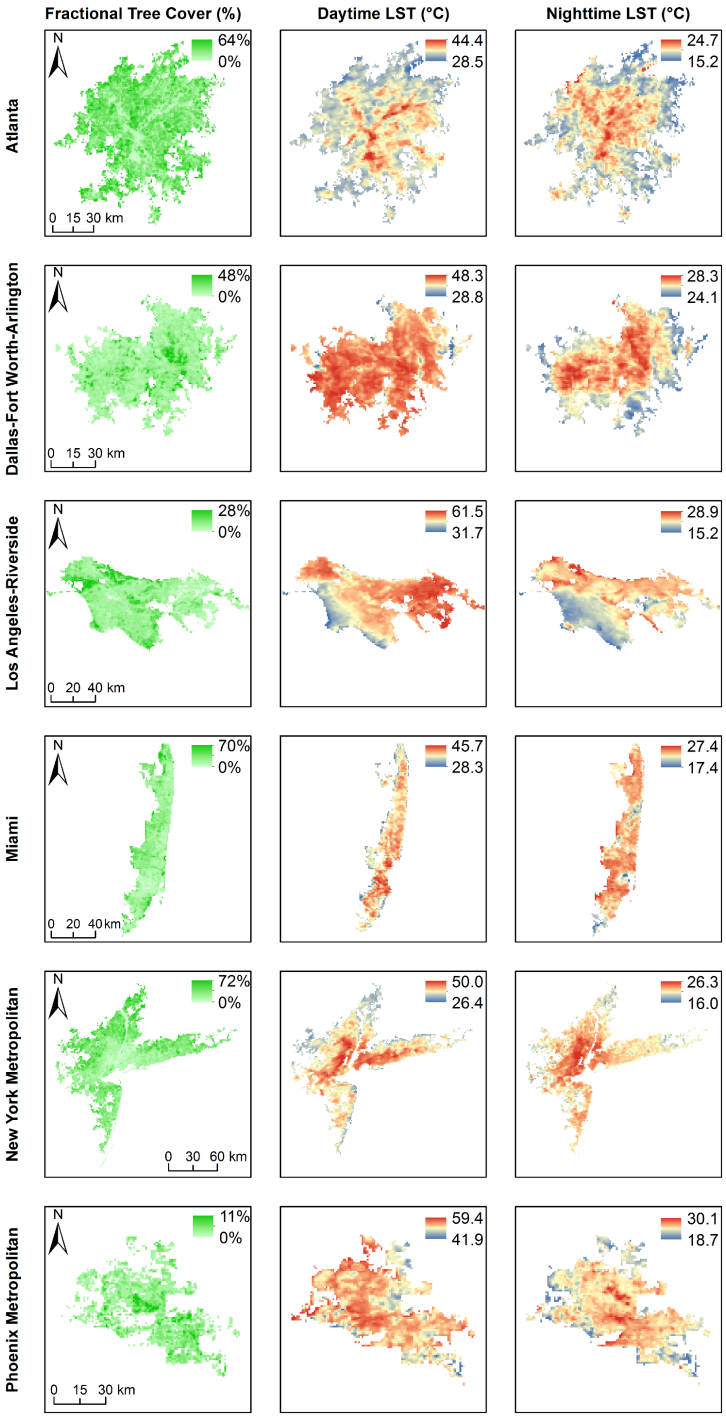

Figure 4.2. Examples of fractional tree cover and land surface temperature during daytime and night in heat waves. The information of the sample satellite images is summarized in Table 4.3.

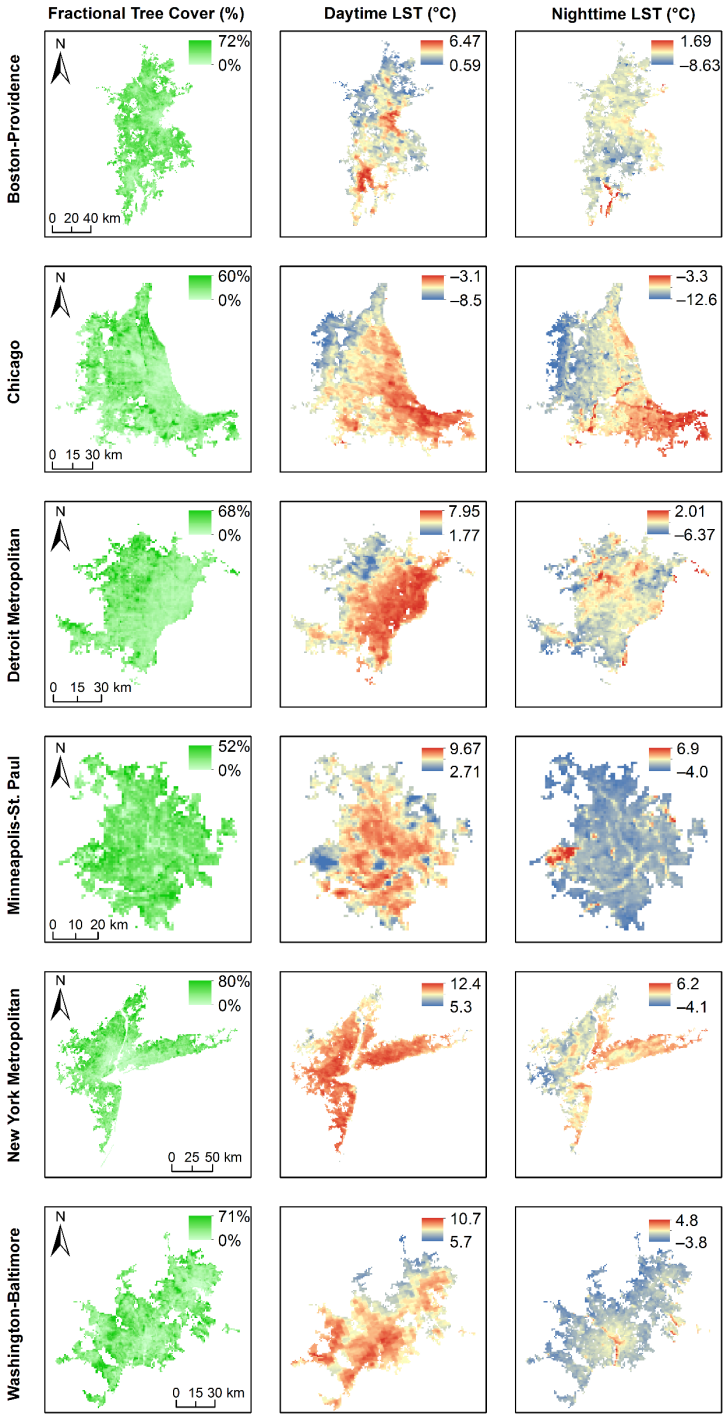

Figure 4.3. Examples of fractional tree cover and land surface temperature during daytime and night in cold waves. The information of the sample satellite images is summarized in Table 4.3.

We also retrieved an additional FTC dataset, Global Forest Cover Change (GFCC) product, from the Land Processes Distributed Active Archive Center (LP DAAC) archives (J. Townshend 2016) to verify the robust pattern of the derived surface cooling rate. This product was developed based on Landsat data (J. R. Townshend et al. 2012). The latest update of this 30-m product in 2015 was selected, and was resampled to 1 km. We conducted a pretest for two cold waves in January 2016 over New York Metropolitan Areas using both MODIS FTC and GFCC FTC. Although the GFCC FTC has a relatively higher overall FTC than MODIS FTC, the results of surface cooling rate using both products are consistent, with r values > 0.95.

The impervious surface data were retrieved from the 2011 National Land Cover Database (NLCD) (Homer et al. 2015). This 30-m yearly product is the most recent 5-year cyclical update, which was developed using Landsat 5 Thematic Mapper (TM) images. Consistent with MODIS FTC and LST data, the NLCD scenes were resampled to 1 km resolution as well. Within each metropolitan boundary, we calculated the spatial averages of MODIS FTC and fractional developed impervious surface. Results of fractional developed impervious surface are shown in Fig. 4.4.

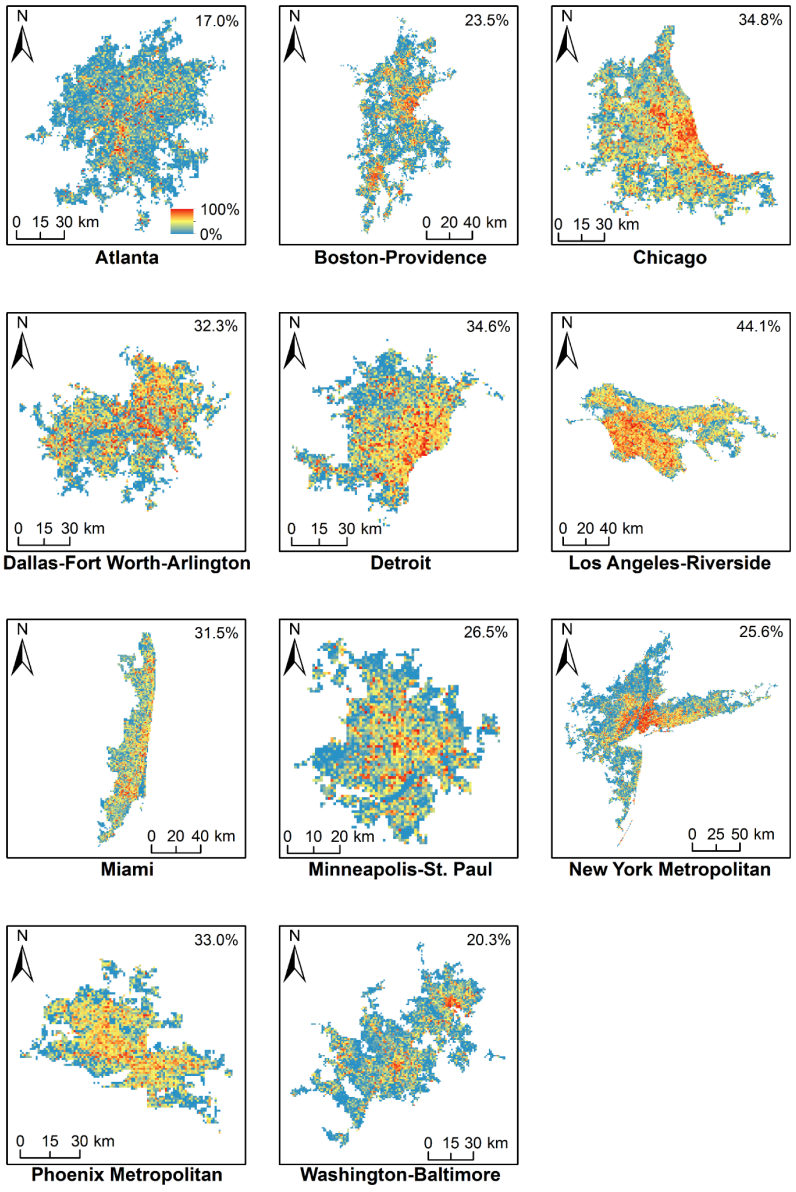

Figure 4.4. Variations of fractional impervious surface among cities. Fractional impervious surface data are from 2011 National Land Cover Database (NLCD). The spatial average of fractional developed impervious surface in each metropolitan area is shown at the upper-right corner of each subplot.

4.2. Results and Discussion

4.2.1. Temperature Dependency of the Surface Cooling Rate by Urban Trees

The cooling effect of urban trees depends on multiple factors, including their physiological and phenological characteristics, background urban settings, and climatic and geographical context (C. Wang, Wang, and Yang 2018). The response of each single tree to temperature, therefore, may show tremendous variabilities, necessitating aggregated evaluations at mesoscale (e.g., city and regional scales). The surface cooling rate defined in Eq. (4.2) indicates the cooling effect due to per percentage of tree cover change, and is therefore a useful measure for such evaluations based on MODIS-derived data. We evaluated the surface cooling rate of urban trees for each satellite image and related it to the average LST at each overpass for all images that meet the criteria described in Sections 4.1.2 and 4.1.4. Figure 4.5 shows the changes of surface cooling rate induced by urban trees in all analyzed extreme events, while the surface cooling rate–average LST relations in individual heat waves and cold spells are shown in Figs. 4.6 and 4.7. The shaded areas in Figs. 4.6 and 4.7 are 95% confidence intervals of slopes, and error bars denote 95% confidence intervals of the estimated surface cooling rates, both showing the uncertainties of the analysis. The statistics of the surface cooling rate–average LST relations are summarized in Table 4.4.

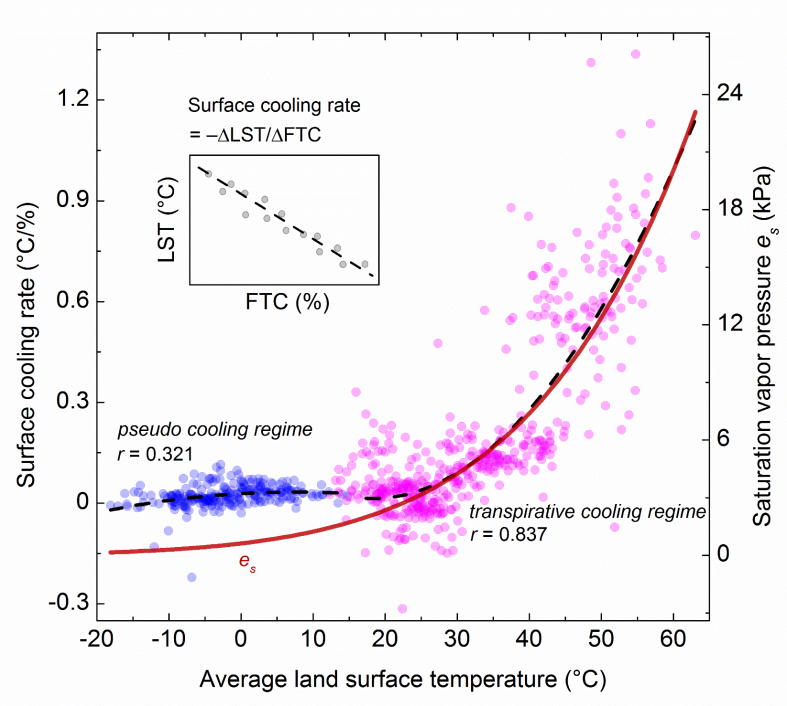

Figure 4.5. Dependence of surface cooling rate provided by urban trees on average urban land surface temperature (for each scene) in transpirative cooling regime and pseudo cooling regime, with inset the schematic diagram of determining the surface cooling rate. Magenta dots are data during heat waves. Blue dots are data during cold waves. Black dashed lines are second order polynomial regression fits to the data (i.e., $\hat{y} = b_0 + b_1x + b_2x^2$, where $\hat{y}$ is the predicted surface cooling rate, x is the averaged land surface temperature, and b_0, b_1, and b_2 are coefficients). For heat waves, p-value < 0.001 for both b_1 and b_2, and n = 486. For cold waves, p-value < 0.001 for b_1, p-value = 0.030 for b_2, and n = 249. The red solid line shows the saturation vapor pressure of water corresponding to average urban land surface temperature.

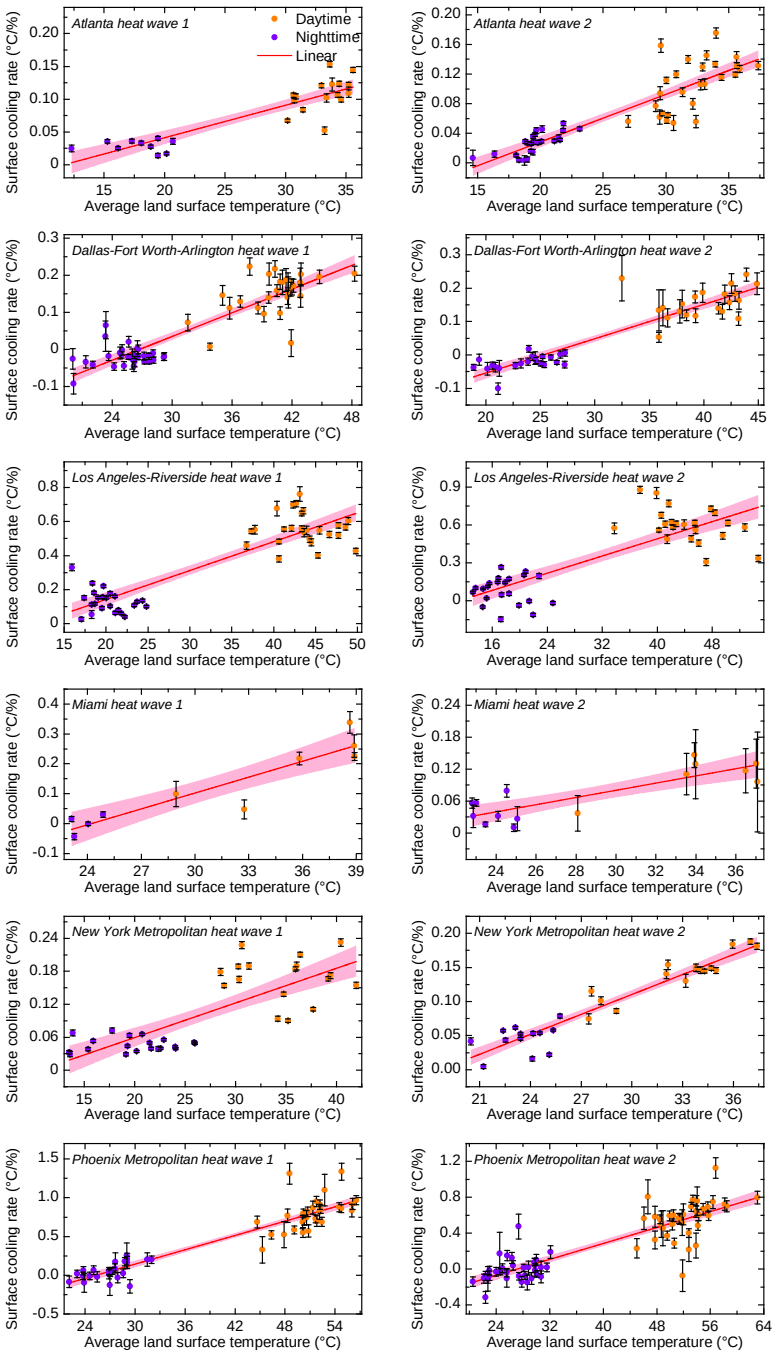

Figure 4.6. Relations between surface cooling rate of urban trees and average urban land surface temperature in heat waves. Shaded areas show 95% confidence intervals of slopes, while error bars show 95% confidence intervals of the estimated surface cooling rates.

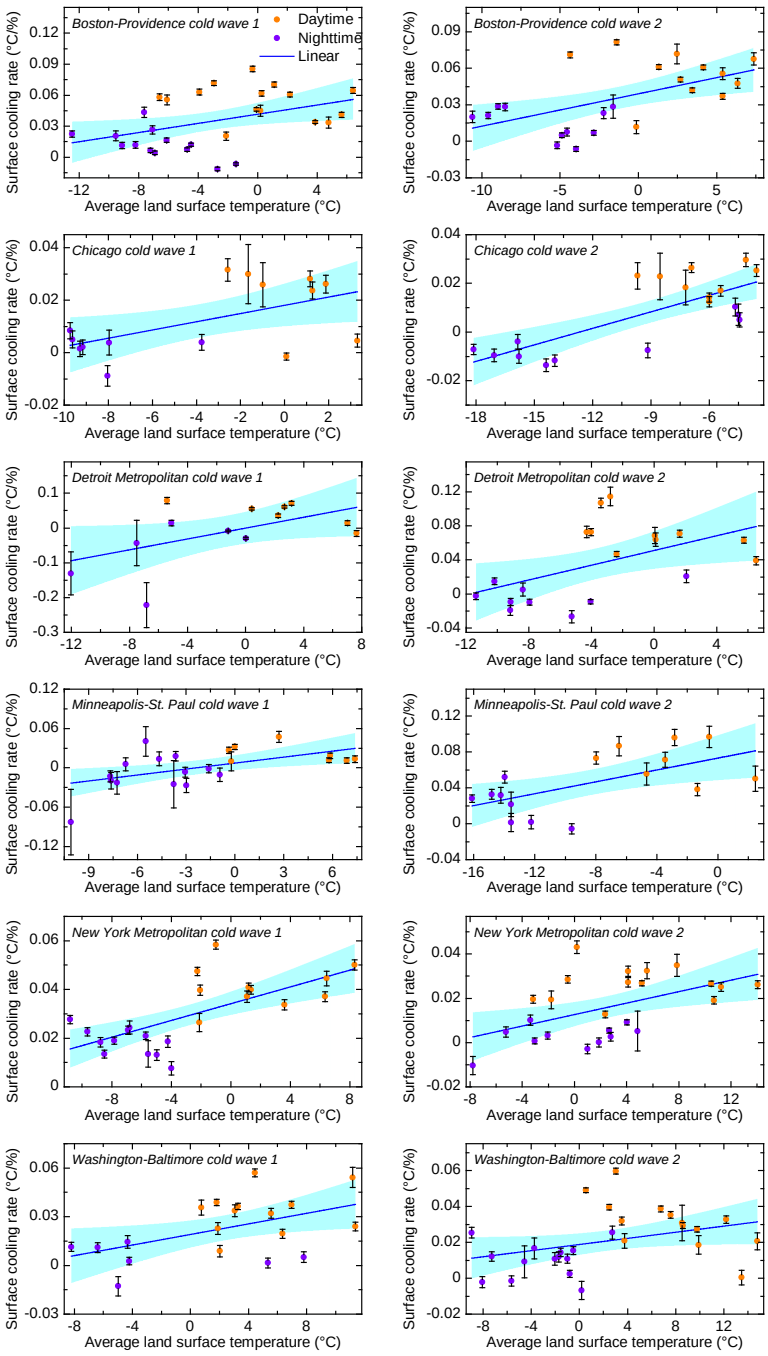

Figure 4.7. Relations between surface cooling rate of urban trees and average urban land surface temperature in cold waves. Shaded areas show 95% confidence intervals of slopes, while error bars show 95% confidence intervals of the estimated surface cooling rates.

Table 4.4. Relationship between surface cooling rate of trees and average urban land surface temperature among the selected metropolitan regions

Metropolitan Area and extreme temperature event	Pearson's *r*	*p*-value	*n*
Atlanta heat wave 1	0.893	< 0.001	26
Atlanta heat wave 2	0.893	< 0.001	51
Dallas-Fort Worth-Arlington heat wave 1	0.898	< 0.001	57
Dallas-Fort Worth-Arlington heat wave 2	0.923	< 0.001	43
Los Angeles-Riverside heat wave 1	0.894	< 0.001	50
Los Angeles-Riverside heat wave 2	0.824	< 0.001	45
Miami heat wave 1	0.927	< 0.001	10
Miami heat wave 2	0.844	< 0.001	15
New York Metropolitan heat wave 1	0.789	< 0.001	37
New York Metropolitan heat wave 2	0.954	< 0.001	29
Phoenix Metropolitan heat wave 1	0.932	< 0.001	53
Phoenix Metropolitan heat wave 2	0.874	< 0.001	70
Boston-Providence cold wave 1	0.420	0.026	28
Boston-Providence cold wave 2	0.550	0.007	23
Chicago cold wave 1	0.558	0.031	15
Chicago cold wave 2	0.763	< 0.001	19
Detroit Metropolitan cold wave 1	0.537	0.059	13
Detroit Metropolitan cold wave 2	0.519	0.023	19
Minneapolis-St. Paul cold wave 1	0.545	0.011	21
Minneapolis-St. Paul cold wave 2	0.602	0.014	16
New York Metropolitan cold wave 1	0.685	< 0.001	23
New York Metropolitan cold wave 2	0.506	0.010	25
Washington-Baltimore cold wave 1	0.501	0.029	19
Washington-Baltimore cold wave 2	0.355	0.064	28

Across 11 selected metropolitan areas in the CONUS, the surface cooling rate consistently increases with the spatial-averaged urban LST in extreme temperature events, as shown in Figs. 4.5–4.7 and Table 4.4. The correlation between cooling rate and urban LST in heat waves (r = 0.837) is much stronger than that in cold waves (r = 0.321), as the biophysical functions of trees, especially those deciduous, are largely suppressed in cold weather. Likewise, strong correlation is found for individual heat waves; r value ranges from 0.789 to 0.954 for heat waves, while from 0.355 to 0.763 for cold waves (Table 4.4). The surface cooling rate strongly intensifies at extremely high temperatures, whilst diminishes as temperature drops and asymptotically approaches zero at extremely low temperatures (Fig. 4.5). This strong dependence on temperature has been confirmed by a previous *in situ* measurement as well (Hamada and Ohta 2010). The year-long observation of the above study in Nagoya, Japan showed that vegetation (trees and grassland) cooling effect, when compared to the surrounding urban area, reached its maximum and minimum in July and March, respectively (Hamada and Ohta 2010). Toward the high temperature regime, the slope of the surface cooling rate (per LST change) increases rapidly, exhibiting a strong nonlinearity similar to the liquid–vapor phase equilibrium of water. Most remarkably, the temperature dependency of the cooling rate is in line with the variation of saturated vapor pressure, i.e., the thermodynamic liquid-water–vapor equilibrium governed by the Clausius–Clapeyron relation in Eq. (4.3) during heat waves (Fig. 4.5).

4.2.2. Surface Cooling Rate in Transpirative Cooling Regime during Heat Waves

Physically, the agreement in Fig. 4.5 can be interpreted in the light that the transpirative cooling is regulated by the liquid–vapor equilibrium, where water vapor passing through stomata of tree leaves is saturated or nearly saturated (Cernusak et al. 2018). During heat waves in summers, urban trees in general manifest stronger daytime cooling effect (Figs. 4.5 and 4.6), largely attributable to the amplified transpiration, as suggested by measurements at different scales (Crawford et al. 2012; Konarska, Uddling, et al. 2016; Urban et al. 2017). For example, Konarska, Uddling, et al. (2016) found that the transpiration rate of sunlit leaves was on average about three times higher than shaded ones in their experiments in Gothenburg, Sweden. With nearly saturated vapor supply through stomata, the rate of transpiration is regulated by the drying power of the atmosphere, which is a demand-controlled process. Per liquid–vapor equilibrium, the saturation vapor pressure within stomatal cavity of the well-watered urban trees increases with environmental temperature (Fig. 4.5). This leads to higher leaf–air vapor pressure gradient and stronger cooling at higher ambient temperatures (Kjelgren and Montague 1998).

Nevertheless, transpiration varies with species under extremely high temperatures (Ewers et al. 2005; Konarska, Uddling, et al. 2016). For tree species with low heat-adaptation capacity, extremely high temperatures reduce stomatal conductance and induce stomatal closure, attenuating the transpiration rate and thus the cooling rate (Hatfield and Prueger 2015; Kjelgren and Montague 1998; J. Zhao et al. 2013). As a result, the surface cooling rate slightly weakens with daytime temperature increase in Los Angeles-Riverside Metropolitan Area (see Fig. 4.6). At even higher temperatures,

however, areas dominated by heat-adapted plants still show strong daytime transpirative cooling effect, e.g., in Phoenix Metropolitan Area (see Fig. 4.6 and Table 4.2), as indicated by studies in Sonoran and Mojave Deserts (Hamerlynck et al. 2000; Smith 1978). A comparison between plant groups from hot environment with different humidity also showed that the plants from a drier environment have stronger transpiration capacity and cooling effect than those from a wetter one (Lin et al. 2017). In contrast, transpiration substantially diminishes at night, e.g., to only ~7–20% of its daytime counterpart as observed by Konarska, Uddling, et al. (2016). However, its contribution to nighttime cooling is synergistically amplified by the stable atmospheric stratification and attenuated anthropogenic heat emission (Holmer, Thorsson, and Lindén 2013; Oke 2006), resulting in lower but still noticeable cooling effect. The cooling effect of clustered tree canopies around urban cores (Figs. 4.2 and 4.4) is largely influenced by the surrounding hot environment. Such spatial distribution of urban trees weakens their cooling effect (Myint et al. 2015) and might even lead to nighttime warming; similar trend is observed here in Dallas-Fort Worth-Arlington and Phoenix Metropolitan Areas (Fig. 4.2).

4.2.3. Surface Cooling Rate in Pseudo Cooling Regime during Cold Waves

Except for areas with warm winters (e.g., Arizona, California, etc.), evergreen trees only constitute a small portion in urban canopy (Table 4.2), exerting weak transpirative cooling effect with lower solar radiation and vapor pressure deficit in wintertime (David et al. 2004). For deciduous trees, the canopy transpiration is nearly negligible in winters. This is also suggested by the discrepancy between saturation vapor

pressure and cooling rates at the low temperature regime (Fig. 4.5). Nevertheless, slight cooling effect still exists in almost all selected six metropolitans, as shown in Fig. 4.7.

In addition to the contribution of transpiration from evergreen species, the surface cooling rate of urban trees during cold waves is mainly due to the contrast to the elevated ambient temperature in urban areas; the latter is largely induced by waste heat released from human activities (Arnfield 2003; Sailor 2011; Sailor and Lu 2004). Anthropogenic heat emissions from extensive human activities including vehicular traffic, electricity consumption, industrial emission, heating fuels, and human metabolism result in higher LST in built-up areas (Figs. 4.3 and 4.4). The representative anthropogenic heating profiles for six large U.S. cities during both summer and winter seasons suggest a much stronger daytime heating than nighttime (Sailor and Lu 2004). As a result, the overall cooling effect of urban trees in winters is a "pseudo" one that is more prominent during daytime. For the same reason, the nighttime pseudo cooling rate of urban trees appears much milder. However, this pseudo cooling rate is impaired and even reversed (as warming) in areas with relatively low fractional tree cover, e.g., Detroit and Chicago (Table 4.2), as the contrast between temperatures of buildings and trees diminishes.

4.2.4. Temporal Variability of the Surface Cooling Rate and Contributions of Other Factors

The temporal variability (within the selected heat or cold waves for each metropolitan area) of the surface cooling rate induced by urban trees, and that of the LST during the studied heat/cold waves, are shown in Fig. 4.8. On average, urban trees show cooling effect during both heat and cold waves in most cities, while sporadic variability is

found such as the mild nighttime warming effect (Fig. 4.8). The temporal variability of average LST is lower in heat waves (standard deviation σ = 2.99 °C on average) than in cold waves (σ = 4.29 °C on average), suggesting that temperature changes in time during a cold wave are more intensive. Meanwhile, the temporal variability of surface cooling rate is higher in heat waves (σ = 0.07 °C/%, cf. 0.02 °C/% in cold waves), highlighting the sensitivity of tree cooling capacity to temperature in high temperature regime. Such dependence on LST becomes even more manifest when separately averaging the surface cooling rate over daytime and nighttime, as shown in Fig. 4.9 (cf. Fig. 4.5).

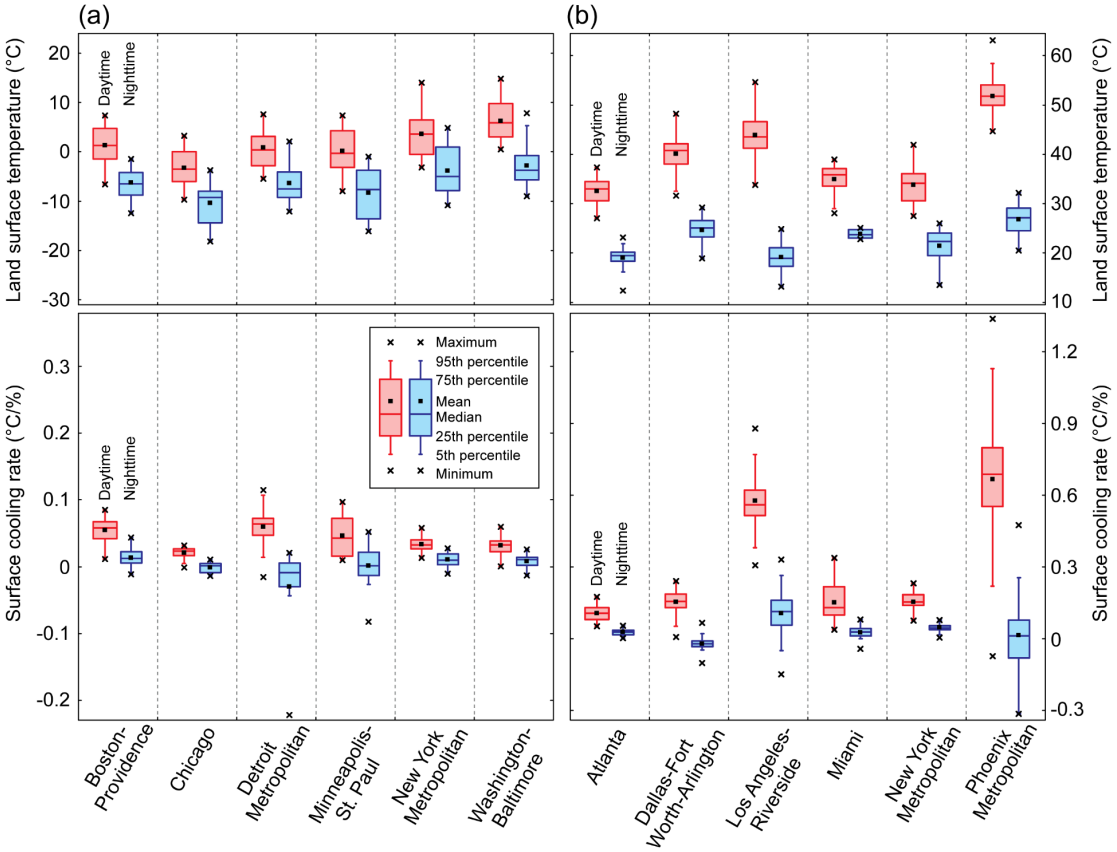

Figure 4.8. Variations of surface cooling rate of trees and corresponding land surface temperature among cities in (a) cold waves and (b) heat waves. The variations for each city are from the two cold or heat waves.

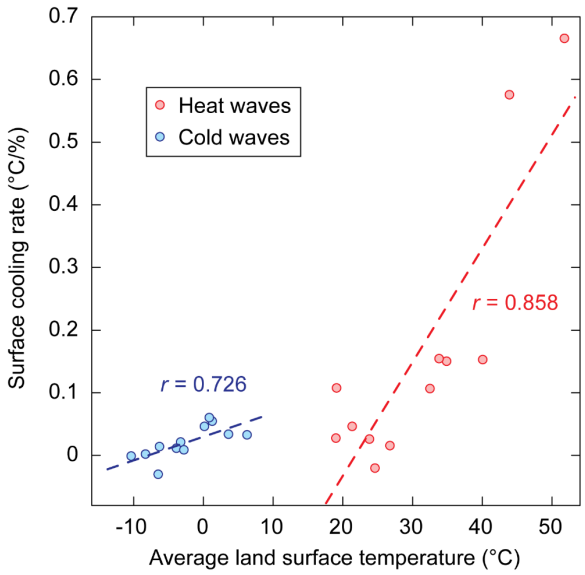

Figure 4.9. Dependence of average surface cooling rate on average urban land surface temperature. Dashed lines are simple linear regression fits to the data. For cold waves *p*-value = 0.007, and for heat waves *p*-value < 0.001. Note that $n = 12$ in all simple linear regressions, showing both daytime and nighttime averages over the two studied cold/heat waves for six cities.

It is noteworthy that on average the nighttime surface cooling rate during heat waves in Phoenix Metropolitan Area is close to zero, as shown in Figs. 4.6 and 4.8b, while previous studies have reported mixed results within the same area. For example, Myint et al. (2013) found statistically significant cooling effect of urban trees during a summer night over a part of the central phoenix (~178 km^2), with a spatial resolution of 90 m. The discrepancy is mainly induced by the difference in the fractional tree cover within the selected study areas, showing the spatial variation of the surface cooling rate.

In addition, the intra-city variability of surface cooling rate also results from regional climatic conditions. For example, Tayyebi and Jenerette (2016) divided the Los Angeles region (greater than the Los Angeles-Riverside metropolitan selected in this study) into 15 climate zones to quantify the cooling effect of urban vegetation. They observed an increasing trend of the cooling effect along the coastal–inland–desert gradient (Tayyebi and Jenerette 2016). As limited by the spatial resolution of the MODIS LST products, the underlying spatial structure of the surface cooling rate was not analyzed in this study. Nevertheless, by selecting metropolitan areas with different climates, the variation induced by climatic conditions can still be captured, as shown in Figs. 4.6–4.8.

While MODIS captures the temperature over the top of tree crowns, transpirative cooling is the primary biophysical function for urban trees in heat waves. Nevertheless, we recognize that other important factors can contribute to the surface cooling in the total built environment. The thermal properties of landscape materials and pavements can significantly impact urban surface temperature (Voogt and Oke 2003). Paved surfaces using highly reflective materials (viz., high albedo), for instance, are markedly cooler (Akbari, Pomerantz, and Taha 2001; Chudnovsky, Ben-Dor, and Saaroni 2004). Radiative cooling plays a strong role in regulating the thermal environment in cities as well (Manickathan et al. 2018; C. Wang, Wang, and Yang 2018). Furthermore, the anthropogenic heat emission also leads to temperature contrast during heat waves. The uncertainties induced by these local and microscale differences, however, cannot be well captured by the 1-km satellite images. To quantify and differentiate the contributions of these factors, we need to resort to a set of derivative data product (e.g., urban morphology, material properties, and near-surface atmospheric conditions) using fine-

resolution remotely imagery, such as thermal radiometer used in Chudnovsky, Ben-Dor, and Saaroni (2004).

4.2.5. Implications for the Use of Trees as an Urban Mitigation Strategy under Future Climate

The relatively consistent relationship between surface cooling rate and LST in extreme temperature events shows that urban trees present an attractive means for mitigating the exacerbated urban thermal stress (Arnfield 2003; Oke 2006; C. Wang, Wang, and Yang 2018). The cooling benefits during summertime can be amplified in cities suffering extensive anthropogenic heat emission. Increasing the percentage of heat-adapted trees is capable of further improving the cooling effect in cities, which is particularly desirable during extreme heat waves. On the other hand, the projected more frequent occurrence of climate extremes (Coumou and Rahmstorf 2012; Diffenbaugh et al. 2017), along with the continuous urbanization (Seto, Güneralp, and Hutyra 2012) in the following decades, will alter the growth rate of urban trees and their response to temperature. A comprehensive investigation based on data from 63 studies found that the enhanced growth in deciduous trees induced by urban warming during growing season is greater than that in evergreen trees, owing to the changes in their photosynthesis and respiration processes (Way and Oren 2010). Considering the prevalence of deciduous trees in the urban environment (as shown in Table 4.2), the enhanced tree growth induced by the elevated temperature (Way and Oren 2010) will likely promote the transpirative cooling effect during summertime later in the future, although the actual cooling capacity may vary with local climatic conditions in different cities. In addition, the trade-off

between cooling effect and water use for irrigation should also be carefully evaluated, especially for cities located in arid and semi-arid environment (Yang and Wang 2015; C. Wang, Wang, and Yang 2019).

In particular, urban forests are believed to be ahead of the global change responses, as they have been exposed to elevated temperature, carbon dioxide, nitrogen deposition, and ozone that will be experienced by their rural counterparts with a time lag of years to centuries (Calfapietra, Peñuelas, and Niinemets 2015; Gregg, Jones, and Dawson 2003; S. Zhao, Liu, and Zhou 2016). Urban environment therefore serves as a natural laboratory to study the long-term response of trees and their ecosystem services in large. The regulation of environmental temperature on surface cooling rate of urban trees also provides insights into evaluating the sustainability of trees as a long-term urban adaptation strategy.

4.3. Concluding Remarks

The effectiveness of urban trees as an urban mitigation and adaptation strategy has been documented by extensive studies (e.g., Bowler et al. 2010; Jenerette et al. 2016). Understanding how the cooling capacity of trees responses to extreme temperatures in different geographical context is important for sustainable urban development. Here we quantified the cooling capacity of urban trees, as the negative ratio of LST changes to FTC changes (i.e., surface cooling rate), in response to thermal extremes. During the studied 24 heat waves and cold spells, the surface cooling rate of urban trees exhibits strong nonlinearity and high dependency on environmental temperature across major metropolitans in the U.S. Especially, its temperature dependence is consistent with the

variation of saturation vapor pressure during heat waves, showing the dominance of plant transpiration in high temperature regime. In contrast, the pseudo cooling effect of urban trees during cold waves is mainly induced by the contrast to ambient anthropogenic heat emission, and therefore its change deviates from the Clausius–Clapeyron relation curve.

The present work captures the changes of urban tree cooling capacity during extreme temperature events based on MODIS LST products with high temporal resolution. It is noteworthy, however, the spatial pattern and magnitude of urban LST can be impacted by other factors such as fractional impervious surface (J. Peng et al. 2016; 2018). Evaluating the contribution of these factors necessarily requires the construction of more complex models such as multiple linear regression models and structural equation models (Tayyebi and Jenerette 2016). On the other hand, the spatial configuration of urban trees, the composition of species, the local climatic conditions, and even the resolution/window size used in the analysis can lead to variations in the surface cooling rate at spatial scales finer than urban scale (Tayyebi and Jenerette 2016; Z.-H. Wang, Fan, et al. 2016; W. Zhou, Wang, and Cadenasso 2017). These variations can be better quantified and evaluated using high-resolution remotely sensed data (a lot finer than 1 km resolution). In addition, the current study can be further improved with seasonal or monthly FTC product, as the yearly FTC product used herein does not capture seasonal foliage dynamics. The proposed method can be readily extrapolated to other metropolitan areas and small cities, and the classification of cities based on the similarity in surface cooling rate will be informative to systematic urban planning. Nevertheless, this study highlights the importance of using urban trees in combatting heat stress during hot seasons. The dependence of its cooling effect on temperature also

provides new insights into evaluating the sustainability of using trees to enhance environmental resistance and resilience for future urban environment.

CHAPTER 5

CONCLUSIONS AND PERSPECTIVES

5.1. Conclusions and Implications

This dissertation presents a comprehensive effort focused on the development, implementation, evaluation, and application of numerical models as well as the systematic evaluation using remote sensing products to quantify the impacts of urban trees on the quality of urban air and thermal environment. To evaluate the impact of urban trees on the traffic-emitted pollutant dispersion, we developed an integrative modeling framework by coupling LES and LSM. In the offline coupled framework, the dispersion trajectories of pollutants are simulated using LSM, while the Eulerian flow statistics and fields are pre-generated using LES. The dispersions of two-way traffic emissions were simulated using a set of 24 scenarios with varying street canyon and tree geometries. The proposed model was first used for simulations in a square canyon. The simulated results show reasonably well agreement with measurement data from water channel and wind tunnel experiments. The pollution level was then evaluated as the mean concentration of different zones in the street canyon. Results show that tall trees lead to the strongest modification of the canyon flow and pollutant concentration, except in narrow canyons. Trees can exacerbate canyon pollution level in certain built environment owing to the presence of isolated canyon vortices. Trees with high leaf area density are beneficial to reducing concentration in broad street canyons, while trapping of pollutants is manifest in narrow canyons. The participatory role of trees, in conjunction with the effect of urban morphology, is therefore crucial and needs to be meticulously evaluated in urban planning for promoting environmental quality.

To assess the impact of urban trees on the thermal environment, we used a coupled WRF-urban modeling system which incorporates the radiative shading of urban trees. The radiative shading effects were quantified as the differences between the control case (without trees) and the shaded case (with shade trees). Two sets of sensitivity tests were carried out to characterize the model uncertainties associated with the variability of existing landscape patterns. The model was then applied to examine the impact of urban trees on hydroclimate, pedestrian thermal comfort level, and urban land surface energy balance over the CONUS. Results show that on average the mean near-surface air temperature in urban areas decreases by 3.06 °C over the entire CONUS with the shading effect. Analysis of pedestrian thermal comfort shows that shade trees improve the thermal comfort level in summers, but could be detrimental in winters for cities located in temperate or subpolar climate zones. In addition, it was found that trees alter the surface energy balance by primarily enhancing the radiative cooling, leading to significant changes in the sensible heat but the ground heat comparatively intact.

Furthermore, we quantified the cooling capacity of urban tress in response to thermal extremes in major U.S. metropolitans. Based on extensive remotely sensed data, the cooling capacity was quantified as the negative ratio of the land surface temperature changes to fractional tree cover changes. The thermal extremes, i.e., heat waves and cold spells, were identified using the land-based meteorological observations from 2010 to 2017. Results show that the surface cooling rate is dominated by plant transpiration up to 1.336 °C/% in heat waves; its temperature dependence remarkably resembles the thermodynamic liquid-water–vapor equilibrium. Urban trees also exert pseudo cooling effect in cold waves in contrast to the anthropogenic heat emission. The average surface

cooling rate in cold waves is 0.022 °C/%, which is much smaller than that in heat waves (0.202 °C/%). The enhanced cooling capacity of urban trees will enable their provision of better ecosystem services to the urban environment for projected future increase of extreme heat.

5.2. Future Work

The coupled LES–LSM framework hitherto developed for pollutant dispersion over complex built terrains (Chapter 2) presents as a relatively economic and robust tool to resolve the turbulent transport of airborne pollutants. While the current results are under neutral condition, non-neutral conditions could change the pollutant dispersion and the ventilation effect of street canyons via buoyancy forces (Mei et al. 2016). Future model development will evaluate the proposed model under stable and unstable atmospheric stratifications. On the other hand, urban trees are numerically represented as ideal porous objects that are in thermal equilibrium with the surrounding air (expect their shading effect), and the complex leaf–air interactions (Leung et al. 2011; Salmond et al. 2016; Vos et al. 2013) are not included. Further development of this framework will focus on the inclusion of: (i) wet and dry deposition of pollutants, such as particulate matters, on leaves, (ii) emissions of VOCs and pollen from leaves, and (iii) heat exchange between trees and canyon air.

In addition, the integrated WRF-urban model developed for simulating shade trees in Chapter 3 suggests the cooling efficacy of trees in the large continental scale simulations. While a uniform geometry of trees was adopted in all 20-km simulations as limited by the relatively coarse resolution (20 km), high resolution (e.g., 5 km)

simulations (C. Wang, Wang, and Yang 2019) is desirable, in which various setups of tree geometries can be applied in different urban land use types. Further efforts toward improving the Monte Carlo ray tracing approach are suggested. The transmissivity can be added to more realistically represent tree crowns and their phenological changes over time. The assessment of pedestrian thermal comfort level in Chapter 2 uses two heat indices (*HI* and *WCI*), and heat- and cold-related mortality was estimated based on previous research. However, a recent study suggests that population dynamics, such as work-related commutes, can modify the exposure of pedestrian to extreme temperatures (Yang, Hu, and Wang 2019). More importantly, the developed framework only incorporates the radiative shading effect, while other important biophysical functions of trees (Ryu et al. 2016) such as ET are excluded. Future numerical studies on the cooling effect of urban trees will be improved via: (i) more realistic representation of tree crowns, (ii) incorporation of ET and root-water uptake in the framework, (iii) large continental scale simulations with spatial resolution much finer than 20 km, and (iv) advanced evaluation of thermal comfort level by incorporating other meteorological variables and population dynamics.

The quantification of how urban trees and their cooling capacity response to thermal extremes (heat waves and cold spells) in Chapter 4 uses remotely sensed products at 1-km spatial resolution. Existing studies have suggested that variations in the cooling effect and cooling capacity of urban trees exist as influenced by a variety of variables such as tree spatial arrangement, composition, and the adopted spatial resolution or window size in the analysis (W. Zhou, Wang, and Cadenasso 2017; Z.-H. Wang, Fan, et al. 2016). Generalizing the cooling capacity of urban trees may require

refined considerations, including (i) sensitivity analysis using remote sensing products with various spatial resolutions, (ii) evaluation on the diurnal change of cooling capacity based on remote sensing products with high temporal scale, and (iii) the use of detailed urban tree inventory as a substitute for remotely sensed data at sub-urban scale. *In situ* measurements on the same phenomenon, although can be limited in both spatial and temporal scales, are strongly suggested to examine how the ET cooling of urban trees responses to thermal extremes.

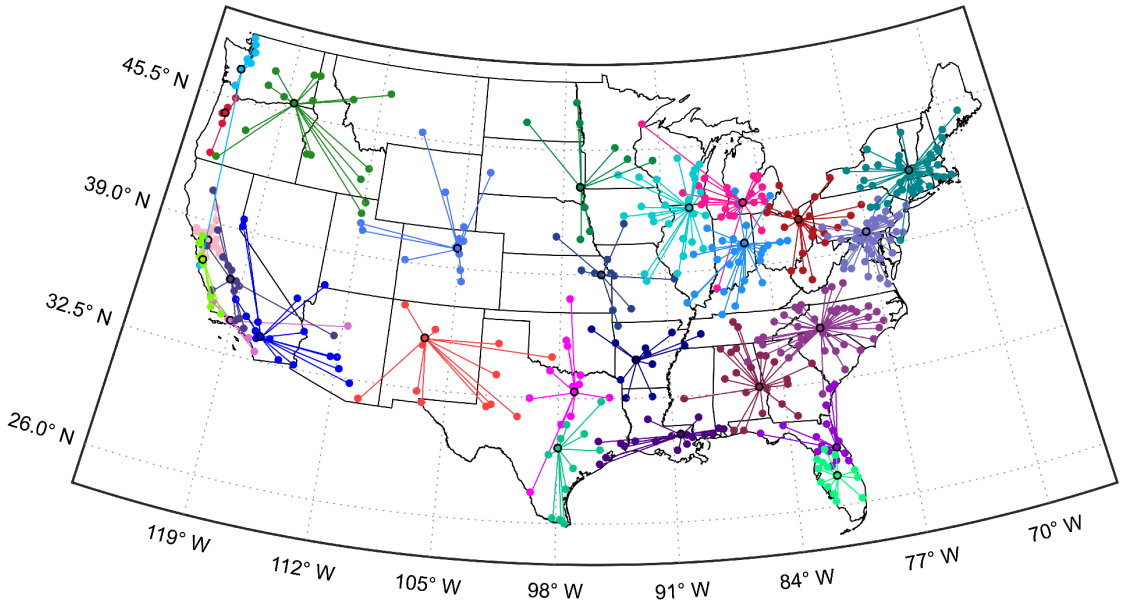

Figure 5.1. Illustration of urban clustering during a heat wave in July 12–19, 2006. Cities with black edges are centers of clusters.

It is noteworthy that both numerical simulations (Chapter 3) and analysis based on remotely sensed data (Chapter 4) suggest strong variability of the cooling effect or capacity provided by urban trees among cities. Urban trees, or more generally, various

urban mitigation and adaptation strategies, need to be judiciously adopted in cities with different geographical conditions. Meanwhile, the similarity in urban components results in analogous response to environmental stressors (e.g., a heat wave), especially when the geographical or climatic conditions are alike (S. Peng et al. 2012). These similarities highlight the potential of viewing cities as highly connected or teleconnected systems, organized clusters, or even complex networks at multiple scales (Seto et al. 2012). As an example, Figure 5.1 shows the clustering pattern of all CONUS cities during a heat wave in 2006 (C. Wang, Wang, and Li 2019). The urban clustering is based on both geographical distance and similarity in LST using the affinity propagation method (Frey and Dueck 2007). The topological structure observed in such analyses not only represents the geographical or climatic similarity, but also offers a more fundamental and holistic means for system-based (instead of process-based) sustainable urban development. For example, one may infer that implementing urban green infrastructure in a like manner would generate similar cooling effect in cities located within the same cluster (e.g., Fig. 5.1) or connected in a network. Examining the connectivity or clustering of cities is therefore imperative in the large-scale implementation of urban planning strategies, especially those in the top-down blue-print planning.

REFERENCES

AASHTO. 2011. *A Policy on Geometric Design of Highways and Streets*, 6th ed. Washington DC, USA: American Association of State Highway and Transportation Officials.

Abhijith, K. V., Prashant Kumar, John Gallagher, Aonghus McNabola, Richard Baldauf, Francesco Pilla, Brian Broderick, Silvana Di Sabatino, and Beatrice Pulvirenti. 2017. "Air Pollution Abatement Performances of Green Infrastructure in Open Road and Built-up Street Canyon Environments – A Review." *Atmospheric Environment* 162: 71–86. https://doi.org/10.1016/j.atmosenv.2017.05.014.

Akbari, Hashem, and Dionysia Kolokotsa. 2016. "Three Decades of Urban Heat Islands and Mitigation Technologies Research." *Energy and Buildings* 133: 834–42. https://doi.org/10.1016/j.enbuild.2016.09.067.

Akbari, Hashem, M. Pomerantz, and H. Taha. 2001. "Cool Surfaces and Shade Trees to Reduce Energy Use and Improve Air Quality in Urban Areas." *Solar Energy* 70 (3): 295–310. https://doi.org/10.1016/S0038-092X(00)00089-X.

Albertson, John D. 1996. "Large Eddy Simulation of Land-Atmosphere Interaction." PhD diss., University of California, Davis.

Albertson, John D., and Marc B. Parlange. 1999. "Surface Length Scales and Shear Stress: Implications for Land-Atmosphere Interaction over Complex Terrain." *Water Resources Research* 35 (7): 2121–32. https://doi.org/10.1029/1999WR900094.

Alduchov, Oleg A., and Robert E. Eskridge. 1996. "Improved Magnus Form Approximation of Saturation Vapor Pressure." *Journal of Applied Meteorology* 35 (4): 601–9. https://doi.org/10.1175/1520-0450(1996)035<0601:IMFAOS>2.0.CO;2.

Amorim, J. H., V. Rodrigues, R. Tavares, J. Valente, and C. Borrego. 2013. "CFD Modelling of the Aerodynamic Effect of Trees on Urban Air Pollution Dispersion." *Science of the Total Environment* 461: 541–51. https://doi.org/10.1016/j.scitotenv.2013.05.031.

Anderson, G. Brooke, and Michelle L. Bell. 2011. "Heat Waves in the United States: Mortality Risk during Heat Waves and Effect Modification by Heat Wave Characteristics in 43 US Communities." *Environmental Health Perspectives* 119 (2): 210–18. https://doi.org/10.1289/ehp.1002313.

Arnfield, A. John. 2003. "Two Decades of Urban Climate Research: A Review of Turbulence, Exchanges of Energy and Water, and the Urban Heat Island." *International Journal of Climatology* 23 (1): 1–26. https://doi.org/10.1002/joc.859.

Belcher, Stephen E., Ian N. Harman, and John J. Finnigan. 2012. “The Wind in the Willows: Flows in Forest Canopies in Complex Terrain.” *Annual Review of Fluid Mechanics* 44 (1): 479–504. https://doi.org/10.1146/annurev-fluid-120710-101036.

Bettencourt, Luís M. A., José Lobo, Dirk Helbing, Christian Kühnert, and Geoffrey B. West. 2007. “Growth, Innovation, Scaling, and the Pace of Life in Cities.” *Proceedings of the National Academy of Sciences of the United States of America* 104 (17): 7301–6. https://doi.org/10.1073/pnas.0610172104.

Bou-Zeid, Elie, Charles Meneveau, and Marc Parlange. 2005. “A Scale-Dependent Lagrangian Dynamic Model for Large Eddy Simulation of Complex Turbulent Flows.” *Physics of Fluids* 17 (2): 025105. https://doi.org/10.1063/1.1839152.

Bou-Zeid, Elie, Jan Overney, Benedict D. Rogers, and Marc B. Parlange. 2009. “The Effects of Building Representation and Clustering in Large-Eddy Simulations of Flows in Urban Canopies.” *Boundary-Layer Meteorology* 132 (3): 415–36. https://doi.org/10.1007/s10546-009-9410-6.

Bowler, Diana E., Lisette Buyung-Ali, Teri M. Knight, and Andrew S. Pullin. 2010. “Urban Greening to Cool Towns and Cities: A Systematic Review of the Empirical Evidence.” *Landscape and Urban Planning* 97 (3): 147–55. https://doi.org/10.1016/j.landurbplan.2010.05.006.

Breyer, Betsy, Heejun Chang, and G. Hossein Parandvash. 2012. “Land-Use, Temperature, and Single-Family Residential Water Use Patterns in Portland, Oregon and Phoenix, Arizona.” *Applied Geography* 35 (1): 142–51. https://doi.org/10.1016/j.apgeog.2012.06.012.

Cai, X.-M., J. F. Barlow, and S. E. Belcher. 2008. “Dispersion and Transfer of Passive Scalars in and above Street Canyons–Large-Eddy Simulations.” *Atmospheric Environment* 42 (23): 5885–95. https://doi.org/10.1016/j.atmosenv.2008.03.040.

Calfapietra, Carlo, Josep Peñuelas, and Ülo Niinemets. 2015. “Urban Plant Physiology: Adaptation-Mitigation Strategies under Permanent Stress.” *Trends in Plant Science* 20 (2): 72–75. https://doi.org/10.1016/j.tplants.2014.11.001.

Caton, F., R. E. Britter, and S. Dalziel. 2003. “Dispersion Mechanisms in a Street Canyon.” *Atmospheric Environment* 37 (5): 693–702. https://doi.org/10.1016/S1352-2310(02)00830-0.

Cernusak, Lucas A., Nerea Ubierna, Michael W. Jenkins, Steven R. Garrity, Thom Rahn, Heath H. Powers, David T. Hanson, et al. 2018. “Unsaturation of Vapour Pressure inside Leaves of Two Conifer Species.” *Scientific Reports* 8 (1): 7667. https://doi.org/10.1038/s41598-018-25838-2.

Chan, Chak K., and Xiaohong Yao. 2008. “Air Pollution in Mega Cities in China.” *Atmospheric Environment* 42 (1): 1–42. https://doi.org/10.1016/j.atmosenv.2007.09.003.

Chen, Fei, Hiroyuki Kusaka, Robert Bornstein, Jason Ching, C. S. B. Grimmond, Susanne Grossman-Clarke, Thomas Loridan, et al. 2011. “The Integrated WRF/Urban Modelling System: Development, Evaluation, and Applications to Urban Environmental Problems.” *International Journal of Climatology* 31 (2): 273–88. https://doi.org/10.1002/joc.2158.

Chester, Stuart, Charles Meneveau, and Marc B. Parlange. 2007. “Modeling Turbulent Flow over Fractal Trees with Renormalized Numerical Simulation.” *Journal of Computational Physics* 225 (1): 427–48. https://doi.org/10.1016/j.jcp.2006.12.009.

Chudnovsky, A., E. Ben-Dor, and H. Saaroni. 2004. “Diurnal Thermal Behavior of Selected Urban Objects Using Remote Sensing Measurements.” *Energy and Buildings* 36 (11): 1063–74. https://doi.org/10.1016/j.enbuild.2004.01.052.

Coumou, Dim, and Stefan Rahmstorf. 2012. “A Decade of Weather Extremes.” *Nature Climate Change* 2 (7): 491–96. https://doi.org/10.1038/nclimate1452.

Crawford, Amanda J., Deirdre H. McLachlan, Alistair M. Hetherington, and Keara A. Franklin. 2012. “High Temperature Exposure Increases Plant Cooling Capacity.” *Current Biology* 22 (10): R396–97. https://doi.org/10.1016/j.cub.2012.03.044.

Curriero, Frank C., Karlyn S. Heiner, Jonathan M. Samet, Scott L. Zeger, Lisa Strug, and Jonathan A. Patz. 2002. “Temperature and Mortality in 11 Cities of the Eastern United States.” *American Journal of Epidemiology* 155 (1): 80–87.

David, T. S., M. I. Ferreira, S. Cohen, J. S. Pereira, and J. S. David. 2004. “Constraints on Transpiration from an Evergreen Oak Tree in Southern Portugal.” *Agricultural and Forest Meteorology* 122 (3): 193–205. https://doi.org/10.1016/j.agrformet.2003.09.014.

Diffenbaugh, Noah S., Deepti Singh, Justin S. Mankin, Daniel E. Horton, Daniel L. Swain, Danielle Touma, Allison Charland, et al. 2017. “Quantifying the Influence of Global Warming on Unprecedented Extreme Climate Events.” *Proceedings of the National Academy of Sciences of the United States of America* 114 (19): 4881–86. https://doi.org/10.1073/pnas.1618082114.

DiMiceli, C., M. Carroll, R. Sohlberg, D. H. Kim, M. Kelly, and J. R. G. Townshend. 2015. *MOD44B MODIS/Terra Vegetation Continuous Fields Yearly L3 Global 250m SIN Grid V006*. NASA EOSDIS Land Processes DAAC. https://doi.org/10.5067/modis/mod44b.006.

Epstein, Yoram, and Daniel S. Moran. 2006. “Thermal Comfort and the Heat Stress Indices.” *Industrial Health* 44 (3): 388–98. https://doi.org/10.2486/indhealth.44.388.

Erell, Evyatar, David Pearlmutter, and Terence Williamson. 2011. *Urban Microclimate: Designing the Spaces between Buildings*. London, UK: Earthscan Ltd.

Ewers, B. E., S. T. Gower, B. Bond-Lamberty, and C. K. Wang. 2005. “Effects of Stand Age and Tree Species on Canopy Transpiration and Average Stomatal Conductance of Boreal Forests.” *Plant, Cell & Environment* 28 (5): 660–78. https://doi.org/10.1111/j.1365-3040.2005.01312.x.

Fan, Chao, Soe W. Myint, and Baojuan Zheng. 2015. “Measuring the Spatial Arrangement of Urban Vegetation and Its Impacts on Seasonal Surface Temperatures.” *Progress in Physical Geography: Earth and Environment* 39 (2): 199–219. https://doi.org/10.1177/0309133314567583.

Frey, Brendan J., and Delbert Dueck. 2007. “Clustering by Passing Messages between Data Points.” *Science* 315 (5814): 972–76. https://doi.org/10.1126/science.1136800.

Georgi, Julia N., and Dimos Dimitriou. 2010. “The Contribution of Urban Green Spaces to the Improvement of Environment in Cities: Case Study of Chania, Greece.” *Building and Environment* 45 (6): 1401–14. https://doi.org/10.1016/j.buildenv.2009.12.003.

Gillies, J. A., W. G. Nickling, and J. King. 2002. “Drag Coefficient and Plant Form Response to Wind Speed in Three Plant Species: Burning Bush (*Euonymus Alatus*), Colorado Blue Spruce (*Picea Pungens* Glauca.), and Fountain Grass (*Pennisetum Setaceum*).” *Journal of Geophysical Research: Atmospheres* 107 (D24): 4760. https://doi.org/10.1029/2001JD001259.

Giometto, M. G., A. Christen, P. E. Egli, M. F. Schmid, R. T. Tooke, N. C. Coops, and M. B. Parlange. 2017. “Effects of Trees on Mean Wind, Turbulence and Momentum Exchange within and above a Real Urban Environment.” *Advances in Water Resources* 106: 154–68. https://doi.org/10.1016/j.advwatres.2017.06.018.

Gregg, Jillian W., Clive G. Jones, and Todd E. Dawson. 2003. “Urbanization Effects on Tree Growth in the Vicinity of New York City.” *Nature* 424 (6945): 183–87. https://doi.org/10.1038/nature01728.

Grimm, Nancy B., Stanley H. Faeth, Nancy E. Golubiewski, Charles L. Redman, Jianguo Wu, Xuemei Bai, and John M. Briggs. 2008. “Global Change and the Ecology of Cities.” *Science* 319 (5864): 756–60. https://doi.org/10.1126/science.1150195.

Grimmond, Sue. 2007. “Urbanization and Global Environmental Change: Local Effects of Urban Warming.” *The Geographical Journal* 173 (1): 83–88. https://doi.org/10.1111/j.1475-4959.2007.232_3.x.

Gromke, Christof, and Bert Blocken. 2015. “Influence of Avenue-Trees on Air Quality at the Urban Neighborhood Scale. Part II: Traffic Pollutant Concentrations at Pedestrian Level.” *Environmental Pollution* 196: 176–84. https://doi.org/10.1016/j.envpol.2014.10.015.

Gromke, Christof, Bert Blocken, Wendy Janssen, Bart Merema, Twan van Hooff, and Harry Timmermans. 2015. “CFD Analysis of Transpirational Cooling by Vegetation: Case Study for Specific Meteorological Conditions during a Heat Wave in Arnhem, Netherlands.” *Building and Environment* 83: 11–26. https://doi.org/10.1016/j.buildenv.2014.04.022.

Gromke, Christof, Riccardo Buccolieri, Silvana Di Sabatino, and Bodo Ruck. 2008. “Dispersion Study in a Street Canyon with Tree Planting by Means of Wind Tunnel and Numerical Investigations – Evaluation of CFD Data with Experimental Data.” *Atmospheric Environment* 42 (37): 8640–50. https://doi.org/10.1016/j.atmosenv.2008.08.019.

Gromke, Christof, Nabaraj Jamarkattel, and Bodo Ruck. 2016. “Influence of Roadside Hedgerows on Air Quality in Urban Street Canyons.” *Atmospheric Environment* 139: 75–86. https://doi.org/10.1016/j.atmosenv.2016.05.014.

Gromke, Christof, and Bodo Ruck. 2007. “Influence of Trees on the Dispersion of Pollutants in an Urban Street Canyon—Experimental Investigation of the Flow and Concentration Field.” *Atmospheric Environment* 41 (16): 3287–3302. https://doi.org/10.1016/j.atmosenv.2006.12.043.

———. 2008. “Aerodynamic Modelling of Trees for Small-Scale Wind Tunnel Studies.” *Forestry* 81 (3): 243–58. https://doi.org/10.1093/forestry/cpn027.

———. 2009. “On the Impact of Trees on Dispersion Processes of Traffic Emissions in Street Canyons.” *Boundary-Layer Meteorology* 131 (1): 19–34. https://doi.org/10.1007/s10546-008-9301-2.

———. 2012. “Pollutant Concentrations in Street Canyons of Different Aspect Ratio with Avenues of Trees for Various Wind Directions.” *Boundary-Layer Meteorology* 144 (1): 41–64. https://doi.org/10.1007/s10546-012-9703-z.

Hamada, Shuko, and Takeshi Ohta. 2010. “Seasonal Variations in the Cooling Effect of Urban Green Areas on Surrounding Urban Areas.” *Urban Forestry & Urban Greening* 9 (1): 15–24. https://doi.org/10.1016/j.ufug.2009.10.002.

Hamerlynck, Erik P., Travis E. Huxman, Michael E. Loik, and Stanley D. Smith. 2000. “Effects of Extreme High Temperature, Drought and Elevated CO_2 on

Photosynthesis of the Mojave Desert Evergreen Shrub, *Larrea Tridentata*." *Plant Ecology* 148 (2): 183–93. https://doi.org/10.1023/A:1009896111405.

Hansen, M. C., R. S. DeFries, J. R. G. Townshend, R. Sohlberg, C. Dimiceli, and M. Carroll. 2002. "Towards an Operational MODIS Continuous Field of Percent Tree Cover Algorithm: Examples Using AVHRR and MODIS Data." *Remote Sensing of Environment* 83 (1–2): 303–19. https://doi.org/10.1016/S0034-4257(02)00079-2.

Harlan, Sharon L., Anthony J. Brazel, Lela Prashad, William L. Stefanov, and Larissa Larsen. 2006. "Neighborhood Microclimates and Vulnerability to Heat Stress." *Social Science & Medicine* 63 (11): 2847–63. https://doi.org/10.1016/j.socscimed.2006.07.030.

Hatfield, Jerry L., and John H. Prueger. 2015. "Temperature Extremes: Effect on Plant Growth and Development." *Weather and Climate Extremes* 10: 4–10. https://doi.org/10.1016/j.wace.2015.08.001.

Holmer, Björn, Sofia Thorsson, and Jenny Lindén. 2013. "Evening Evapotranspirative Cooling in Relation to Vegetation and Urban Geometry in the City of Ouagadougou, Burkina Faso." *International Journal of Climatology* 33 (15): 3089–3105. https://doi.org/10.1002/joc.3561.

Homer, Collin G., Jon A. Dewitz, Limin Yang, Suming Jin, Patrick Danielson, George Xian, John Coulston, Nathaniel D. Herold, J. D. Wickham, and Kevin Megown. 2015. "Completion of the 2011 National Land Cover Database for the Conterminous United States-Representing a Decade of Land Cover Change Information." *Photogrammetric Engineering and Remote Sensing* 81 (5): 345–54.

Höppe, P. 1999. "The Physiological Equivalent Temperature – a Universal Index for the Biometeorological Assessment of the Thermal Environment." *International Journal of Biometeorology* 43 (2): 71–75. https://doi.org/10.1007/s004840050118.

Howells, Mark, Sebastian Hermann, Manuel Welsch, Morgan Bazilian, Rebecka Segerström, Thomas Alfstad, Dolf Gielen, et al. 2013. "Integrated Analysis of Climate Change, Land-Use, Energy and Water Strategies." *Nature Climate Change* 3 (7): 621–26. https://doi.org/10.1038/nclimate1789.

Hsieh, Cheng-I., and Gabriel Katul. 2009. "The Lagrangian Stochastic Model for Estimating Footprint and Water Vapor Fluxes over Inhomogeneous Surfaces." *International Journal of Biometeorology* 53 (1): 87–100. https://doi.org/10.1007/s00484-008-0193-0.

Jackson, Robert B., James T. Randerson, Josep G. Canadell, Ray G. Anderson, Roni Avissar, Dennis D. Baldocchi, Gordon B. Bonan, et al. 2008. "Protecting Climate

with Forests." *Environmental Research Letters* 3 (4): 044006. https://doi.org/10.1088/1748-9326/3/4/044006.

Janhäll, Sara. 2015. "Review on Urban Vegetation and Particle Air Pollution – Deposition and Dispersion." *Atmospheric Environment* 105: 130–37. https://doi.org/10.1016/j.atmosenv.2015.01.052.

Jeanjean, A. P. R., Riccardo Buccolieri, James Eddy, Paul S. Monks, and Roland J. Leigh. 2017. "Air Quality Affected by Trees in Real Street Canyons: The Case of Marylebone Neighbourhood in Central London." *Urban Forestry & Urban Greening* 22: 41–53. https://doi.org/10.1016/j.ufug.2017.01.009.

Jeanjean, A. P. R., P. S. Monks, and R. J. Leigh. 2016. "Modelling the Effectiveness of Urban Trees and Grass on PM2.5 Reduction via Dispersion and Deposition at a City Scale." *Atmospheric Environment* 147: 1–10. https://doi.org/10.1016/j.atmosenv.2016.09.033.

Jenerette, G. Darrel, Sharon L. Harlan, Alexander Buyantuev, William L. Stefanov, Juan Declet-Barreto, Benjamin L. Ruddell, Soe Win Myint, Shai Kaplan, and Xiaoxiao Li. 2016. "Micro-Scale Urban Surface Temperatures Are Related to Land-Cover Features and Residential Heat Related Health Impacts in Phoenix, AZ USA." *Landscape Ecology* 31 (4): 745–60. https://doi.org/10.1007/s10980-015-0284-3.

Jin, Menglin, Robert E. Dickinson, and D. A. Zhang. 2005. "The Footprint of Urban Areas on Global Climate as Characterized by MODIS." *Journal of Climate* 18 (10): 1551–65. https://doi.org/10.1175/JCLI3334.1.

Jin, Sijia, Jiankang Guo, Stephen Wheeler, Liyan Kan, and Shengquan Che. 2014. "Evaluation of Impacts of Trees on $PM_{2.5}$ Dispersion in Urban Streets." *Atmospheric Environment* 99: 277–87. https://doi.org/10.1016/j.atmosenv.2014.10.002.

Kalnay, Eugenia, and Ming Cai. 2003. "Impact of Urbanization and Land-Use Change on Climate." *Nature* 423 (6939): 528–31. https://doi.org/10.1038/nature01675.

Kim, Jae-Jin, and Jong-Jin Baik. 2001. "Urban Street-Canyon Flows with Bottom Heating." *Atmospheric Environment* 35 (20): 3395–3404. https://doi.org/10.1016/S1352-2310(01)00135-2.

Kjelgren, Roger, and Thayne Montague. 1998. "Urban Tree Transpiration over Turf and Asphalt Surfaces." *Atmospheric Environment* 32 (1): 35–41. https://doi.org/10.1016/S1352-2310(97)00177-5.

Konarska, Janina, Björn Holmer, Fredrik Lindberg, and Sofia Thorsson. 2016. "Influence of Vegetation and Building Geometry on the Spatial Variations of Air Temperature and Cooling Rates in a High-Latitude City." *International Journal of Climatology* 36 (5): 2379–95. https://doi.org/10.1002/joc.4502.

Konarska, Janina, Johan Uddling, Björn Holmer, Martina Lutz, Fredrik Lindberg, Håkan Pleijel, and Sofia Thorsson. 2016. “Transpiration of Urban Trees and Its Cooling Effect in a High Latitude City.” *International Journal of Biometeorology* 60 (1): 159–72. https://doi.org/10.1007/s00484-015-1014-x.

Kottek, Markus, Jürgen Grieser, Christoph Beck, Bruno Rudolf, and Franz Rubel. 2006. “World Map of the Köppen-Geiger Climate Classification Updated.” *Meteorologische Zeitschrift* 15 (3): 259–63. https://doi.org/10.1127/0941-2948/2006/0130.

Krayenhoff, E. S., A. Christen, A. Martilli, and T. R. Oke. 2014. “A Multi-Layer Radiation Model for Urban Neighbourhoods with Trees.” *Boundary-Layer Meteorology* 151 (1): 139–78. https://doi.org/10.1007/s10546-013-9883-1.

Krayenhoff, E. S., J.-L. Santiago, A. Martilli, A. Christen, and T. R. Oke. 2015. “Parametrization of Drag and Turbulence for Urban Neighbourhoods with Trees.” *Boundary-Layer Meteorology* 156 (2): 157–89. https://doi.org/10.1007/s10546-015-0028-6.

Kumar, Vijayant, Jan Kleissl, Charles Meneveau, and Marc B. Parlange. 2006. “Large-eddy Simulation of a Diurnal Cycle of the Atmospheric Boundary Layer: Atmospheric Stability and Scaling Issues.” *Water Resources Research* 42 (6): W06D09. https://doi.org/10.1029/2005WR004651.

Lalic, Branislava, and Dragutin T. Mihailovic. 2004. “An Empirical Relation Describing Leaf-Area Density inside the Forest for Environmental Modeling.” *Journal of Applied Meteorology* 43 (4): 641–45. https://doi.org/10.1175/1520-0450(2004)043<0641:AERDLD>2.0.CO;2.

Lanzani, Guido, and Matted Tamponi. 1995. “A Microscale Lagrangian Particle Model for the Dispersion of Primary Pollutants in a Street CANYON. Sensitivity Analysis and First Validation Trials.” *Atmospheric Environment* 29 (23): 3465–75. https://doi.org/10.1016/1352-2310(95)00104-7.

Lee, Sang-Hyun, Hyunho Lee, Seung-Bu Park, Ju-Wan Woo, Doo-Il Lee, and Jong-Jin Baik. 2016. “Impacts of In-Canyon Vegetation and Canyon Aspect Ratio on the Thermal Environment of Street Canyons: Numerical Investigation Using a Coupled WRF-VUCM Model.” *Quarterly Journal of the Royal Meteorological Society* 142 (699): 2562–78. https://doi.org/10.1002/qj.2847.

Lee, Sang-Hyun, and Soon-Ung Park. 2008. “A Vegetated Urban Canopy Model for Meteorological and Environmental Modelling.” *Boundary-Layer Meteorology* 126 (1): 73–102. https://doi.org/10.1007/s10546-007-9221-6.

Leung, Dennis Y. C., Jeanie K. Y. Tsui, Feng Chen, Wing-Kin Yip, Lilian L. P. Vrijmoed, and Chun-Ho Liu. 2011. “Effects of Urban Vegetation on Urban Air

Quality." *Landscape Research* 36 (2): 173–88. https://doi.org/10.1080/01426397.2010.547570.

Li, Qi, Elie Bou-Zeid, and William Anderson. 2016. "The Impact and Treatment of the Gibbs Phenomenon in Immersed Boundary Method Simulations of Momentum and Scalar Transport." *Journal of Computational Physics* 310: 237–51. https://doi.org/10.1016/j.jcp.2016.01.013.

Li, Qi, Elie Bou-Zeid, William Anderson, Sue Grimmond, and Marcus Hultmark. 2016. "Quality and Reliability of LES of Convective Scalar Transfer at High Reynolds Numbers." *International Journal of Heat and Mass Transfer* 102: 959–70. https://doi.org/10.1016/j.ijheatmasstransfer.2016.06.093.

Li, Qi, and Zhi-Hua Wang. 2018. "Large-Eddy Simulation of the Impact of Urban Trees on Momentum and Heat Fluxes." *Agricultural and Forest Meteorology*, Honoring W. J. Massman's Discoveries: Bringing Physics to Agriculture, 255: 44–56. https://doi.org/10.1016/j.agrformet.2017.07.011.

Lin, Hua, Yajun Chen, Houlei Zhang, Peili Fu, and Zexin Fan. 2017. "Stronger Cooling Effects of Transpiration and Leaf Physical Traits of Plants from a Hot Dry Habitat than from a Hot Wet Habitat." *Functional Ecology* 31 (12): 2202–11. https://doi.org/10.1111/1365-2435.12923.

Loughner, Christopher P., Dale J. Allen, Da-Lin Zhang, Kenneth E. Pickering, Russell R. Dickerson, and Laura Landry. 2012. "Roles of Urban Tree Canopy and Buildings in Urban Heat Island Effects: Parameterization and Preliminary Results." *Journal of Applied Meteorology and Climatology* 51 (10): 1775–93. https://doi.org/10.1175/JAMC-D-11-0228.1.

Louka, P., S. E. Belcher, and R. G. Harrison. 1998. "Modified Street Canyon Flow." *Journal of Wind Engineering and Industrial Aerodynamics* 74–76: 485–93. https://doi.org/10.1016/S0167-6105(98)00044-0.

Manickathan, Lento, Thijs Defraeye, Jonas Allegrini, Dominique Derome, and Jan Carmeliet. 2018. "Parametric Study of the Influence of Environmental Factors and Tree Properties on the Transpirative Cooling Effect of Trees." *Agricultural and Forest Meteorology* 248: 259–74. https://doi.org/10.1016/j.agrformet.2017.10.014.

Mei, Shuo-Jun, Cheng-Wei Liu, Di Liu, Fu-Yun Zhao, Han-Qing Wang, and Xiao-Hong Li. 2016. "Fluid Mechanical Dispersion of Airborne Pollutants inside Urban Street Canyons Subjecting to Multi-Component Ventilation and Unstable Thermal Stratifications." *Science of the Total Environment* 565: 1102–15. https://doi.org/10.1016/j.scitotenv.2016.05.150.

Middel, Ariane, Nalini Chhetri, and Raymond Quay. 2015. "Urban Forestry and Cool Roofs: Assessment of Heat Mitigation Strategies in Phoenix Residential

Neighborhoods." *Urban Forestry & Urban Greening* 14 (1): 178–86. https://doi.org/10.1016/j.ufug.2014.09.010.

Myint, Soe W., Elizabeth A. Wentz, Anthony J. Brazel, and Dale A. Quattrochi. 2013. "The Impact of Distinct Anthropogenic and Vegetation Features on Urban Warming." *Landscape Ecology* 28 (5): 959–78. https://doi.org/10.1007/s10980-013-9868-y.

Myint, Soe W., Baojuan Zheng, Emily Talen, Chao Fan, Shai Kaplan, Ariane Middel, Martin Smith, Huei-Ping Huang, and Anthony Brazel. 2015. "Does the Spatial Arrangement of Urban Landscape Matter? Examples of Urban Warming and Cooling in Phoenix and Las Vegas." *Ecosystem Health and Sustainability* 1 (4): 1–15. https://doi.org/10.1890/EHS14-0028.1.

NACTO. 2017. "Urban Street Design Guide." Last modified July 24, 2015. https://nacto.org/publication/urban-street-design-guide/streets/.

National Centers for Environmental Prediction. 2000. *NCEP FNL Operational Model Global Tropospheric Analyses, Continuing from July 1999 (Updated Daily)*. National Center for Atmospheric Research, Computational and Information Systems Laboratory. https://doi.org/10.5065/D6M043C6."

NOAA. 2007. "Weather Safety - NOAA's National Weather Service." Accessed September 22, 2016. http://www.nws.noaa.gov/safety.php.

Nowak, David J., Miki Kuroda, and Daniel E. Crane. 2004. "Tree Mortality Rates and Tree Population Projections in Baltimore, Maryland, USA." *Urban Forestry & Urban Greening* 2 (3): 139–47. https://doi.org/10.1078/1618-8667-00030.

Oke, T. R. 1988a. "The Urban Energy Balance." *Progress in Physical Geography* 12 (4): 471–508. https://doi.org/10.1177%2F030913338801200401.

———. 1988b. "Street Design and Urban Canopy Layer Climate." *Energy and Buildings* 11 (1): 103–13. https://doi.org/10.1016/0378-7788(88)90026-6.

———. 2006. "Towards Better Scientific Communication in Urban Climate." *Theoretical and Applied Climatology* 84 (1–3): 179–90. https://doi.org/10.1007/s00704-005-0153-0.

Oke, T. R., J. M. Crowther, K. G. McNaughton, J. L. Monteith, and B. Gardiner. 1989. "The Micrometeorology of the Urban Forest." *Philosophical Transactions of the Royal Society of London B: Biological Sciences* 324 (1223): 335–49. https://doi.org/10.1098/rstb.1989.0051.

Oke, T. R., G. Mills, A. Christen, and J. A. Voogt. 2017. *Urban Climates*. Cambridge, UK: Cambridge University Press.

Orszag, Steven A. 1971. “On the Elimination of Aliasing in Finite-Difference Schemes by Filtering High-Wavenumber Components.” *Journal of the Atmospheric Sciences* 28 (6): 1074. https://doi.org/10.1175/1520-0469(1971)028<1074:OTEOAI>2.0.CO;2.

Pan, Ying, Marcelo Chamecki, and Scott A. Isard. 2014. “Large-Eddy Simulation of Turbulence and Particle Dispersion inside the Canopy Roughness Sublayer.” *Journal of Fluid Mechanics* 753: 499–534. https://doi.org/10.1017/jfm.2014.379.

Park, Minsun, Aya Hagishima, Jun Tanimoto, and Ken-ichi Narita. 2012. “Effect of Urban Vegetation on Outdoor Thermal Environment: Field Measurement at a Scale Model Site.” *Building and Environment* 56: 38–46. https://doi.org/10.1016/j.buildenv.2012.02.015.

Patton, Edward G., Peter P. Sullivan, Roger H. Shaw, John J. Finnigan, and Jeffrey C. Weil. 2016. “Atmospheric Stability Influences on Coupled Boundary Layer and Canopy Turbulence.” *Journal of the Atmospheric Sciences* 73 (4): 1621–47. https://doi.org/10.1175/JAS-D-15-0068.1.

Peng, Jian, Jinglei Jia, Yanxu Liu, Huilei Li, and Jiansheng Wu. 2018. “Seasonal Contrast of the Dominant Factors for Spatial Distribution of Land Surface Temperature in Urban Areas.” *Remote Sensing of Environment* 215: 255–67. https://doi.org/10.1016/j.rse.2018.06.010.

Peng, Jian, Pan Xie, Yanxu Liu, and Jing Ma. 2016. “Urban Thermal Environment Dynamics and Associated Landscape Pattern Factors: A Case Study in the Beijing Metropolitan Region.” *Remote Sensing of Environment* 173: 145–55. https://doi.org/10.1016/j.rse.2015.11.027.

Peng, Shushi, Shilong Piao, Philippe Ciais, Pierre Friedlingstein, Catherine Ottle, François-Marie Bréon, Huijuan Nan, Liming Zhou, and Ranga B. Myneni. 2012. “Surface Urban Heat Island across 419 Global Big Cities.” *Environmental Science & Technology* 46 (2): 696–703. https://doi.org/10.1021/es2030438.

Peterson, Thomas C., Richard R. Heim, Robert Hirsch, Dale P. Kaiser, Harold Brooks, Noah S. Diffenbaugh, Randall M. Dole, et al. 2013. “Monitoring and Understanding Changes in Heat Waves, Cold Waves, Floods, and Droughts in the United States: State of Knowledge.” *Bulletin of the American Meteorological Society* 94 (6): 821–34. https://doi.org/10.1175/BAMS-D-12-00066.1.

Phelan, Patrick E., Kamil Kaloush, Mark Miner, Jay Golden, Bernadette Phelan, Humberto Silva, and Robert A. Taylor. 2015. “Urban Heat Island: Mechanisms, Implications, and Possible Remedies.” *Annual Review of Environment and Resources* 40 (1): 285–307. https://doi.org/10.1146/annurev-environ-102014-021155.

Pinard, J. D. Jean-Paul, and John D. Wilson. 2001. “First- and Second-Order Closure Models for Wind in a Plant Canopy.” *Journal of Applied Meteorology* 40 (10): 1762–68. https://doi.org/10.1175/1520-0450(2001)040<1762:FASOCM>2.0.CO;2.

Quigley, Martin F. 2004. “Street Trees and Rural Conspecifics: Will Long-Lived Trees Reach Full Size in Urban Conditions?” *Urban Ecosystems* 7 (1): 29–39. https://doi.org/10.1023/B:UECO.0000020170.58404.e9.

Rahman, M. A., J. G. Smith, P. Stringer, and A. R. Ennos. 2011. “Effect of Rooting Conditions on the Growth and Cooling Ability of Pyrus Calleryana.” *Urban Forestry & Urban Greening* 10 (3): 185–92. https://doi.org/10.1016/j.ufug.2011.05.003.

Raupp, Michael J., Anne Buckelew Cumming, and Erin C. Raupp. 2006. “Street Tree Diversity in Eastern North America and Its Potential for Tree Loss to Exotic Borers.” *Arboriculture & Urban Forestry* 32 (6): 297–304.

Richards, K., and T. R. Oke. 2002. “Validation and Results of a Scale Model of Dew Deposition in Urban Environments.” *International Journal of Climatology* 22 (15): 1915–33. https://doi.org/10.1002/joc.856.

Rodean, Howard C. 1996. *Stochastic Lagrangian Models of Turbulent Diffusion*. Boston, USA: Meteorological Monographs, American Meteorological Society. https://doi.org/10.1007/978-1-935704-11-9.

Rotach, Mathias W. 2001. “Simulation of Urban-Scale Dispersion Using a Lagrangian Stochastic Dispersion Model.” *Boundary-Layer Meteorology* 99 (3): 379–410. https://doi.org/10.1023/A:1018973813500.

Rothfusz, Lans P. 1990. *The Heat Index Equation (or, More than You Ever Wanted to Know about Heat Index)*. Fort Worth, Texas: National Oceanic and Atmospheric Administration, National Weather Service, Office of Meteorology.

Roy, Sudipto, Jason Byrne, and Catherine Pickering. 2012. “A Systematic Quantitative Review of Urban Tree Benefits, Costs, and Assessment Methods across Cities in Different Climatic Zones.” *Urban Forestry & Urban Greening* 11 (4): 351–63. https://doi.org/10.1016/j.ufug.2012.06.006.

Ryu, Young-Hee, Elie Bou-Zeid, Zhi-Hua Wang, and James A. Smith. 2016. “Realistic Representation of Trees in an Urban Canopy Model.” *Boundary-Layer Meteorology* 159 (2): 193–220. https://doi.org/10.1007/s10546-015-0120-y.

Sailor, David J. 2011. “A Review of Methods for Estimating Anthropogenic Heat and Moisture Emissions in the Urban Environment.” *International Journal of Climatology* 31 (2): 189–99. https://doi.org/10.1002/joc.2106.

Sailor, David J., and Lu Lu. 2004. “A Top–down Methodology for Developing Diurnal and Seasonal Anthropogenic Heating Profiles for Urban Areas.” *Atmospheric Environment* 38 (17): 2737–48. https://doi.org/10.1016/j.atmosenv.2004.01.034.

Salim, Salim Mohamed, Siew Cheong Cheah, and Andrew Chan. 2011. “Numerical Simulation of Dispersion in Urban Street Canyons with Avenue-like Tree Plantings: Comparison between RANS and LES.” *Building and Environment* 46 (9): 1735–46. https://doi.org/10.1016/j.buildenv.2011.01.032.

Salmond, Jennifer A., Marc Tadaki, Sotiris Vardoulakis, Katherine Arbuthnott, Andrew Coutts, Matthias Demuzere, Kim N. Dirks, et al. 2016. “Health and Climate Related Ecosystem Services Provided by Street Trees in the Urban Environment.” *Environmental Health* 15 (S1): 95–111. https://doi.org/10.1186/s12940-016-0103-6.

Santamouris, M. 2014. “Cooling the Cities – A Review of Reflective and Green Roof Mitigation Technologies to Fight Heat Island and Improve Comfort in Urban Environments.” *Solar Energy* 103: 682–703. https://doi.org/10.1016/j.solener.2012.07.003.

Schläpfer, Markus, Joey Lee, and Luís Bettencourt. 2015. “Urban Skylines: Building Heights and Shapes as Measures of City Size.” *Preprint arXiv*:1512.00946.

Schlegel, Fabian, Jörg Stiller, Anne Bienert, Hans-Gerd Maas, Ronald Queck, and Christian Bernhofer. 2015. “Large-Eddy Simulation Study of the Effects on Flow of a Heterogeneous Forest at Sub-Tree Resolution.” *Boundary-Layer Meteorology* 154 (1): 27–56. https://doi.org/10.1007/s10546-014-9962-y.

Seto, Karen C., Michail Fragkias, Burak Güneralp, and Michael K. Reilly. 2011. “A Meta-Analysis of Global Urban Land Expansion.” *PLoS ONE* 6 (8): e23777. https://doi.org/10.1371/journal.pone.0023777.

Seto, Karen C., Burak Güneralp, and Lucy R. Hutyra. 2012. “Global Forecasts of Urban Expansion to 2030 and Direct Impacts on Biodiversity and Carbon Pools.” *Proceedings of the National Academy of Sciences of the United States of America* 109 (40): 16083–88. https://doi.org/10.1073/pnas.1211658109.

Seto, Karen C., Anette Reenberg, Christopher G Boone, Michail Fragkias, Dagmar Haase, Tobias Langanke, Peter Marcotullio, Darla K Munroe, Branislav Olah, and David Simon. 2012. “Urban Land Teleconnections and Sustainability.” *Proceedings of the National Academy of Sciences of the United States of America* 109 (20): 7687–92. https://doi.org/10.1073/pnas.1117622109.

Shahidan, Mohd. F., Mustafa K. M. Shariff, Phillip Jones, Elias Salleh, and Ahmad M. Abdullah. 2010. “A Comparison of Mesua Ferrea L. and Hura Crepitans L. for Shade Creation and Radiation Modification in Improving Thermal Comfort.”

Landscape and Urban Planning 97 (3): 168–81. https://doi.org/10.1016/j.landurbplan.2010.05.008.

Shashua-Bar, L., and M. E. Hoffman. 2000. “Vegetation as a Climatic Component in the Design of an Urban Street: An Empirical Model for Predicting the Cooling Effect of Urban Green Areas with Trees.” *Energy and Buildings* 31 (3): 221–35. https://doi.org/10.1016/S0378-7788(99)00018-3.

Shashua-Bar, L., and Milo E. Hoffman. 2002. “The Green CTTC Model for Predicting the Air Temperature in Small Urban Wooded Sites.” *Building and Environment* 37 (12): 1279–88. https://doi.org/10.1016/S0360-1323(01)00120-2.

Shashua-Bar, L., David Pearlmutter, and Evyatar Erell. 2009. “The Cooling Efficiency of Urban Landscape Strategies in a Hot Dry Climate.” *Landscape and Urban Planning* 92 (3): 179–86. https://doi.org/10.1016/j.landurbplan.2009.04.005.

Shaw, Roger H., and Ulrich Schumann. 1992. “Large-Eddy Simulation of Turbulent Flow above and within a Forest.” *Boundary-Layer Meteorology* 61 (1–2): 47–64. https://doi.org/10.1007/BF02033994.

Skamarock, William C., Joseph B. Klemp, Jimy Dudhia, David O. Gill, Dale M. Barker, M. G. Duda, X.-Y. Huang, Wei Wang, and Jordan G. Powers. 2008. *A Description of the Advanced Research WRF Version 3*. National Center for Atmospheric Research Technical Note. https://doi.org/10.5065/D68S4MVH.

Smith, William K. 1978. “Temperatures of Desert Plants: Another Perspective on the Adaptability of Leaf Size.” *Science* 201 (4356): 614–16. https://doi.org/10.1126/science.201.4356.614.

Song, Jiyun, and Zhi-Hua Wang. 2015a. “Interfacing the Urban Land-Atmosphere System through Coupled Urban Canopy and Atmospheric Models.” *Boundary-Layer Meteorology* 154 (3): 427–48. https://doi.org/10.1007/s10546-014-9980-9.

———. 2015b. “Impacts of Mesic and Xeric Urban Vegetation on Outdoor Thermal Comfort and Microclimate in Phoenix, AZ.” *Building and Environment* 94, Part 2: 558–68. https://doi.org/10.1016/j.buildenv.2015.10.016.

———. 2016. “Diurnal Changes in Urban Boundary Layer Environment Induced by Urban Greening.” *Environmental Research Letters* 11 (11): 114018. https://doi.org/10.1088/1748-9326/11/11/114018.

Song, Jiyun, Zhi-Hua Wang, and Chenghao Wang. 2017. “Biospheric and Anthropogenic Contributors to Atmospheric CO_2 Variability in a Residential Neighborhood of Phoenix, Arizona.” *Journal of Geophysical Research: Atmospheres* 122 (6): 3317–29. https://doi.org/10.1002/2016JD026267.

———. 2018. “The Regional Impact of Urban Heat Mitigation Strategies on Planetary Boundary-Layer Dynamics over a Semiarid City.” *Journal of Geophysical Research: Atmospheres* 123 (12): 6410–22. https://doi.org/10.1029/2018JD028302.

Spronken-Smith, R. A., and T. R. Oke. 1998. “The Thermal Regime of Urban Parks in Two Cities with Different Summer Climates.” *International Journal of Remote Sensing* 19 (11): 2085–2104. https://doi.org/10.1080/014311698214884.

———. 1999. “Scale Modelling of Nocturnal Cooling in Urban Parks.” *Boundary-Layer Meteorology* 93 (2): 287–312. https://doi.org/10.1023/A:1002001408973.

Stone Jr, Brian. 2005. “Urban Heat and Air Pollution: An Emerging Role for Planners in the Climate Change Debate.” *Journal of the American Planning Association* 71 (1): 13–25. https://doi.org/10.1080/01944360508976402.

Storch, Hans von, Heike Langenberg, and Frauke Feser. 2000. “A Spectral Nudging Technique for Dynamical Downscaling Purposes.” *Monthly Weather Review* 128 (10): 3664–73. https://doi.org/10.1175/1520-0493(2000)128<3664:ASNTFD>2.0.CO;2.

Su, Hong-Bing, Roger H. Shaw, and Kyaw Tha Paw U. 2000. “Two-Point Correlation Analysis of Meutrally Stratified Flow within and above a Forest from Large-Eddy Simulation.” *Boundary-Layer Meteorology* 94 (3): 423–60. https://doi.org/10.1023/A:1002430213742.

Tayyebi, Amin, and G. Darrel Jenerette. 2016. “Increases in the Climate Change Adaption Effectiveness and Availability of Vegetation across a Coastal to Desert Climate Gradient in Metropolitan Los Angeles, CA, USA.” *Science of the Total Environment* 548–549: 60–71. https://doi.org/10.1016/j.scitotenv.2016.01.049.

Tewari, Mukul, Hiroyuki Kusaka, Fei Chen, William J. Coirier, Sura Kim, Andrzej A. Wyszogrodzki, and Thomas T. Warner. 2010. “Impact of Coupling a Microscale Computational Fluid Dynamics Model with a Mesoscale Model on Urban Scale Contaminant Transport and Dispersion.” *Atmospheric Research* 96 (4): 656–64. https://doi.org/10.1016/j.atmosres.2010.01.006.

Thomson, D. J. 1987. “Criteria for the Selection of Stochastic Models of Particle Trajectories in Turbulent Flows.” *Journal of Fluid Mechanics* 180: 529–56. https://doi.org/10.1017/S0022112087001940.

Tominaga, Yoshihide, and Ted Stathopoulos. 2011. “CFD Modeling of Pollution Dispersion in a Street Canyon: Comparison between LES and RANS.” *Journal of Wind Engineering and Industrial Aerodynamics*, 99 (4): 340–48. https://doi.org/10.1016/j.jweia.2010.12.005.

———. 2016. “Ten Questions Concerning Modeling of Near-Field Pollutant Dispersion in the Built Environment.” *Building and Environment* 105: 390–402. https://doi.org/10.1016/j.buildenv.2016.06.027.

Townshend, J. 2016. *Global Forest Cover Change (GFCC) Tree Cover Multi-Year Global 30 m V003*. NASA EOSDIS Land Processes DAAC. https://doi.org/10.5067/measures/gfcc/gfcc30tc.003.

Townshend, John R., Jeffrey G. Masek, Chengquan Huang, Eric F. Vermote, Feng Gao, Saurabh Channan, Joseph O. Sexton, et al. 2012. “Global Characterization and Monitoring of Forest Cover Using Landsat Data: Opportunities and Challenges.” *International Journal of Digital Earth* 5 (5): 373–97. https://doi.org/10.1080/17538947.2012.713190.

Tseng, Yu-Heng, Charles Meneveau, and Marc B. Parlange. 2006. “Modeling Flow around Bluff Bodies and Predicting Urban Dispersion Using Large Eddy Simulation.” *Environmental Science & Technology* 40 (8): 2653–62. https://doi.org/10.1021/es051708m.

United Nations. 2015. *World Urbanization Prospects: The 2014 Revision*. United Nations, Department of Economic and Social Affairs, Population Division.

US EPA. 2008. *Reducing Urban Heat Islands: Compendium of Strategies*. United States Environmental Protection Agency.

Upreti, Ruby, Zhi-Hua Wang, and Jiachuan Yang. 2017. “Radiative Shading Effect of Urban Trees on Cooling the Regional Built Environment.” *Urban Forestry & Urban Greening* 26: 18–24. https://doi.org/10.1016/j.ufug.2017.05.008.

Urban, Josef, Miles W. Ingwers, Mary Anne McGuire, and Robert O. Teskey. 2017. “Increase in Leaf Temperature Opens Stomata and Decouples Net Photosynthesis from Stomatal Conductance in *Pinus Taeda* and *Populus Deltoides x Nigra*.” *Journal of Experimental Botany* 68 (7): 1757–67. https://doi.org/10.1093/jxb/erx052.

Voogt, J. A., and T. R. Oke. 2003. “Thermal Remote Sensing of Urban Climates.” *Remote Sensing of Environment* 86 (3): 370–84. https://doi.org/10.1016/S0034-4257(03)00079-8.

Vos, Peter E. J., Bino Maiheu, Jean Vankerkom, and Stijn Janssen. 2013. “Improving Local Air Quality in Cities: To Tree or Not to Tree?” *Environmental Pollution* 183: 113–22. https://doi.org/10.1016/j.envpol.2012.10.021.

Wan, Zhengming. 2014. “New Refinements and Validation of the Collection-6 MODIS Land-Surface Temperature/Emissivity Product.” *Remote Sensing of Environment* 140: 36–45. https://doi.org/10.1016/j.rse.2013.08.027.

Wan, Zhengming, S. Hook, and G. Hulley. 2015a. *MOD11A1 MODIS/Terra Land Surface Temperature/Emissivity Daily L3 Global 1km SIN Grid V006*. NASA EOSDIS Land Processes DAAC. https://doi.org/10.5067/MODIS/MOD11A1.006.

———. 2015b. *MYD11A1 MODIS/Aqua Land Surface Temperature/Emissivity Daily L3 Global 1km SIN Grid V006*. NASA EOSDIS Land Processes DAAC. https://doi.org/10.5067/MODIS/MYD11A1.006.

Wan, Zhengming, Yulin Zhang, Qincheng Zhang, and Zhao-liang Li. 2002. "Validation of the Land-Surface Temperature Products Retrieved from Terra Moderate Resolution Imaging Spectroradiometer Data." *Remote Sensing of Environment* 83 (1–2): 163–80. https://doi.org/10.1016/S0034-4257(02)00093-7.

Wang, Chenghao, Qi Li, and Zhi-Hua Wang. 2018. "Quantifying the Impact of Urban Trees on Passive Pollutant Dispersion Using a Coupled Large-Eddy Simulation–Lagrangian Stochastic Model." *Building and Environment* 145: 33–49. https://doi.org/10.1016/j.buildenv.2018.09.014.

Wang, Chenghao, Chuyuan Wang, Soe W. Myint, and Zhi-Hua Wang. 2017. "Landscape Determinants of Spatio-Temporal Patterns of Aerosol Optical Depth in the Two Most Polluted Metropolitans in the United States." *Science of the Total Environment* 609: 1556–65. https://doi.org/10.1016/j.scitotenv.2017.07.273.

Wang, Chenghao, and Zhi-Hua Wang. 2017. "Projecting Population Growth as a Dynamic Measure of Regional Urban Warming." *Sustainable Cities and Society* 32: 357–65. https://doi.org/10.1016/j.scs.2017.04.010.

Wang, Chenghao, Zhi-Hua Wang, and Qi Li. 2019. "Emergence of Urban Clustering among U.S. Cities under Environmental Stressors." *Science of the Total Environment*, under review.

Wang, Chenghao, Zhi-Hua Wang, Chuyuan Wang, and Soe W. Myint. 2019. "Environmental Cooling Provided by Urban Trees under Extreme Heat and Cold Waves in U.S. Cities." *Remote Sensing of Environment* 227: 28–43. https://doi.org/10.1016/j.rse.2019.03.024.

Wang, Chenghao, Zhi-Hua Wang, and Jiachuan Yang. 2018. "Cooling Effect of Urban Trees on the Built Environment of Contiguous United States." *Earth's Future* 6 (8): 1066–81. https://doi.org/10.1029/2018EF000891.

———. 2019. "Urban Water Capacity: Irrigation for Heat Mitigation." *Computers, Environment and Urban Systems* 78: 101397. https://doi.org/10.1016/j.compenvurbsys.2019.101397.

Wang, Chenghao, Zhi-Hua Wang, Jiachuan Yang, and Qi Li. 2018. “A Backward-Lagrangian-Stochastic Footprint Model for the Urban Environment.” *Boundary-Layer Meteorology* 168: 59–80. https://doi.org/10.1007/s10546-018-0338-6.

Wang, Jingfeng, Rafael L. Bras, Manuel Lerdau, and Guido D. Salvucci. 2007. “A Maximum Hypothesis of Transpiration.” *Journal of Geophysical Research* 112: G03010. https://doi.org/10.1029/2006JG000255.

Wang, M., M. Wagner, G. Miguez-Macho, Y. Kamarianakis, A. Mahalov, M. Moustaoui, J. Miller, et al. 2017. “On the Long-Term Hydroclimatic Sustainability of Perennial Bioenergy Crop Expansion over the United States.” *Journal of Climate* 30 (7): 2535–57. https://doi.org/10.1175/JCLI-D-16-0610.1.

Wang, Zhi-Hua. 2014a. “A New Perspective of Urban–Rural Differences: The Impact of Soil Water Advection.” *Urban Climate* 10: 19–34. https://doi.org/10.1016/j.uclim.2014.08.004.

———. 2014b. “Monte Carlo Simulations of Radiative Heat Exchange in a Street Canyon with Trees.” *Solar Energy* 110: 704–13. https://doi.org/10.1016/j.solener.2014.10.012.

Wang, Zhi-Hua, Elie Bou-Zeid, and James A. Smith. 2013. “A Coupled Energy Transport and Hydrological Model for Urban Canopies Evaluated Using a Wireless Sensor Network.” *Quarterly Journal of the Royal Meteorological Society* 139 (675): 1643–57. https://doi.org/10.1002/qj.2032.

Wang, Zhi-Hua, Chao Fan, Soe W. Myint, and Chenghao Wang. 2016. “Size Matters: What Are the Characteristic Source Areas for Urban Planning Strategies?” *PLoS ONE* 11 (11): e0165726. https://doi.org/10.1371/journal.pone.0165726.

Wang, Zhi-Hua, and Qi Li. 2017. “Thermodynamic Characterisation of Urban Nocturnal Cooling.” *Heliyon* 3 (4): e00290. https://doi.org/10.1016/j.heliyon.2017.e00290.

Wang, Zhi-Hua, Xiaoxi Zhao, Jiachuan Yang, and Jiyun Song. 2016. “Cooling and Energy Saving Potentials of Shade Trees and Urban Lawns in a Desert City.” *Applied Energy* 161: 437–44. https://doi.org/10.1016/j.apenergy.2015.10.047.

Way, Danielle A., and Ram Oren. 2010. “Differential Responses to Changes in Growth Temperature between Trees from Different Functional Groups and Biomes: A Review and Synthesis of Data.” *Tree Physiology* 30 (6): 669–88. https://doi.org/10.1093/treephys/tpq015.

Wilson, John D., and Brian L. Sawford. 1996. “Review of Lagrangian Stochastic Models for Trajectories in the Turbulent Atmosphere.” *Boundary-Layer Meteorology* 78 (1–2): 191–210. https://doi.org/10.1007/BF00122492.

Wood, Nigel. 2000. “Wind Flow over Complex Terrain: A Historical Perspective and the Prospect for Large-Eddy Modelling.” *Boundary-Layer Meteorology* 96 (1–2): 11–32. https://doi.org/10.1023/A:1002017732694.

Xue, Fei, and Xiaofeng Li. 2017. “The Impact of Roadside Trees on Traffic Released PM_{10} in Urban Street Canyon: Aerodynamic and Deposition Effects.” *Sustainable Cities and Society* 30: 195–204. https://doi.org/10.1016/j.scs.2017.02.001.

Yang, Jiachuan, Leiqiu Hu, and Chenghao Wang. 2019. “Population Dynamics Modify Urban Residents’ Exposure to Extreme Temperatures across the United States.” *Science Advances*, in press.

Yang, Jiachuan, and Zhi-Hua Wang. 2015. “Optimizing Urban Irrigation Schemes for the Trade-off between Energy and Water Consumption.” *Energy and Buildings* 107: 335–44. https://doi.org/10.1016/j.enbuild.2015.08.045.

Yang, Jiachuan, Zhi-Hua Wang, Fei Chen, Shiguang Miao, Mukul Tewari, James A. Voogt, and Soe Myint. 2015. “Enhancing Hydrologic Modelling in the Coupled Weather Research and Forecasting–Urban Modelling System.” *Boundary-Layer Meteorology* 155 (1): 87–109. https://doi.org/10.1007/s10546-014-9991-6.

Yang, Jiachuan, Zhi-Hua Wang, Matei Georgescu, Fei Chen, and Mukul Tewari. 2016. “Assessing the Impact of Enhanced Hydrological Processes on Urban Hydrometeorology with Application to Two Cities in Contrasting Climates.” *Journal of Hydrometeorology* 17 (4): 1031–47. https://doi.org/10.1175/JHM-D-15-0112.1.

Zhao, Junbin, Henrik Hartmann, Susan Trumbore, Waldemar Ziegler, and Yiping Zhang. 2013. “High Temperature Causes Negative Whole-Plant Carbon Balance under Mild Drought.” *New Phytologist* 200 (2): 330–39. https://doi.org/10.1111/nph.12400.

Zhao, Shuqing, Shuguang Liu, and Decheng Zhou. 2016. “Prevalent Vegetation Growth Enhancement in Urban Environment.” *Proceedings of the National Academy of Sciences of the United States of America* 113 (22): 6313–18. https://doi.org/10.1073/pnas.1602312113.

Zhou, L., R. E. Dickinson, Y. Tian, X. Zeng, Y. Dai, Z.-L. Yang, C. B. Schaaf, et al. 2003. “Comparison of Seasonal and Spatial Variations of Albedos from Moderate-Resolution Imaging Spectroradiometer (MODIS) and Common Land Model.” *Journal of Geophysical Research: Atmospheres* 108 (D15): 4488. https://doi.org/10.1029/2002JD003326.

Zhou, Weiqi, Jia Wang, and Mary L. Cadenasso. 2017. “Effects of the Spatial Configuration of Trees on Urban Heat Mitigation: A Comparative Study.” *Remote Sensing of Environment* 195: 1–12. https://doi.org/10.1016/j.rse.2017.03.043.

APPENDIX A

DATA SOURCES AND INFORMATION OF THE URBAN TREE STATISTICS

The data sources and information of the urban tree statistics shown in Table 4.2 are summarized below with the following format: name of the metropolitan area, *data source (report or inventory)*, data source publication date, study area, inventory date, number of trees in the report or inventory, note, and the link to the report or inventory.

1. Atlanta. Data source: *Downtown Tree Management Plan for City of Atlanta, Georgia*. Data source publication date: November 2012. Study area: Downtown Atlanta and the expanded area. Inventory date: July–August 2011. Number of trees in the report or inventory: 8465. Note: 85.75% for street trees, and 14.25% for park trees. Links: https://www.atlantaga.gov/Home/ShowDocument?id=10872, and https://www.atlantaga.gov/government/departments/city-planning/office-of-buildings/arborist-division/downtown-tree-inventory.

2. Boston-Providence. Data source: *Providence's Urban Forest: Structure, Effects and Values*. Data source publication date: Feb 2014. Study area: City of Providence. Inventory date: 2013. Number of trees in the report or inventory: 415000. Note: Only the top 11 most common tree species were documented. Link: https://www.itreetools.org/resources/reports/iTreeEcoProv2014.pdf or https://www.itreetools.org/resources/reports.php.

3. Chicago. Data source: *Urban Trees and Forests of the Chicago Region*. Data source publication date: August 2013. Study area: Chicago region. Inventory date: 2010. Number of trees in the report or inventory: 157142000. Note: N/A. Link: https://www.nrs.fs.fed.us/pubs/44566.

4. Dallas-Fort Worth-Arlington. Data source: *Downtown Dallas Tree Inventory & Ecosystem Services Benefits Report*. Data source publication date: May 2015. Study area:

Downtown Dallas. Inventory date: August 2014–March 2015. Number of trees in the report or inventory: 6218. Note: N/A. Link: http://www.texastrees.org/projects/downdown-dallas/.

5. Detroit Metropolitan. Data source: *Urban & Community Forestry Program, Michigan Department of Natural Resources*. Data source publication date: Note mentioned. Study area: Detroit. Inventory date: ~2015–2016. Number of trees in the report or inventory: 130625. Note: only the top 5 most common tree species were documented. Link: https://www.michigan.gov/documents/dnr/UCF_Presentation_-_FMAC_2016_2_510160_7.pdf.

6. Los Angeles-Riverside. Data source: *Assessing Urban Forest Effects and Values, Los Angeles' Urban Forest*. Data source publication date: March 2011. Study area: City of Los Angeles. Inventory date: 2007–2008. Number of trees in the report or inventory: ~6.0 million. Note: most deciduous trees can be evergreen or semi-evergreen in Los Angeles. Link: https://www.nrs.fs.fed.us/pubs/37671.

7. Miami. Data source: *Street Tree Management Plan*. Data source publication date: July 2015. Study area: City of North Miami. Inventory date: 2015. Number of trees in the report or inventory: 15968. Note: only the top 10 most common tree species were documented. Link: http://northmiamifl.gov/docs/N_Miami_Street_Tree_Management_Plan_07202015.pdf.

8. Minneapolis-St. Paul. Data source: *City of Minneapolis, Minnesota Municipal Tree Resource Analysis*. Data source publication date: June 2005. Study area: 3 districts in Minneapolis. Inventory date: 2004. Number of trees in the report or inventory: 198633. Note: N/A. Link: https://www.fs.usda.gov/treesearch/pubs/45984.

9. New York Metropolitan. Data source: *New York City, New York Municipal Tree Resource Analysis*. Data source publication date: March 2007. Study area: New York City. Inventory date: 2005–2006. Number of trees in the report or inventory: 592130. Note: N/A. Link: https://www.fs.usda.gov/treesearch/pubs/45969.

10. Phoenix Metropolitan. Data source: *Phoenix, Arizona – Community Forest Assessment*. Data source publication date: August 2014. Study area: City of Phoenix. Inventory date: 2013. Number of trees in the report or inventory: 3166000. Note: most deciduous trees can be evergreen or semi-evergreen in Phoenix. Link: https://www.itreetools.org/resources/reports/DesertCanopy/Phoenix_Community_Forest_Assessment_1.2.15-Final.pdf.

11. Washington-Baltimore. Data source: District of Columbia Assessment of Urban Forest Resources and Strategy. Data source publication date: June 2010. Study area: Washington, D.C. Inventory date: 2006. Number of trees in the report or inventory: 144000. Note: N/A. Link: https://ddot.dc.gov/page/dc-assessment-urban-forest-resources-and-strategy.